NONLINEAR TIME-FREQUENCY CONTROL THEORY WITH APPLICATIONS

A Dissertation

by

MENG-KUN LIU

Submitted to the Office of Graduate Studies of
Texas A&M University
in partial fulfillment of the requirements for the degree of

DOCTOR OF PHILOSOPHY

Approved by:

Chair of Committee,	Chii-Der S. Suh
Committee Members,	Alan Palazzolo
	Jyhwen Wang
	Jim Ji
Head of Department,	Jerald A. Caton

December 2012

Major Subject: Mechanical Engineering

ABSTRACT

Nonlinear control is an important subject drawing much attention. When a nonlinear system undergoes route-to-chaos, its response is naturally bounded in the time-domain while in the meantime becoming unstably broadband in the frequency-domain. Control scheme facilitated either in the time- or frequency-domain alone is insufficient in controlling route-to-chaos, where the corresponding response deteriorates in the time and frequency domains simultaneously. It is necessary to facilitate nonlinear control in both the time and frequency domains without obscuring or misinterpreting the true dynamics. The objective of the dissertation is to formulate a novel nonlinear control theory that addresses the fundamental characteristics inherent of all nonlinear systems undergoing route-to-chaos, one that requires no linearization or closed-form solution so that the genuine underlying features of the system being considered are preserved. The theory developed herein is able to identify the dynamic state of the system in real-time and restrain time-varying spectrum from becoming broadband. Applications of the theory are demonstrated using several engineering examples including the control of a non-stationary Duffing oscillator, a 1-DOF time-delayed milling model, a 2-DOF micro-milling system, unsynchronized chaotic circuits, and a friction-excited vibrating disk.

Not subject to all the mathematical constraint conditions and assumptions upon which common nonlinear control theories are based and derived, the novel theory has its philosophical basis established in the simultaneous time-frequency control, on-line system identification, and feedforward adaptive control. It adopts multi-rate control, hence enabling control over nonstationary, nonlinear response with increasing bandwidth – a physical condition oftentimes fails the contemporary control theories. The applicability of the theory to complex multi-input-multi-output (MIMO) systems without resorting to mathematical manipulation and extensive computation is demonstrated through the multi-variable control of a micro-milling system. The research is of a broad impact on the control of a wide range of nonlinear and chaotic systems. The implications of the nonlinear time-frequency control theory in cutting, micro-machining, communication security, and the mitigation of friction-induced vibrations are both significant and immediate.

ACKNOWLEDGEMENTS

I would like to express my sincere gratitude to my committee chair, Dr. C. Steve Suh for his instruction. He taught me the right way to do research; that is, not being a follower but always challenging the conventional wisdoms and digging into the core of the problem. He is also my life mentor, guiding me when I encounter difficulties, supporting me when I am depressed, encouraging me to grow academically and professionally, and most importantly, advising me to always plan for the future. I would not have been able to finish this dissertation without his support.

I would also like to thank my committee members, Dr. Alan Palazzolo, Dr. Jyhwen Wang, and Dr. Jim Ji, for their precious opinions and suggestions throughout the course of this research. Many thanks also go to my colleagues, especially Eric Halfmann, Xuele Qi, Brandon C. Gegg, and Chi-Wei Kuo, for their companion and assistance. I also want to extend my gratitude to Texas A&M University for providing an excellent study and research environment.

Finally, I would like to dedicate this dissertation to my beloved father, Mr. Tong-Chin Liu, and mother, Mrs. Mei-Jung Chen, for their unconditional love and support. I cannot complete this doctoral program without them.

TABLE OF CONTENTS

Page

Page

LIST OF FIGURES

FIGURE Page

FIGURE Page

FIGURE Page

FIGURE Page

LIST OF TABLES

TABLE Page

1. INTRODUCTION AND LITERATURE REVIEW*

1.1 Overview and Literature Review

Research on chaos control has drawn much attention over several decades. Open-loop control and closed-loop control are the two major categories. Open-loop control, which alters the behavior of a nonlinear system by applying a properly chosen input function or external excitation, is simple and requires no sensors. However, open-loop control is in general limited by the fact that its action is not goal oriented [1]. Closed-loop control, on the other hand, feedbacks a perturbation selected based upon the state of the system to control a prescribed dynamics. Of the many closed-loop chaos control theories formulated over the years, the OGY method, delayed feedback control, Lyapunov-based control and adaptive control are considered prominent. The OGY method [2] uses small discontinuous parameter perturbation to stabilize a chaotic orbit and forces the trajectory to follow a target UPO (unstable periodic orbit) in a chaotic attractor. It uses the eigenvalues of the system's Jacobian at fixed point(s) to establish stability. But for chaotic systems of higher dimensions, there are complex eigenvalues or multiple unstable eigenvalues, making it difficult to control such systems by the OGY method [3]. Several revisions have been made to control chaos in higher-order dynamic-

---

*Part of this chapter is reprinted with permission from "Simultaneous Time-Frequency Control of Bifurcation and Chaos" by Liu, M. K. and Suh, C. S., 2012, Communications in Nonlinear Science and Numerical Simulations, 17(6), pp. 2539-2550, Copyright 2012 by Elsevier al systems [3-6]. Another disadvantage is that the available adjustable range of the controlling parameter is limited by the distance between the system state variable and UPO. Because the initiation of OGY control requires that the state variable approaches the proximity of the target UPO, the waiting time can be shortened by applying the reconstruction of phase plane [7]. Nonetheless, it is very difficult to obtain an exact, analytic formula for an UPO. It is even more so to physically implement UPOs due to the instability nature of such orbits [8]. Since the corrections of the parameter are discrete, rare and small, presence of noise can lead to occasional bursts of the system into regions far from the desired periodic orbit [9]. These difficulties limit the OGY method to only a few applications such as the control of robot arms [10], forced pendulum [11, 12] and power systems [13].

Another widely accepted chaos control theory is the delayed feedback control (DFC) [9]. The stabilization of UPO of a chaotic system can be achieved either by combined feedback with the use of a specially designed external oscillator, or by delayed self-controlling feedback. The feedback is a small continuous perturbation that is less vulnerable to noises. Unlike the OGY method, it doesn’t need *a priori* analytical knowledge of the system dynamic, except for the period of the target UPO, and it can be applied to high-dimensional system. Recent efforts include the stability analysis [14] and the stabilization of UPO with arbitrarily large period [15]. A comprehensive review of the delayed feedback control method is found in [16]. The drawback of the delayed feedback control is that it is hard to conduct linear stability analysis of the delayed feedback system [16] and that its performance is very sensitive to the choice of the delay

[17]. If the control goal is to stabilize a forced T-periodic solution, the delay will mandatorily be set to T. Alternatively, a heuristic method is used to estimate the delay time, but it is still difficult to find the smallest period.

Lyapunov's direct method allows the stability of a system to be determined without explicitly integrating the dynamic equation. It relies on the physical property that the system, whose total energy is continuously being dissipated, must eventually end up at an equilibrium point [18]. Suppose a continuously differentiable positive definite (Lyapunov) function V(x) can be derived from the system. The system is stable if the derivative of V(x) is negative semi-definite, and asymptotically stable if the derivative of V(x) is negative definite. This concept can be integrated into controller design. As long as the derivative of Lyapunov function of the system is confined to negative semi-definite or definite along the closed-loop system trajectory, the system is guaranteed stable or asymptotically stable. Lyapunov-based controller has been applied to the synchronization of chaos [19-21], Duffing oscillators [22, 23], chaotic pendulum [24] and robotics [18]. Its drawback is that the Lyapunov function cannot necessarily be asserted from some particular models, and the chosen parameters may be too conservative, thereby compromising the transient response of the system [18].

An identification algorithm usually is coupled with the control algorithm to facilitate adaptive control over the dynamical system that has unknown parameters in its governing equation. In adaptive control, parameter estimation and control are performed simultaneously. When the system parameters are estimated and control action is calculated based on the estimated parameters, the adaptive control scheme is called indirect adaptive control. In direct adaptive control, on the other hand, controller parameters are directly updated using an adaptive law. Adaptive control theory modifies the control law to cope with the time-varying parameters of the system. Even though adaptive control describes a nonlinear system by a linear model, the feedback tuning of its parameters renders the overall system response nonlinear. Hence, adaptive control is widely adopted for the control of chaotic systems, such as Hénon map [25], nonlinear pendulum [26], chaos synchronization [27], and hyper-chaos system [28]. A priori knowledge of the system is required for model-based adaptive control, which focuses exclusively on time-domain performance.

Although all demonstrated capability in controlling chaos, however, the applicability of the chaos control theories reviewed above is limited to autonomous, stationary systems. They are all developed assuming chaotic system to be autonomous even though nonlinear dynamics concerns predominantly with non-autonomous systems. These controllers are good at handling “static chaos,” meaning the state of chaos doesn’t change. “Static chaos” doesn’t transition from bifurcation to chaos as is explicit in a bifurcation diagram. The spectral bandwidth of its response doesn’t change either. For non-autonomous, non-stationary systems whose chaotic responses are “dynamic,” these chaos control theories would fail. Two examples on chaos control are studied in the followings.

1.1.1 OGY Control of Hénon Maps

Consider the two-dimensional iterative (Hénon) map function below with $\alpha > 0$, $|\beta| < 1$, and $r_n^2 = x_n^2 + y_n^2$

$$\begin{cases} x_{n+1} = 1 + y_n - \alpha x_n^2 \\ y_{n+1} = \beta x_n \end{cases} \tag{1.1}$$

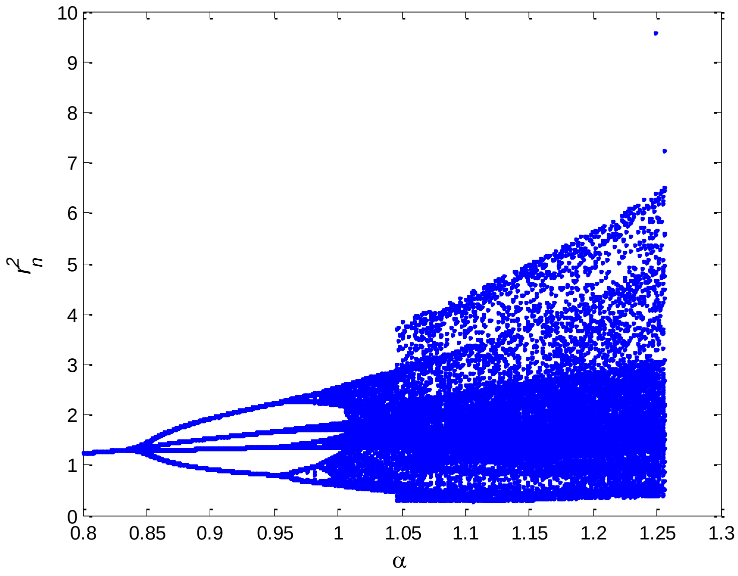

Fig. 1.1 Bifurcation diagram of Hénon map

When parameter α is increasing, the system undergoes bifurcation, as depicted in Fig. 1.1. Because α varies in time, the nonlinear dynamics shown in Fig. 1.1 is one of non-autonomous and time-variant. If β = 0.4 and α is set at 1.2, the response is a chaotic attractor. But this time it is a case of "static chaos." The range of its time response and frequency spectrum remains unchanging. Fig. 1.2 shows the corresponding time response and instantaneous frequency (IF) [29] of the Hénon map when the OGY method [30] is applied. With the controller being turned on at the 300th-time step (see Fig. 1.2(a)), the chaotic response is stabilized to a fixed point. The response is examined by IF in Fig. 1.2(b) using an integration time step Δt = 0.1s. The IF plot shows a transient between t = 30sec and t = 62sec, followed by a null region devoid of any time-frequency activity. Both the time response and IF signify that the OGY method is able to stabilize the chaotic attractor generated by a stationary Hénon Map.

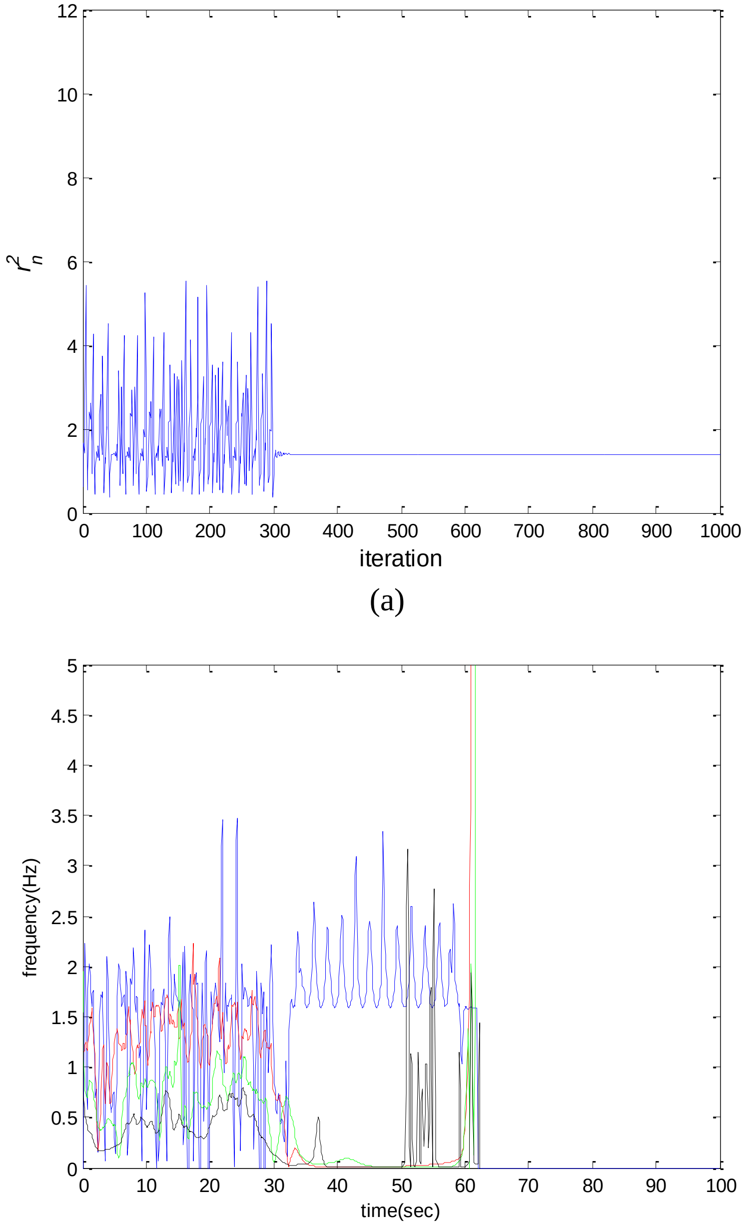

(a)

(b)

Fig. 1.2 (a) time response (b) instantaneous frequency of the Hénon Map controlled by OGY method

Fig. 1.3 shows the bifurcation diagram of a non-stationary Hénon Map controlled by the same OGY method, in which the controlling parameter α is increasing in time. The OGY method fails for such a non-autonomous, nonstationary system.

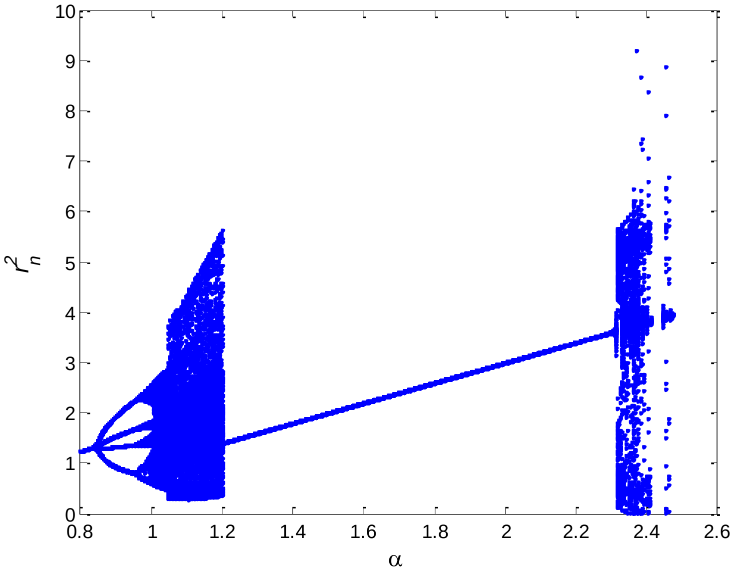

Fig. 1.3 Bifurcation diagram of a non-autonomous Hénon map controlled by OGY method

In Fig. 1.3, the controller is activated when α = 1.2. For a stationary system, r_n^2 would be fixed when the controller is turned on, which means that it has only one frequency when the system is under control. But in Fig. 1.3 it shows that the trajectory in the bifurcation diagram is no longer a straight line. It means that the frequency is changing and that chaos abruptly emerges when α is increased to around 2.3. The result is not surprising because the concept of the OGY method is based on the linearization of the Poincaré map. Hence its stability region is inevitably limited to the vicinity of the equilibrium point.

1.1.2 Lyapunov-based Control of Duffing Oscillators

Consider 2 Duffing oscillators

$$\ddot{x} + p\dot{x} + p_1 x + x^3 = q cos(\omega t) \tag{1.2}$$

$$\ddot{x} + p\dot{x} + p_1 x + x^3 = (q + 0.01t) cos(\omega t) \tag{1.3}$$

with p = 0.4, p_1 = -1.1, q = 2.1 and ω = 1.8. Note that the excitation amplitude is a time function in Eq. (1.3). The Lyapunov-based controller designed in [23] is applied to both cases and a reference (target) response is set to be *sin(t)*. Fig. 1.4 compares the responses of the stationary and nonstationary Duffing oscillators controlled by the Lyapunov-based controller. The amplitudes of the external excitation in Fig. 1.4(a-c) are held constant. Fig. 1.4(a) shows that when the controller is turned on at t = 500sec, the controller stabilizes the system and mitigates the chaotic response to a periodic motion. This result agrees with its time-domain error between the system response and the reference trajectory as shown in Fig. 1.4(b). The instantaneous frequency in Fig. 1.4(c) shows that the controller also has a good performance in the IF domain. There's only one frequency left after t = 500sec. A second frequency is also seen emerging at t = 700sec. On the contrary, the Lyapunov-based controller loses control when the amplitude of the external excitation is increasing in time in Fig. 1.4(d-f). In Fig. 1.4(d) the response is no longer a periodic motion and in Fig. 1.4(e) the time-domain error increases in time. Further, from the IF plot in Fig. 1.4(f), the frequency remains oscillating in time after the controller is engaged, indicative of the presence of nonlinearity [31].

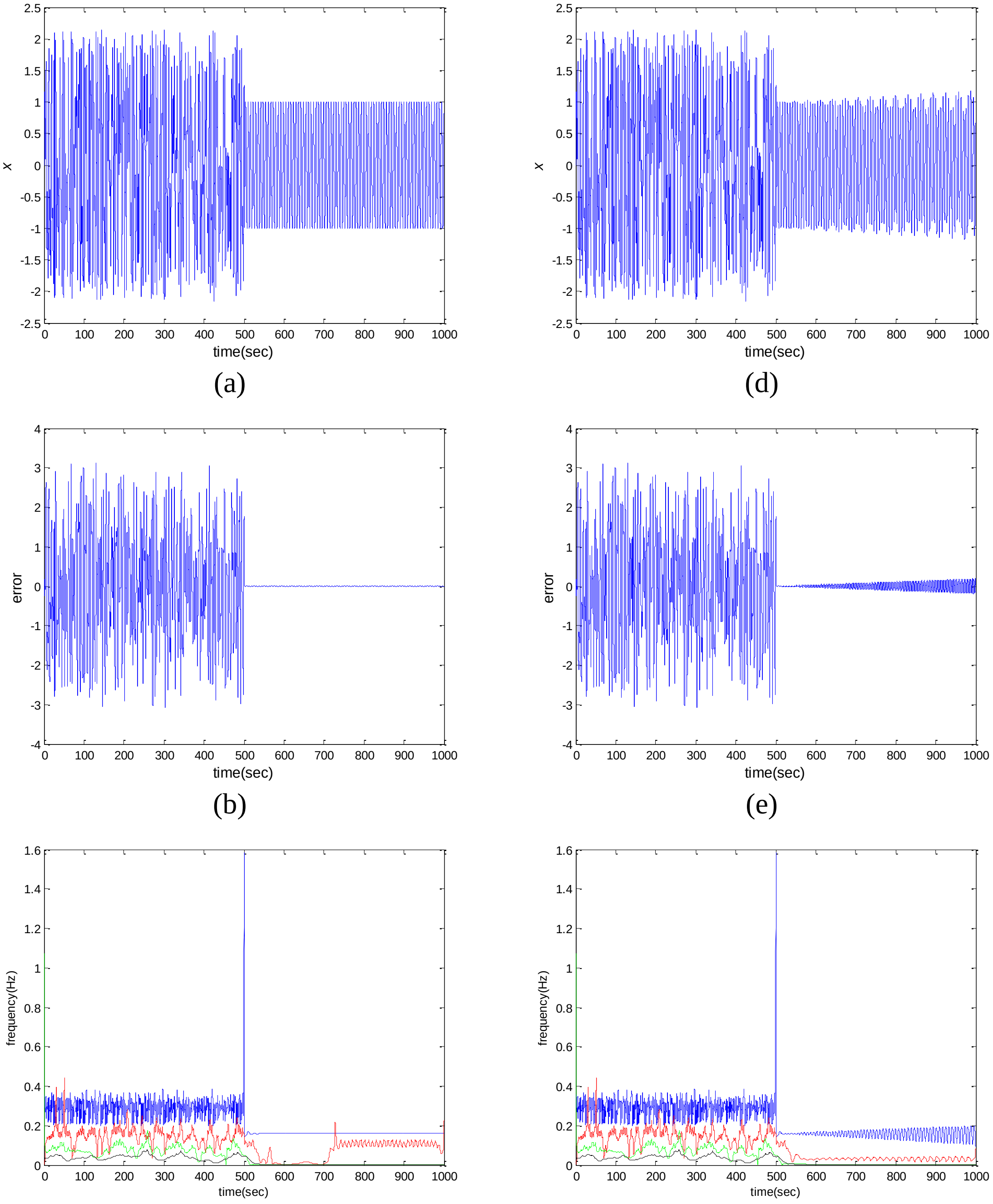

(a) (d)

(b) (e)

(c) (f)

Fig. 1.4 (a) Time response, (b) time-domain error, and (c) IF of a stationary Duffing oscillator, and (d) time response, (e) time-domain error, and (f) IF of a nonstationary Duffing oscillator, all controlled by Lyapunov-based controller

In summary, the Lyapunov-based controller was able to deny the progression of chaos in the stationary Duffing oscillator, but for the nonstationary oscillator, it lost control in both the time and frequency domains. The review performed above can be summarized using the following observations:

1. All reviewed chaos control theories failed to mitigate “dynamic chaos.” The OGY method is based on the linearization of the Poincaré map. It discards nonlinear terms and uses Jacobian matrix to determine the stability of the equilibrium point around its vicinity. The method worked for the autonomous, stationary system but failed for the non-autonomous, nonstatioary system for the reason that in the latter its trajectories in the Poincaré map were subject to change in time. They ran away from the equilibrium point and the stability established by the Jacobian matrix at equilibrium point was no longer valid. The Lyapunov-based controller also failed for the non-autonomous, nonstationary system because the variation of the system parameter directly affected the derivation of the Lyapunov function.
2. A priori knowledge of the system must be available for the control theories to be effective. For the OGY method, the period of unstable periodic orbits (UPOs) must be known and the system state on the Poincaré map must be observed. But it is very difficult to obtain exact analytic formulation for an UPO [8]. Lyapunov-based controller uses energy-like concept to define Lyapunov function, and by examining its derivative, to determine the stability of the equilibrium point. But there is no systematic way for finding the Lyapunov function and in some cases it’s basically a matter of trial-and-error. Even if a Lyapunov function could be found, it is only for

an autonomous, nonstationary system. For delayed feedback control, the delayed time is set to the period of the desired orbit, and a heuristic method is then used to estimate the delay time. But it is still difficult to find the smallest period.

3. None of the theories control both time and frequency responses simultaneously. Except for the OGY method, all are formulated in the time-domain. However, as seen previously, the instantaneous frequency of a nonlinear, nonstationary system undergoing route-to-chaos is characteristically time-modulated and broad spectral bandwidth with emerging new frequency components. This was further asserted in the nonstationary Duffing oscillator where both time and frequency responses deteriorated at the same time. A controller designed to control time-domain error would not be able to negate the increasing of the spectrum. On the other hand, a controller designed in the frequency-domain would confine the expansion of the bandwidth while losing control over time-domain error. Neither frequency-domain nor time-domain based controllers are effective in mitigating bifurcation and chaotic response.

1.1.3 Property of Chaos Control

The review on the chaos control of non-autonomous, nonstationary systems provides several hints essential to the development of a viable control solution. The solution can be formulated by recognizing the various attributes inherent of a chaotic system, including the simultaneous deterioration of dynamics in both the time and frequency domains when bifurcates, nonstationarity, and sensitivity to initial conditions.

For a linear time-invariant system, only the amplitude and the phase angle of the excitation input vary. The response frequency remains the same with respect to the input frequency, and the system can be stabilized by applying a proper feedback gain. Both time- and frequency-domain responses are bounded. However, this is not the case for the chaotic response generated by a nonlinear system, which contains an infinite number of unstable periodic orbits of all periods called strange attractors. Chaotic response doesn't remain following one periodic orbit but switching rapidly between many unstable periodic orbits. If the chaotic response is projected into a Poincaré section, a lower dimensional subspace transversal to the trajectory of the response, it can be shown that the intersection points congregate densely and are confined within a finite area. It indicates that the chaotic response is bounded in the time-domain while simultaneously becoming unstably broadband in the frequency-domain due to the rapid switching between infinite numbers of UPOs. Hence, for a chaos control algorithm to be effective, control has to be performed in the time and frequency domains simultaneously.

The second property universal of chaotic systems is nonstationarity. Route-to-chaos is a temporal, transient process. The location and the stability of the equilibrium point therefore also vary in time. For high dimensional system, a priori knowledge of the system is often hard to come by. It is thus necessary for a viable chaos control scheme to conduct on-line identification and control at the same time in order to cope with the time varying parameters of the system. The third property is the sensitivity of a chaotic system to initial conditions. A minor deviation between two closed initial trajectories might diverge exponentially with the increase of time, thus implying that a small perturbation could render the system unstable. Reversely, a nonlinear system can also be stabilized by a small perturbation, as implied by open-loop chaos control theories of early days that it is possible to stabilize a chaotic system by giving small perturbations to its input or system parameters.

1.2 Research Objectives

The objective of the dissertation is to *formulate a novel nonlinear control theory that addresses and retains the fundamental characteristic inherent of all nonlinear systems undergoing route-to-chaos*; that is, one that requires no linearization or closed form solution so that the genuine underlying features of the system being considered are preserved. The theory is also required to be able to (1) restrain time-varying frequency spectrum from becoming broadband and (2) identify the dynamic state of the system in real-time. In other words, the theory is to enable the facilitation of control in the time and frequency domain simultaneously without distorting or misinterpreting the true dynamics.

To address the stated objective, the following research tasks are defined, including investigating the temporal and spectral behaviors of the route-to-chaos process and conducting an extensive review on the contemporary chaos control theories so as to identify the discrepancy that is fundamental to their being invalid and ineffective in controlling nonlinear responses.

- Investigate route-to-chaos in the time and frequency domain concurrently.
- Identify the essential elements of nonlinear control through studying the innate properties of bifurcation and chaos.

- Develop a novel nonlinear control theory that mandates no linearization and closed form solution.
- Adopt time domain discrete wavelet transform and adaptive filters to facilitate simultaneous time-frequency control.
- Optimize the selection of mother wavelet and decomposition level.
- Design target signal using Fourier expansion.
- Test to validate the nonlinear control theory using nonstationary Duffing oscillators that display route-to-chaos dynamic deterioration.

Apply the nonlinear control theory to explore viable control solutions for complex engineering systems, including milling, micro-machining, synchronization of chaos, and friction-induced vibration.

2. TEMPORAL AND SPECTRAL RESPONSES OF A SOFTENING DUFFING OSCILLATOR UNDERGOING ROUTE-TO-CHAOS*

2.1 Introduction

One of the essential objectives in studying a nonlinear system is to obtain the condition that guarantees the existence of periodic solutions so that their stabilities can be subsequently determined [32]. Steady-state solution is obtained for small but finite amplitude oscillations around the equilibrium point to estimate the threshold value of the excitation amplitude, stability region, and number of limit cycles. Linearization is performed under the assumption that if the operation range is in the immediate proximity of the equilibrium point of the nonlinear system, the response of the linearized model would approximate the nonlinear one with accuracy. However, there are cases that, although giving correct time profile of the nonlinear response, the inherent components resolved using perturbation methods neither collectively nor individually provide any physically meaningful representation of the nonlinear system [33]. Applying linearization to investigate nonlinear system without exercising proper discretions would obscure the underlying nonlinear characteristics and risk misinterpreting the stability bound.

---

*Part of this chapter is reprinted with permission from “Temporal and Spectral Responses of A Softening Duffing Oscillator Undergoing Route-To-Chaos” by Liu, M. K. and Suh, C. S., 2012, Communications in Nonlinear Science and Numerical Simulations, 17(12), pp. 5217-5228, Copyright 2012 by Elsevier

Fourier-based analyses have been widely accepted as a tool for exploring nonlinear system. Because stationary sinusoids are employed in representing time-varying signals of inherent nonlinearity, the use of Fourier domain methodologies would also risk misrepresenting the underlying physics of the nonlinear system being investigated [34]. As most methods employed to process nonstationary signals are Fourier-based, they also suffer from the shortcomings associated with Fourier transform [35]. The fact that nonlinear responses including route-to-chaos are intrinsically transient, nonstationary with coupled amplitude-frequency modulation implies that, if a nonlinear response is to be fully characterized, the inherent amplitude modulation (AM) and frequency modulation (FM) need to be temporally decoupled [35]. The concept of Instantaneous Frequency (IF) is adopted in this study to resolve the dependency of frequency on time. Growing attention is focused on the Hilbert-Huang Transform (HHT), which has been used to investigate the response of quadratic and cubic nonlinearities [36], Duffing oscillators [37], dynamic systems with slowly-varying amplitudes and phases [38], and fault induced nonlinear rotary [39]. Because HHT does not use predetermined basis functions and their orthogonality for component extraction, it provides instantaneous amplitude and frequency of the extracted components for the accurate estimation of system characteristics and nonlinearities [40]. It is shown that HHT is better appropriate than sinusoidal harmonics for characterizing nonstationary and transient responses. The interpretation of nonlinearity using IF is found to be both intuitively rigorous and physically valid.

Various Duffing oscillators have been explored to help elucidate a wide range of physical applications in the real-world. In Ref. [41] the response of a damped Duffing oscillator with harmonic excitation is analyzed by second-order perturbation solutions along with Floquet analysis to predict symmetry-breaking and period-doubling bifurcation. Duffing oscillators under nonstationary excitations are also considered by many, where linear and cyclic variations of frequencies and amplitudes are applied and nonstationary bifurcation is studied. It is shown that nonstationary process is distinct from stationary process with different characteristics [42, 43]. Nonetheless, these perturbation method based studies on nonlinear systems generate nonphysical results that are bound to be misinterpreted. The presentation that follows reviews the nonlinearity and nonstationary bifurcation of a softening Duffing oscillator from the time-frequency perspective established using IF. It is noted that although IF is considered a viable tool for exploring nonlinear dynamic response, little effort has been made to study the generation and evolution of bifurcation to ultimate chaotic response, a process that is inherently nonstationary and transient. A Duffing oscillator and its linearized counterpart are studied first by fast Fourier transform (FFT), short time Fourier transform (STFT), Gabor transform, and instantaneous frequency (IF). The second part of the paper presents an in-depth investigation into the rout-to-chaos generated by the Duffing oscillator under nonstationary excitation using conventional nonlinear dynamic analysis tools and IF.

2.2 Instantaneous Frequency and Intrinsic Mode Function

The concept of instantaneous frequency was introduced to resolve the time evolution of the spectral response of a nonstationary signal [44] – a task of which Fourier-based analyses fall short. IF is defined as the time derivative of the phase of a complex signal. Such a definition was shown to work well with signals of monocomponent. In the followings the definition of instantaneous frequency is briefly reviewed. A time-varying signal $x(t)$ having both amplitude modulated (AM) and frequency modulated (FM) components can be represented as $x(t) = c(t)\cos(\theta(t))$. Its corresponding analytic signal can be defined as

$$s(t) = x(t) + iy(t) = x(t) + iH[x(t)] = c(t)\exp(i\theta(t)) \tag{2.1}$$

where $s(t)$ is the analytic signal, $c(t)$ is the instantaneous amplitude, $\theta(t)$ is the instantaneous phase, and $y(t)$ is the imaginary part of $s(t)$. Defining $H[x(t)]$ as the Hilbert Transform of the time varying signal *x(t)*

$$y(t) = H[x(t)] = \frac{p}{\pi}\int_{-\infty}^{\infty} \frac{x(\tau)}{t-\tau} d\tau = x(t) \cdot (p/\pi t) \tag{2.2}$$

with *p* being the Cauchy principle value. In theory $x(t)$ and $y(t)$ are out of phase by $\pi/2$. The instantaneous amplitude and phase are defined as $c(t) = \sqrt{x^2(t) + y^2(t)}$ and $\theta(t) = \tan^{-1}(y(t)/x(t))$, respectively. By Ville's definition [44] the derivative of the instantaneous phase is the instantaneous frequency, thus, $f(t) = (1/2\pi)(d\theta(t)/dt)$. Such a definition agrees with our intuition for instantaneous frequency and captures the concept of instantaneity in nature. However, the definition fails when applied to multicomponent signals for the reason that it adversely averages all the individual IFs associated with each individual monocomponent and interprets them as single instantaneous frequency. In addition to falling short on providing a unified interpretation for signals of multicomponent, the definition also allows infinite and negative frequencies to be induced. The Empirical Mode Decomposition (EMD) scheme proposed by Huang et al. [33] effectively decomposes a time series into its several inherent physical modes of motion called the Intrinsic Mode Functions (IMF). Each IMF is an orthogonal set of intrinsic monocomponent from the response and retains the inherent physical features. By definition, every mode has the same numbers of extrema and zero crossings and the inherent oscillation is symmetric with respect to a local mean defined by the average of the maximum envelope and minimum envelop without resorting to any time scale. All the inherent IMFs, $C_1(t)$, $C_2(t)$, $C_3(t)\ldots$, and C_m of the dynamic response *x(t)* can be extracted using a shifting algorithm that resolves a residual term *R(t)* that carries no frequency component. It can be shown that the summation of all the IMFs and the residual term restores back to the response, $x(t)=\sum_{j=1}^{m}C_j(t)+R(t)$. From the decomposition process, it is understood that the first mode (C_1) has the smallest time scale, indicating that it includes the highest frequency components. As the decomposition continues, the frequency components included in IMF become lower. The decomposition is based on the local characteristic time scale of the data to produce an adaptive basis and does not employ a set of fixed time scales.

Marginal spectrum, defined below in Eq. (2.3), provides a quantitative measurement of the cumulated weight of all the instantaneous frequency components over a specific time period,

$$f_{01}(\omega) = \int_{t0}^{t1} F(\omega, t)dt \tag{2.3}$$

where $f_{01}(\omega)$ is the cumulated weight of the frequency ω between times t_0 and t_1. It should be noted that the marginal spectrum defined in Eq. (2.3) describes and interprets the meaning of the frequency differently from Fourier spectrum does. In Fourier spectrum, presence of energy at a harmonic is interpreted as if the specific sinusoidal component is present throughout the entire duration of the time history. On the other hand, the marginal spectrum gives the cumulated weights of all instantaneous frequency components over a selected time span in the probabilistic sense, thus indicating the occurrence probability of the frequency components being considered [34].

2.3 Implication of Linearization in Time-Frequency Domain

To examine the impact of linearization, the responses of a nonlinear Duffing oscillator and its linearized version under stationary excitation are investigated by FFT, time-frequency analysis tools and IF. Analogous to complex nonlinear systems including the rolling motion of a ship, Duffing oscillators have the advantage of simplicity and can be investigated in sufficient detail. Of interest is the response of a particular Duffing oscillator subject to a harmonic excitation with viscous damping, which has been found to exhibit hysteretic and chaotic behaviors [40]. The general form of the non-dimensional Duffing oscillator is

$$\ddot{x} + 2\mu\dot{x} + \beta x + \alpha x^3 = a\cos(\omega t) \tag{2.4}$$

where μ, β, α, a, and ω are constants. When the motion is small, the cubic term can be linearized with respect to the equilibrium point zero and be ignored as

$$\ddot{x} + 2\mu\dot{x} + \beta x = a\cos(\omega t) \tag{2.5}$$

If $\beta - \mu^2 > 0$, the general solution can be simplified as

$$x(t) = \underbrace{Ae^{-\mu t}\cos\left(\sqrt{\beta - \mu^2}\,t + \theta\right)}_{transient} + \underbrace{\frac{a}{\sqrt{(\omega^2-\beta)^2+4\mu^2\omega^2}}\cos\,(\omega t - \theta)}_{steady\ state} \tag{2.6}$$

When $\mu < 1$, it is an underdamped system and the damped natural frequency is $\sqrt{\beta - \mu^2}$. The frequency of the steady state response ω is the same as the excitation frequency. In the followings the single-well Duffing oscillator investigated in [41] is adopted, with $\alpha = -1, \beta = 1$, $\mu = 0.2$, and the stationary excitation amplitude, a, being kept at 0.32 and excitation frequency at 0.78 rad/s. Fig. 2.1 shows the FFT of the linearized and nonlinear Duffing oscillators. It is hard to distinguish one from the other at first glimpse, and most would think both hold only one frequency at 0.12Hz.

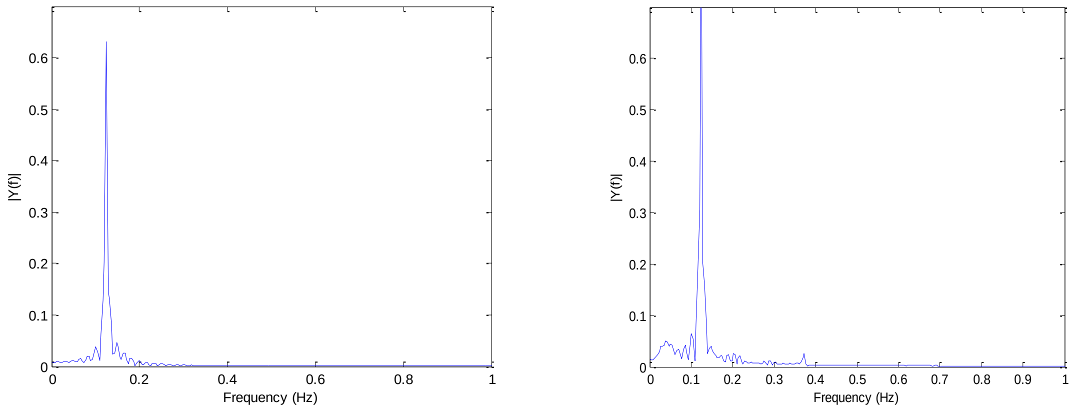

(a) (b)

Fig. 2.1 Fast Fourier transform of (a) linearized (b) nonlinear Duffing oscillator

Two time-frequency analysis methods, Short time Fourier transform (STFT) and Gabor wavelet transform are applied to investigate nonlinear and linearized responses as follows. Neither the dominant frequency nor the nonlinear effect is precisely resolved by STFT in Fig. 2.2. To improve the frequency resolution, one has to increase the width of the time window, thus inevitably resulting in poor time resolution. This dilemma is inherent of all Fourier-based time-frequency distribution. The Gabor wavelet transform [45] in Fig. 2.3 shows a better time-frequency resolution, however, it is still unable to differentiate the nonlinear response from the linearized one. As the only difference between these two spectra is the tiny irregular frequencies near the dominant frequency, which would be taken by most as the noise to be filtered, linearization would be adopted in a heartbeat. But the careless assumption that the response of the nonlinear system can be linearized, and afterwards be controlled, without further investigation could expose the system to the potential risk of abrupt break-down. Linearization, an approach generally accepted as the premise to dealing with nonlinear problems without caveat, in fact distorts the inherent underlying physical characteristics. A system could be falsely characterized, thus risking becoming unstable as a result.

IF provides an alternative look at the response in the simultaneous time-frequency domain. Fig. 2.4(a) shows the selected time history (top) of the linearized Duffing oscillator along with its extracted IMF C1 (middle) and residual R(t) (bottom). IMF C1, the mode containing the highest frequency components, is characteristically similar to the original time response that is a harmonic oscillation. The response of the linearized Duffing oscillator has only one frequency, thus resulting in only one IMF. According to the study in [34], the IF is exactly the reciprocal of the period in the IMF mode. Hence the steady-state IF of the C1 mode indicates a constant frequency at 0.124Hz as seen in Fig. 2.4(b), which coincides with the frequency $\omega = 0.78/2\pi$ Hz from the linearized model described in Eq. (2.5).

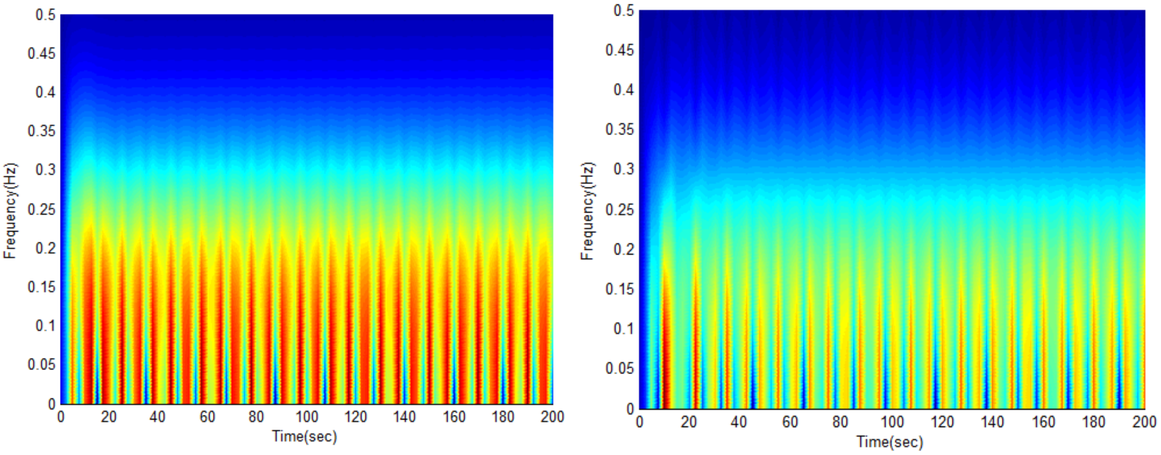

(a) (b)

Fig. 2.2 Short time Fourier transforms of (a) linearized and (b) nonlinear Duffing oscillators under stationary excitation (Sampling frequency = 2Hz)

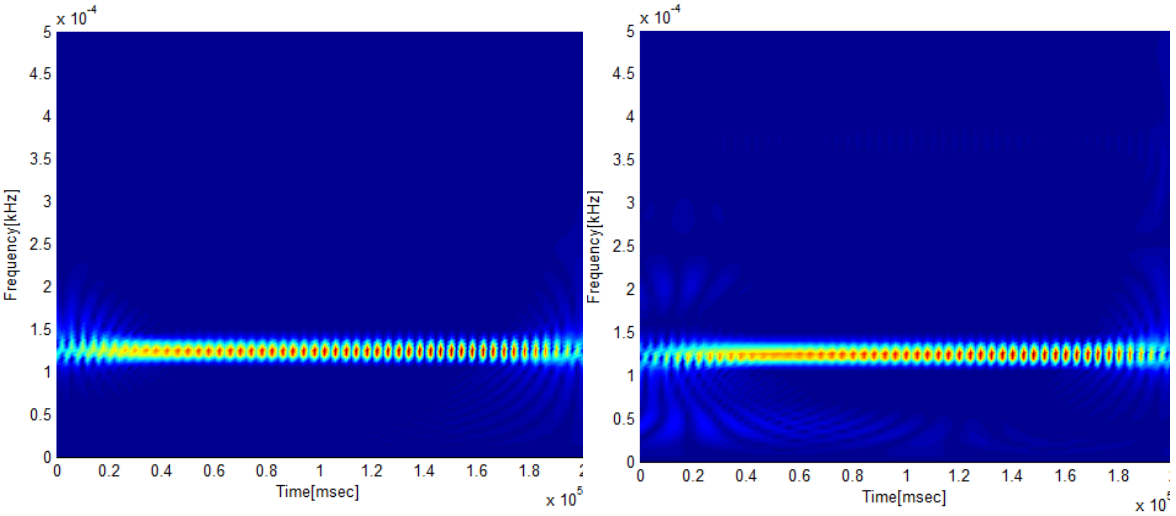

(a) (b)

Fig. 2.3 Gabor transforms of (a) linearized and (b) nonlinear Duffing oscillators under stationary excitation (Sampling frequency = 2Hz)

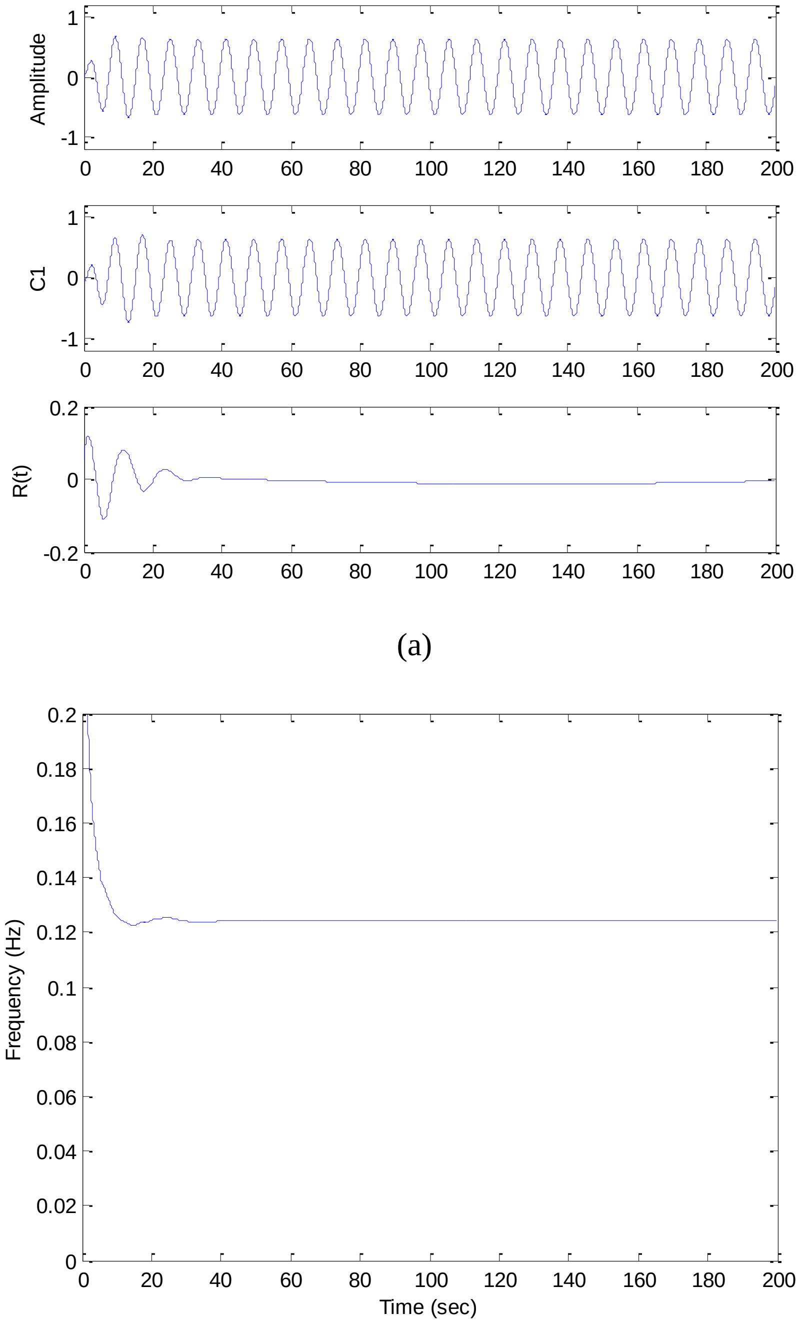

(a)

(b)

Fig. 2.4 (a) Time response and its IMFs and (b) IF of the linearized Duffing oscillator

The following analysis retains the cubic nonlinear term of the Duffing oscillator. The IMFs and IFs of the nonlinear Duffing oscillator in Eq. (2.4) are shown in Fig. 2.5. Although the IMF C1 waveform in Fig. 2.5(a) seems harmonic, the IF in Fig. 2.5(b) shows that it is not a harmonic, but rather displaying a simultaneously temporal-modal behavior oscillating periodically between 0.11 and 0.14 Hz with the mean value at 0.124 Hz, which happens to be the frequency of the linearized system. The IF points out that the frequency of the nonlinear response is not static but rather varying within a certain range. This is further asserted by reviewing the marginal spectrum which shows frequency distribution in the probabilistic sense. The marginal spectrum in Fig. 2.6(a) shows that there is a single frequency associated with the linearized Duffing oscillator. But for the nonlinear case in Fig. 2.6(b) there are multiple frequencies distributed between 0.11 and 0.14 Hz. Since a marginal spectrum is the occurrence probability of frequency components over a selected time span, it is evident that there are multiple frequency components in the response rather than a single frequency.

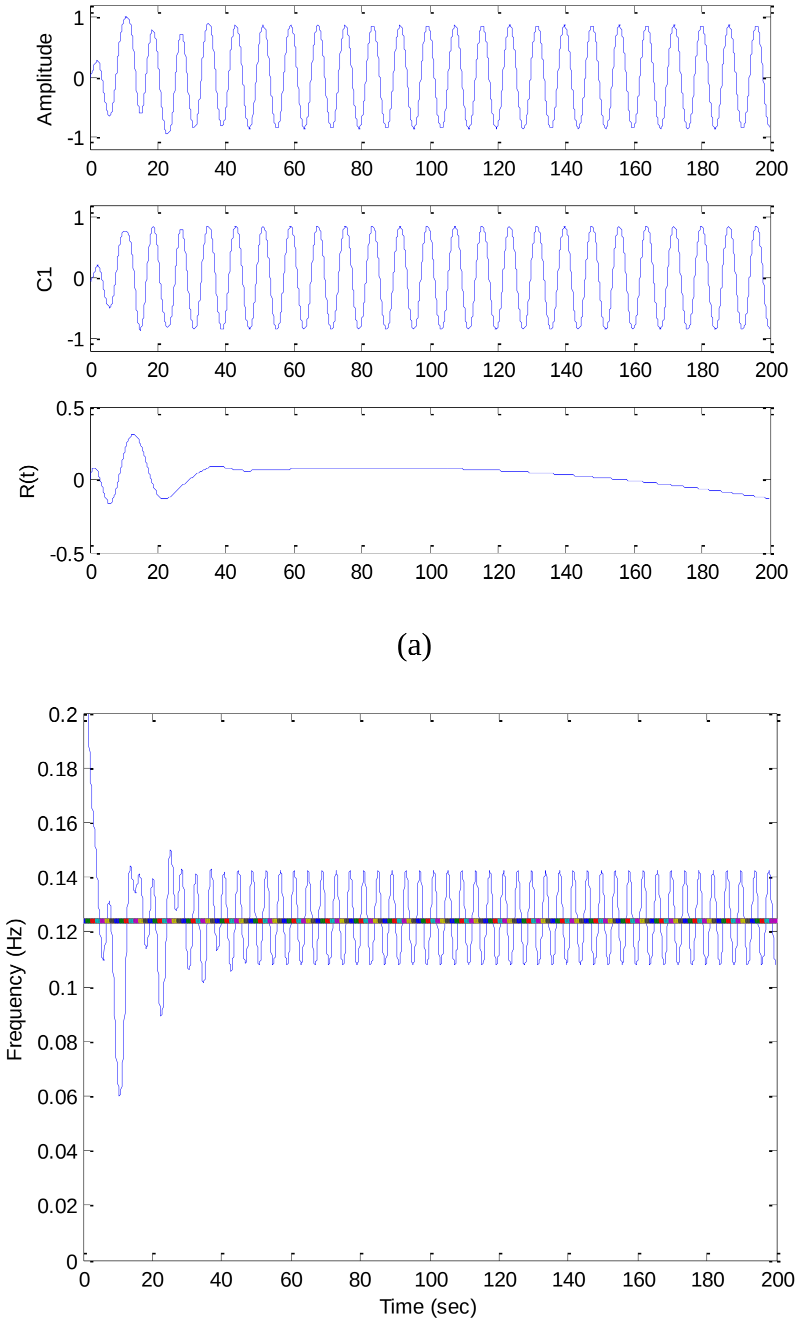

(a)

(b)

Fig. 2.5 (a) Time response and its IMFs (b) IF of the nonlinear Duffing oscillator

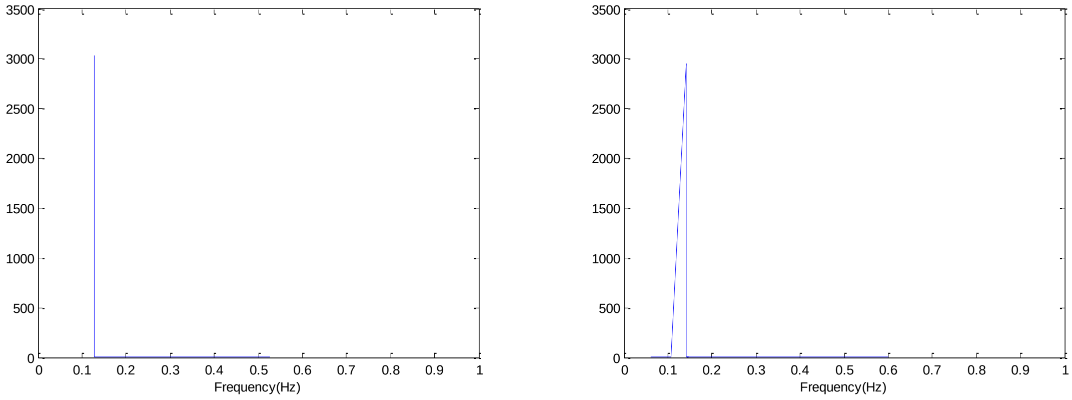

(a) (b)

Fig. 2.6 Marginal spectrum of (a) linearized and (b) nonlinear Duffing oscillator

Two observations can be made. First, the Fourier spectrum is unable to reveal the true characteristic of the nonlinear response. Second, by comparing the marginal spectra of the nonlinear and linearized responses, it is observed that linearization in fact misinterprets nonlinear features, replacing multiple frequencies with a single frequency. The false representation of spectral characteristics implies that the common frequency-domain-based controllers designed using linearization would misinterpret the frequency response, thus incapable of realizing the ongoing evolution of bifurcation. Since route-to-chaos is a transient progress in which spectral response deteriorates from being periodic to aperiodic and broadband, linearization and Fourier based controller design would most certainly fail to identify the inception of bifurcation and chaos, and the stability bound of the system.

2.4 Route-to-Chaos in Time-Frequency Domain

Unlike the nonlinear response due to stationary excitation, the one induced by nonstationary excitation is a temporal transition from bifurcation to chaos with a time-varying spectrum. Conventional tools including bifurcation diagram, phase portrait and Poincaré section are used to investigate the route-to-chaos in contrast to the result obtained by IF. The Duffing oscillator of single potential well in Eq. (2.4) is again considered, but with a time-increasing excitation amplitude. When the amplitude is small, the response is bounded and remains in the valley of the potential well. When the external excitation gradually increases, the response, whose amplitude may still be bounded, could jump to an unbounded solution after it passes a critical limit – a phenomenon similar to the catastrophic capsizing of a marine vessel. The excitation amplitude in Eq. (2.4) is considered as the control parameters, with all other coefficients ($\alpha = -1, \beta = 1,$ and $\mu = 0.2$) follow from Ref. [43], where a stationary bifurcation diagram of a Duffing oscillator was generated using multiple scales and Floquet theory. Again the excitation frequency is held at 0.78 rad/s. The excitation amplitude is a linear time function, $a = 0.32 + 10^{-7} t$. Thus the response is bounded within the potential well, and the slow increasing of the amplitude ensures that the bifurcation process can be clearly observed. By making the amplitude a function of time, a nonstationary bifurcation diagram is constructed in Fig. 2.7. While agreeing with the result in [38], the figure also indicates the penetration effect and the elimination of the stationary discontinuities.

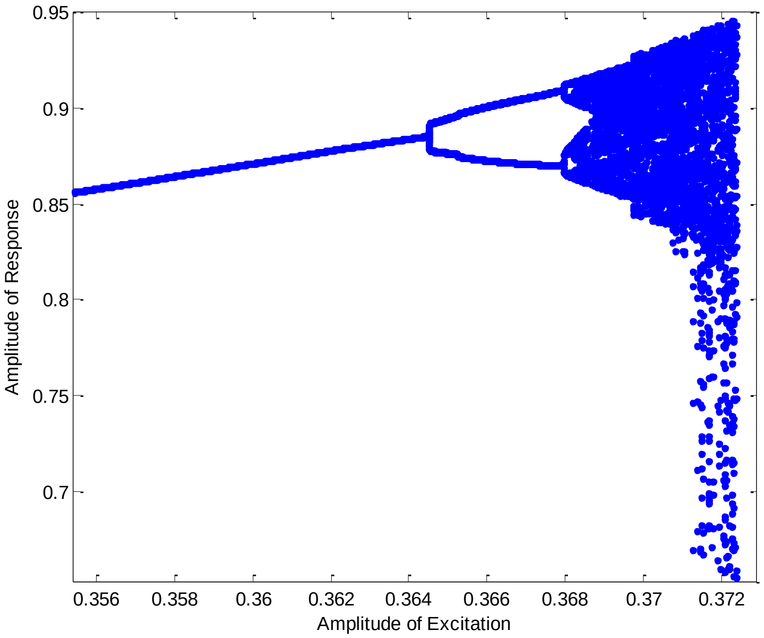

Fig. 2.7 Nonstationary bifurcation diagram with increasing excitation amplitude

In general the bifurcation depicted in Fig. 2.7 can be divided into three stages before becoming unbounded. The stage of singular frequency is the first stage which existed when the excitation was first applied. At this stage each value of the excitation amplitude refers to only one point in the bifurcation diagram, meaning that there is only one frequency at any time instance, though this frequency may not be static. When excitation amplitude increases, period-doubling is observed. When multiple periods show up, it is the third, fractal stage. Within this stage spectral bandwidth increases, but remains bounded. When excitation amplitude exceeds 0.3725, the response becomes unbounded. In addition to the bifurcation diagram, phase portraits and Poincaré sections are plotted to help resolve the bifurcation-to-chaos progression in time. Fig. 2.8(a) shows a close-trajectory phase portrait and a corresponding single-dot Poincaré section, representing a periodic response with single frequency. A 2T period doubling bifurcation and a 4T period doubling bifurcation are seen in Fig. 2.8(b) and (c), respectively. Fractal structures emerge from Fig. 2.8(d) and deteriorate in Fig. 2.8(e) before the response becomes unbounded. However, it is difficult to make out the motion states due to the overlapping of the trajectories, thus highlighting the inability of phase portraits and Poincaré sections in capturing the transient phenomena of the route-to-chaos process. Other than showing the qualitative transition from bifurcation to chaos, the bifurcation diagram does not provide any further information.

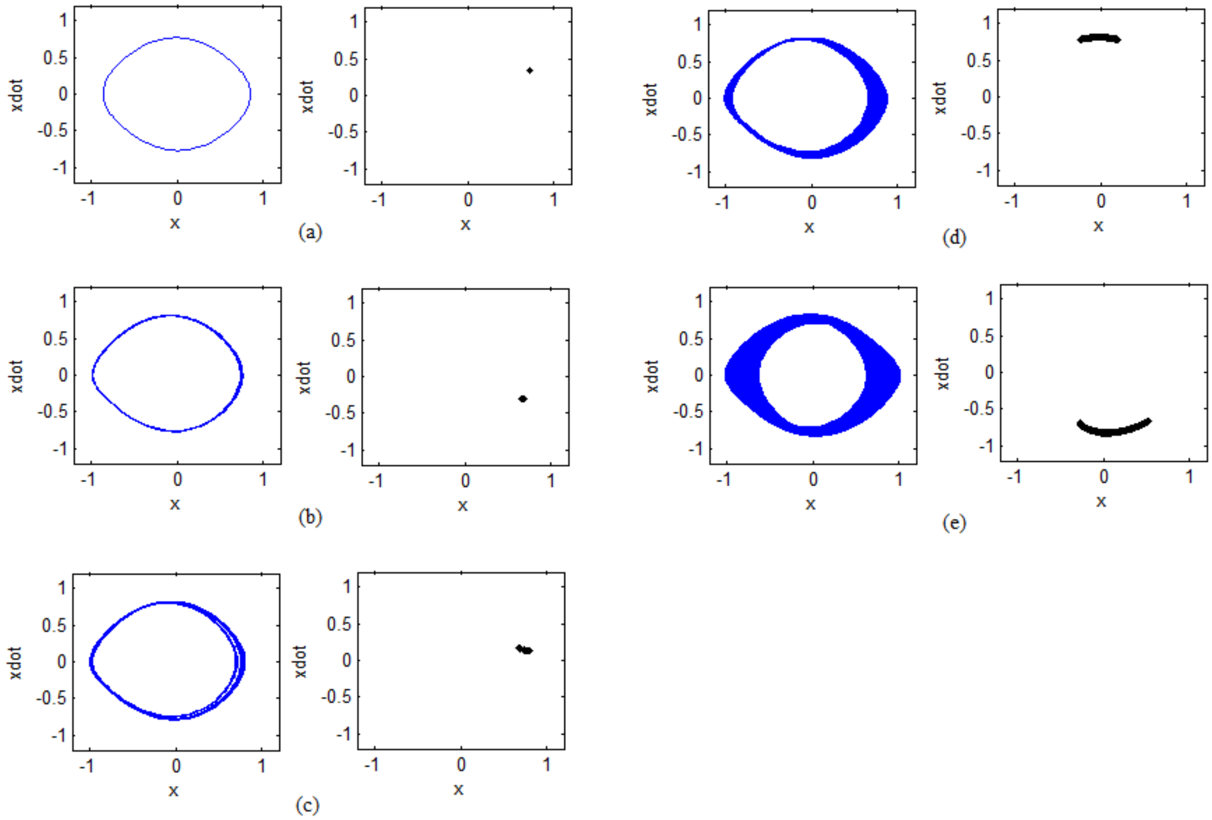

Fig. 2.8 Phase portrait and Poincaré section for (a) periodic motion (b) 2T period doubling bifurcation (c) 4T period doubling bifurcation (d) fractal (e) fractal before unbounded

Responses in Fig. 2.8 are further evaluated using FFT and marginal spectrum. The FFT of the periodic motion in Fig. 2.9(a) indicates a frequency component at 0.142 Hz, while the marginal spectrum shows that the frequency is not static but rather oscillates between 0.11 and 0.14 Hz, which is a primary characteristic of a nonlinear response. As the excitation amplitude increases, a second cluster of frequencies appears in the marginal spectrum in Fig. 2.9(b), while the FFT still shows a single frequency. The same observation is made to the 4T period doubling bifurcation in Fig. 2.9(c). Furthermore, the marginal spectra in Figs. 2.9(d) and (e) indicate a high probability of frequency occurrence between 0 and 0.05 Hz. It indicates that the response frequency proliferates to be broadband and undergoes a route-to-chaos process, while the corresponding FFT is incapable of resolving the changing process. In addition, noticeable fictitious high frequencies emerge in Figs. 2.9(b), (d), and (e). These artificial high frequencies stem from using superharmonic components to fit the dynamic response in FFT – a result of averaging and eliminating the subharmonic frequencies of the real signal. The result shows that FFT could be non-physical and misinterpreting the true response. Instantaneous frequency is then applied to the selected time segments to scrutinize the three stages that are characterized, respectively, by a singular frequency, period doubling bifurcation, and fractal. A fixed time window of 200sec is applied to ensure a better resolution. Several figures are followed to illustrate the time-progression of the periodic motion, 2T period doubling bifurcation, 4T period doubling bifurcation, and route-to-chaos. Fig. 2.10 shows the IFs along with its corresponding IMFs of the singular frequency stage. It is found that this stage, previously considered as a periodic motion by phase portrait and Poincaré section, actually has oscillating frequencies indicative of nonlinearity. It is surprising to compare the IF of the one under nonstationary excitation with the one under stationary excitation. Although the nonstationary excitation amplitude is increased slowly with a rate of only 10^{-7} per second (whose time responses/waveforms are similar to those in Fig. 2.5), their IFs show differences. Comparing the IFs in Fig. 2.10(b) with the one in Fig. 2.5(b), it is clear that IF is capable of resolving even the slightest shift of the system that was not revealed using all previous methods.

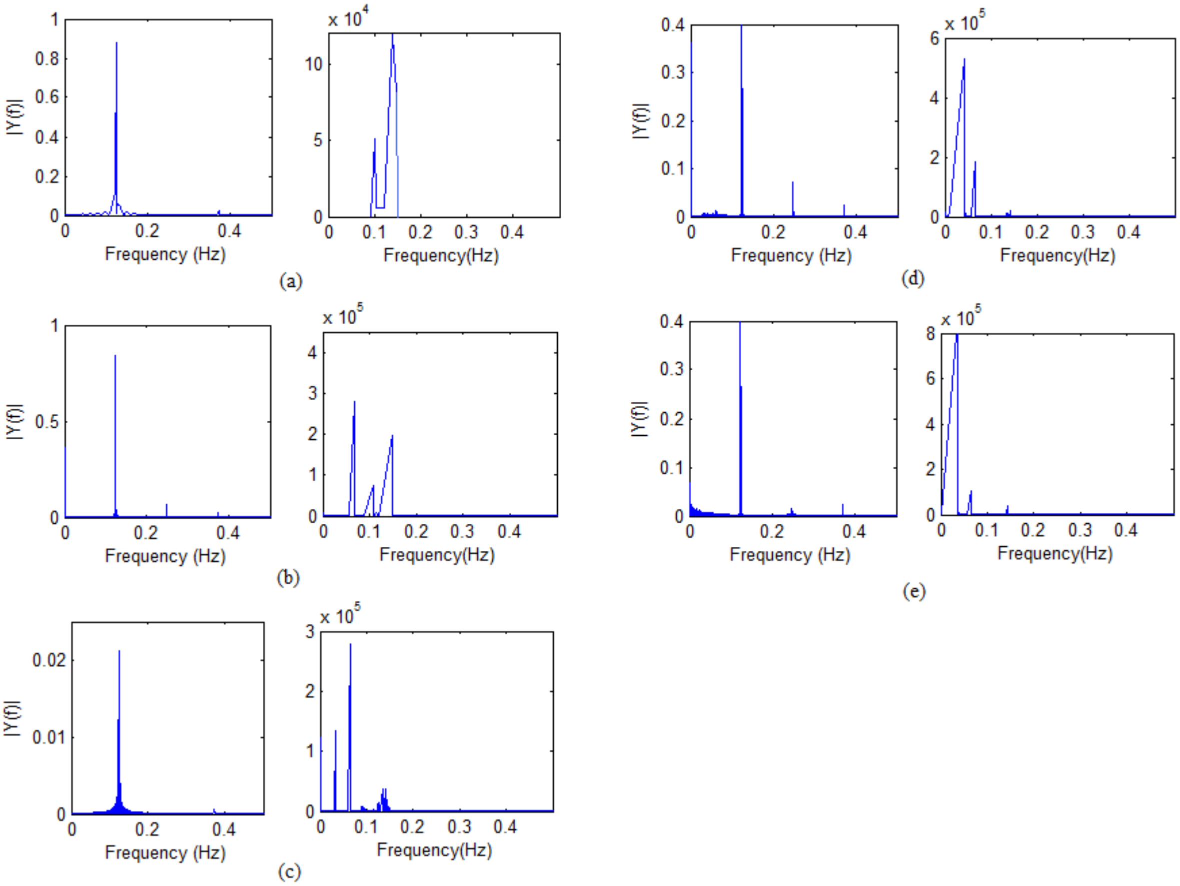

Fig. 2.9 FFT and marginal spectrum for (a) periodic motion (b) 2T period doubling bifurcation (c) 4T period doubling bifurcation (d) fractal (e) fractal before unbounded

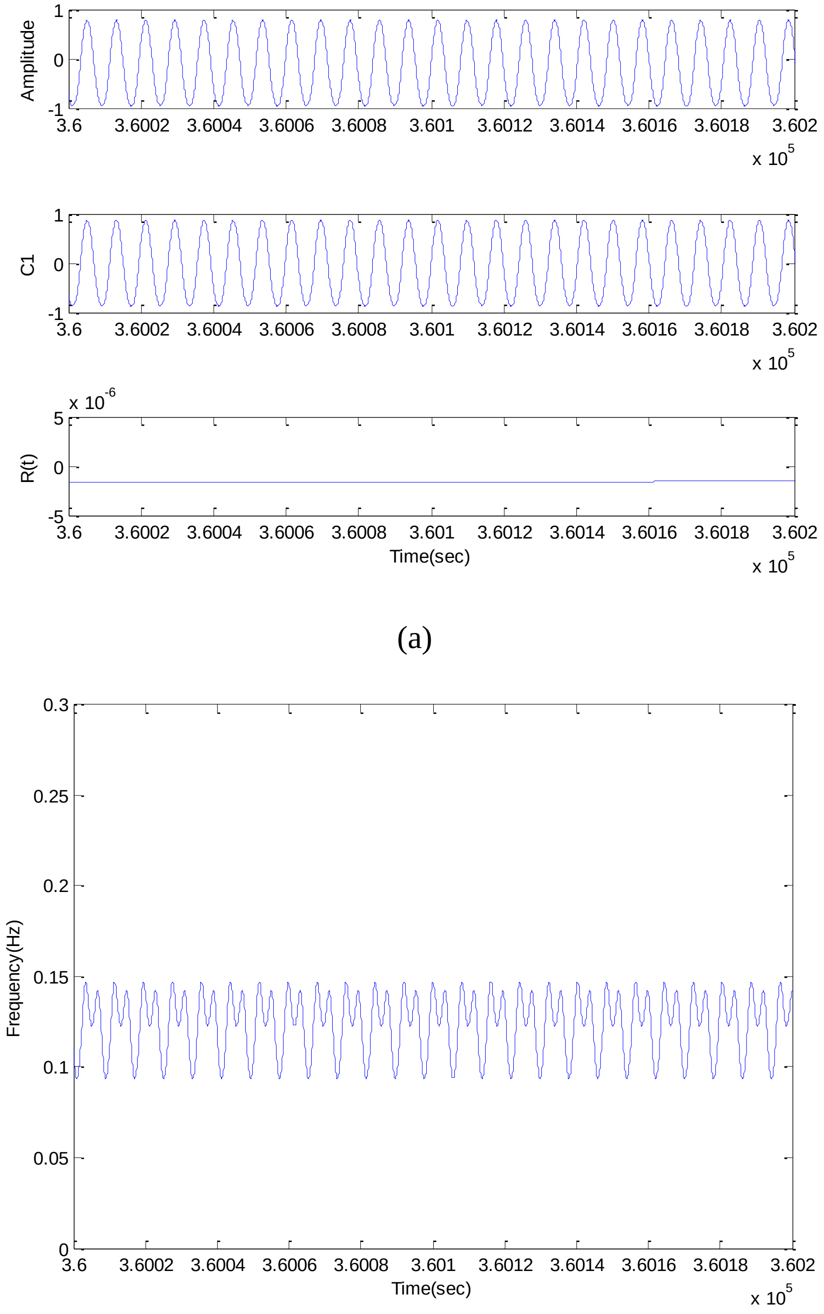

(a)

(b)

Fig. 2.10 (a) Time response and its IMFs, (b) Instantaneous frequencies of the stage of singular frequency (single frequency for each time point)

As the excitation amplitude increases further, the response undergoes a 2T period doubling bifurcation. The first IMF mode, C1, is similar to the time response, and the corresponding IF looks identical to the IF associated with the singular frequency stage. The C2 mode emerges with increasing amplitude. Its IF in Fig. 2.11 indicates a second frequency oscillating about 0.06 Hz, which is half of the frequency of the first mode, thus a period doubling bifurcation. However, both frequencies are not static, but displaying a temporal-modal structure oscillating periodically and showing rich nonlinearities. Fig. 2.12 shows a 4T period doubling bifurcation. Two more IMF modes, C3 and C4, emerge. All of them look like harmonic oscillations, but none possesses constant periodicity. In Fig. 2.12(b), two new frequencies are generated with a less vigorous oscillation comparing to the first two instantaneous frequencies.

The instantaneous frequency of the fractal structure is illustrated in Fig. 2.13(b). Unlike the IFs in the 4T period-doubling bifurcation where relatively regular temporal-modal oscillations were observed, all IFs follow no well-defined pattern or structure. All IMF modes, C1, C2, C3, and C4, lose their previous characteristics and show varying amplitude and period. The corresponding IFs exhibit highly irregular temporal-modal oscillations with large amplitude, especially for the high frequencies generated from the first two IMFs. These IFs oscillate with significant mutual-crossings, rendering a broad spectrum of a larger number of frequencies.

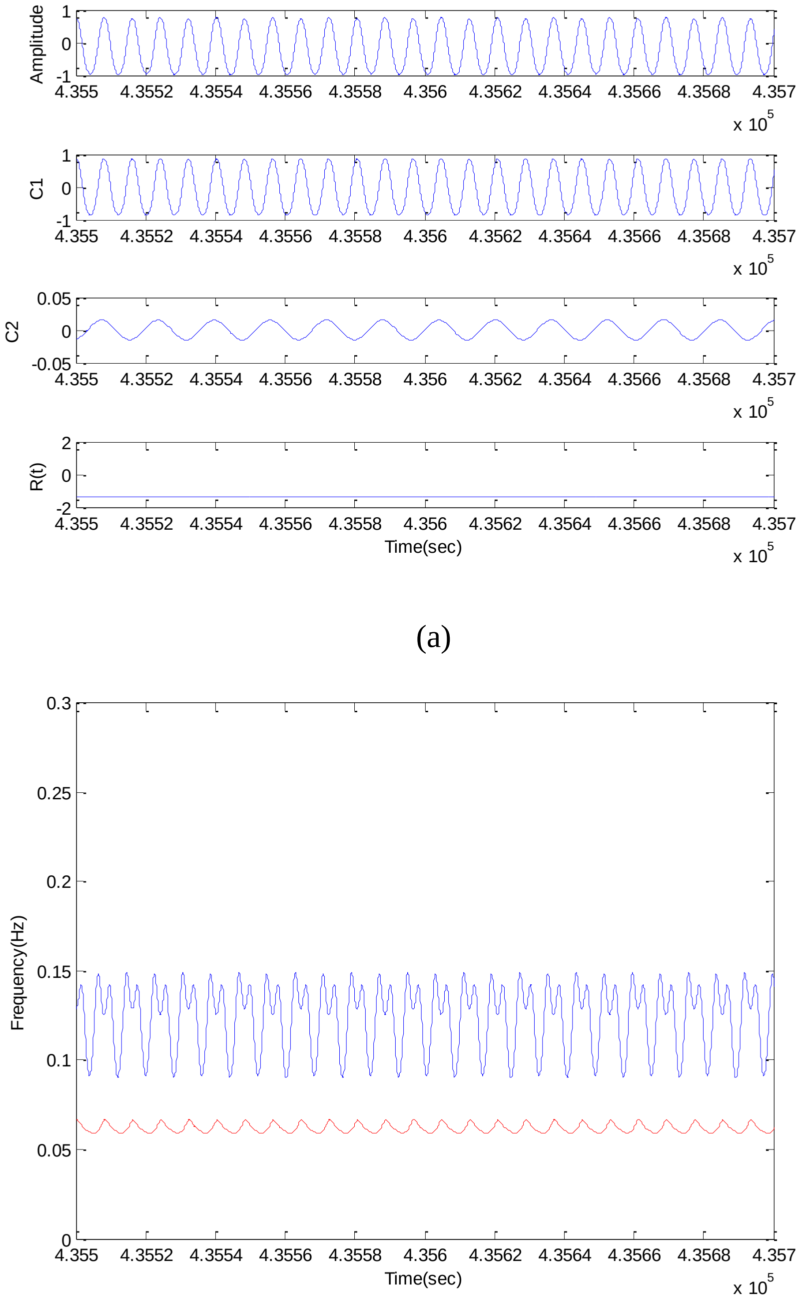

(a)

(b)

Fig. 2.11 (a) Time response and its IMFs, (b) Instantaneous frequencies of the 2T period doubling bifurcation

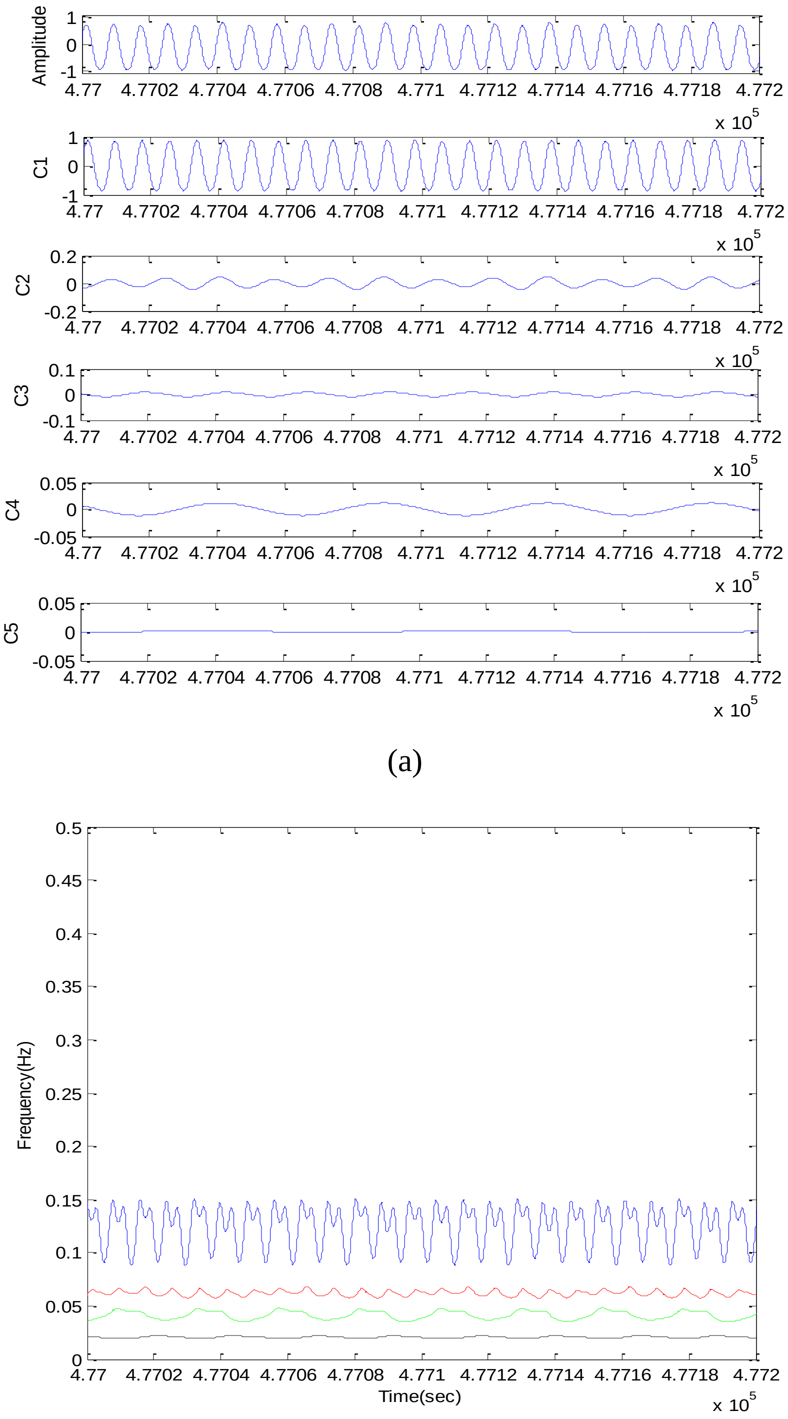

(a)

(b)

Fig. 2.12 (a) Time response and its IMFs, (b) Instantaneous frequencies of the stage of 4T period doubling bifurcation

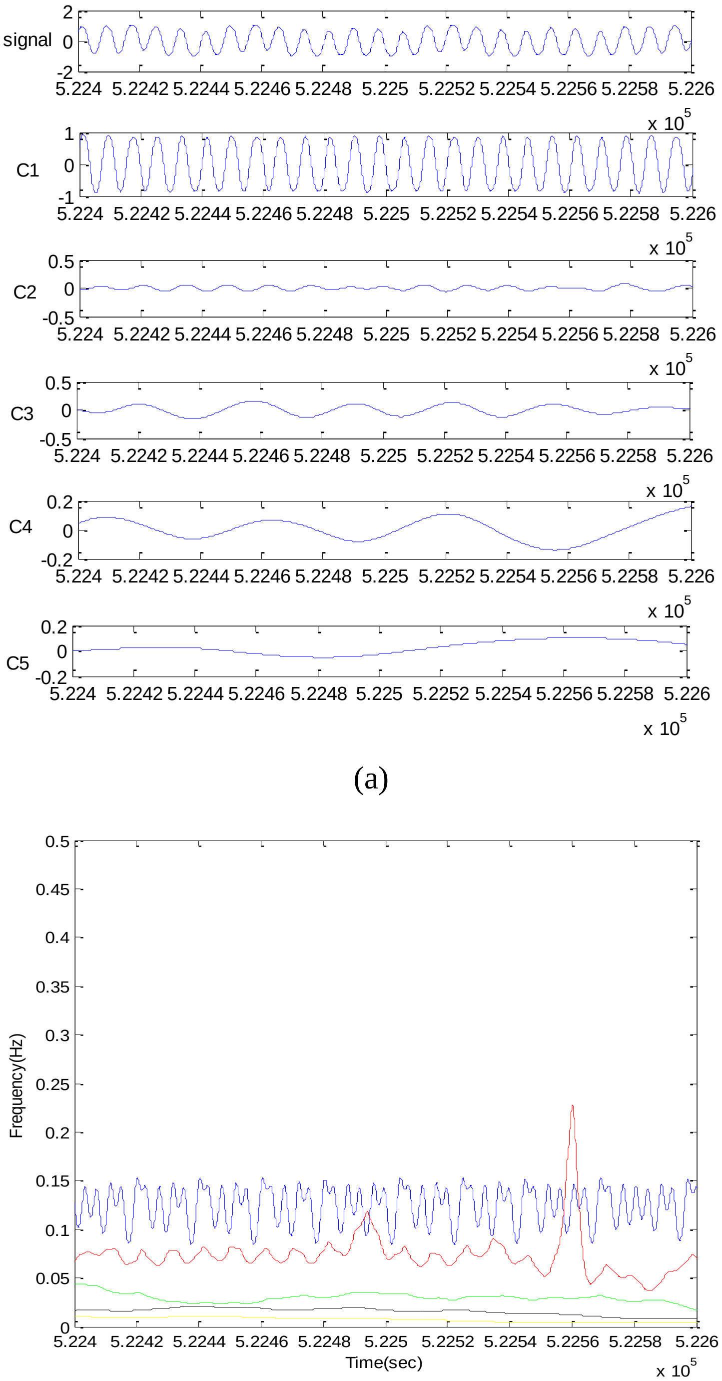

(a)

(b)

Fig. 2.13 (a) Time waveform and its IMFs, (b) Instantaneous Frequencies of the stage of fractal

2.5 Summary

A softening Duffing oscillator was investigated for its intrinsic time-frequency characteristics. It was shown that linearization disregarded the inherent nonlinear attributes, hence inevitably misjudging the underlying physics of the nonlinear response. In addition, as it employs static sinusoids as the fundamental constituents, FFT generated fictitious frequencies in the process of attempting to approximate the nonlinear response mathematically. Both methods inexorably misinterpreted and obscured the genuine characteristic of the responses that were transient, nonlinear, and full of modulated amplitude and frequency. Instantaneous frequency was then applied to investigate the responses of a softening Duffing oscillator undergoing nonstationary excitation. The temporal progression of route-to-chaos was interpreted with vigorous physical intuition using the fundamental concept of instantaneous frequency. It was shown that the frequency of the nonlinear Duffing oscillator was a temporal-modal oscillation and that the inception of period-doubling bifurcation and the deterioration of route-to-chaos were precisely identified. Instantaneous frequency was shown to provide intuitively vigorous and physically valid interpretation of the nonlinear response, implying that time-varying, transient processes fundamental of bifurcation and chaotic response need to be established in the simultaneous time-frequency domain.

3. SIMULTANEOUS TIME-FREQUENCY CONTROL OF BIFURCATION AND CHAOS*

3.1 Introduction

The review on the chaos control of non-autonomous, nonstationary systems in Section 1 provides several hints essential to the development of a viable control solution. The solution can be formulated by recognizing the various attributes inherent of a chaotic system, including the simultaneous deterioration of dynamics in both the time and frequency domains when bifurcates, nonstationarity, and sensitivity to initial conditions. For a linear time-invariant system, only the amplitude and the phase angle of the excitation input vary. The response frequency remains the same with respect to the input frequency, and the system can be stabilized by applying a proper feedback gain. Both time- and frequency-domain responses are bounded. However, this is not the case for the chaotic response generated by a chaotic system, which contains an infinite number of unstable periodic orbits of all periods called strange attractors. Chaotic response doesn’t remain following one periodic orbit but switching rapidly between many unstable periodic orbits. If the chaotic response is projected into a Poincaré section, a lower dimensional subspace transversal to the trajectory of the response, it can

---

*Part of this chapter is reprinted with permission from “Simultaneous Time-Frequency Control of Bifurcation and Chaos” by Liu, M. K. and Suh, C. S., 2012, Communications in Nonlinear Science and Numerical Simulations, 17(6), pp. 2539-2550, Copyright 2012 by Elsevier be shown that the intersection points congregate densely and are confined within a finite area. It indicates that the chaotic response is bounded in the time-domain while simultaneously becoming unstably broadband in the frequency-domain due to the rapid switching between infinite numbers of UPOs. Hence, for a chaos control algorithm to be effective, control has to be performed in the time and frequency domains simultaneously.

The second property universal of chaotic systems is nonstationarity. Route-to-chaos is a temporal, transient process. The location and the stability of the equilibrium point therefore also vary in time. For high dimensional system, a priori knowledge of the system is often hard to come by. It is thus necessary for a viable chaos control scheme to conduct on-line identification and control at the same time in order to cope with the time varying parameters of the system. The third property is the sensitivity of a chaotic system to initial conditions. A minor deviation between two closed initial trajectories might diverge exponentially with the increase of time, thus implying that a small perturbation could render the system unstable. Reversely, a nonlinear system can also be stabilized by a small perturbation, as implied by open-loop chaos control theories of early days that it is possible to stabilize a chaotic system by giving small perturbations to its input or system parameters.

A solution with physical features effective in addressing the identified properties is described below. To address the need for providing simultaneous time and frequency resolution, Parseval’s theorem is turned to for inspirations, which states that the total energy computed in the time-domain equals the total energy computed in the frequency-domain, thus implying that it’s possible to incorporate time-domain control with frequency-domain control together. Wavelet transform (WT) localizes a time event and detects the ensued changes in the wavelet domain, which is essentially a simultaneous time-frequency domain. Unlike Fourier analysis that approximates signals using sinusoids, WT uses finite, compact-supported orthogonal functions and provides localized time and frequency resolution through the translation and dilation of a base wavelet function. Efforts have been reported on incorporating discrete WT in control theory that explored (wavelet) multiresolution through employing iterative filter banks. A wavelet filter bank runs a signal through two parallel channels, filtering one channel with a high-pass filter and the other with a low-pass filter, and then down-samples the signal by two. Control algorithms presented in Refs [46-49] were all constructed using wavelet coefficients by multiresolution analysis. They all reported improved transient performance. Discrete wavelet transform (DWT) was incorporated with neural network to indentify unknown systems in real-time [50-55], where adaptive control rules were applied. Relieved computational load and higher accuracy for system identification were among the benefits. Ref [56] applied DWT to replace the long-standing higher-order Taylor series approach. Such a method reduces complexity and increases efficiency, but it is only applicable for linear models. In general, the coefficients of multiresolution analysis inherently carry simultaneous time-frequency information. Additionally, down-sampling in filter banks operation greatly reduces the amount of data and thus shortens the computation time.

3.2 Simultaneous Time-Frequency Control

To address the nonstationary nature of a chaotic system the concept of active noise control [57] is adopted. Active noise control puts a control algorithm driven loudspeaker near the sound source to attenuate the sound. The sound source is cancelled by the sound emitted by the loudspeaker which has the same amplitude as the source but of an opposite phase. The most commonly used algorithm is the filter-x lease mean square (FXLMS) algorithm, whose block diagram is shown in Fig. 3.1.

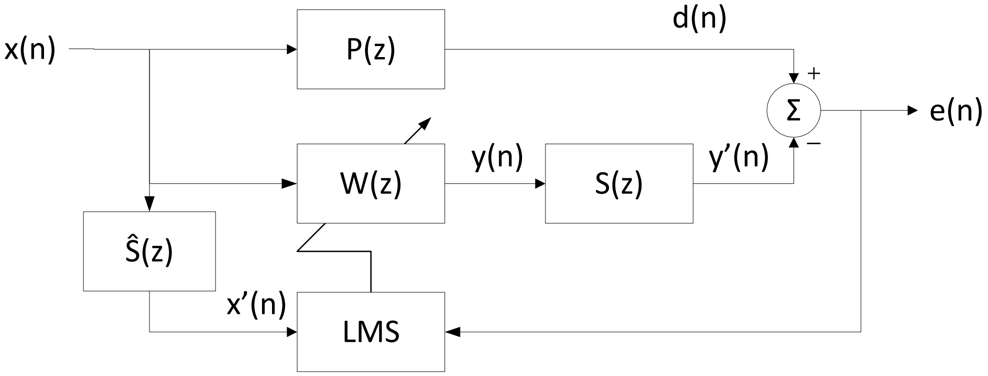

Fig. 3.1 FXLMS algorithm

The primary path P(z) defines the path from the reference source x(n) to the error sensor where the noise attenuation is to be realized. The adaptive filter W(z) provides an adaptive method to simultaneously model the primary plant P(z) and the secondary path S(z) with a given input source to minimize the residual noise e(n). To ensure the convergence of the LMS algorithm, an identical filter $\hat{S}(z)$ is positioned in the reference source path to the weight update of the LMS algorithm. In addition to noise control, FXLMS has been used to suppress the vibration of composite structure [58], gear pairs [59], building [60], and machine tool [61]. FXLMS could also be combined with other controllers, such as H_∞ feedback robust controller [62] and LQR controller [63], to promote convergence speed and increase robust performance. Even though FXLMS uses a feedforward adaptive filter to change the input according to the error, it still needs off-line identification of a system as a priori information. However it can be modified by adding another adaptive FIR filter to identify the system in real-time. Multiresolution analysis can be integrated into the on-line FXLMS structure by putting analysis filter banks in front of the adaptive filters to manipulate wavelet coefficients, and then use synthesis filter banks to reconstruct the control signal. Scheme of such a construct that possesses joint time-frequency resolution and follows the on-line FXLMS algorithm is able to control non-autonomous, nonstationary systems.

3.2.1 Time Domain Discrete Wavelet Transformation

Simultaneous time-frequency control can be realized through manipulating the discrete wavelet coefficients in the time domain [64, 65]. Implementation of such a novel control idea includes incorporating discrete wavelet transform (DWT) with Least Mean Square (LMS) adaptive filters to perform feedforward control, on-line identification [66], and adopting Filter-x Least Mean Square (FXLMS) algorithm [67] to construct a parallel adaptive filterbank. DWT in time domain can be realized by passing the signal through a two-channel filter bank iteratively, as the one shown in Fig. 3.2.

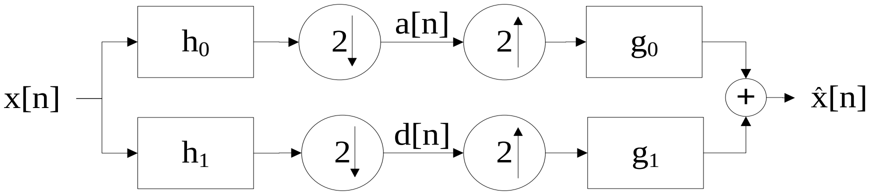

Fig. 3.2 Two-channel filter bank in time domain

Assume that the infinite input signal x[n] is of real numbers. The decomposition process in Fig. 3.2 convolutes the input x[n] with a high-pass filter h_0 and a low-pass filter h_1, followed by down-sample by two. The approximation coefficient a[n] and detail coefficients d[n] it received are calculated in the time domain as follows

$$a[n] = \sum_k h_0[2n-k]x[k] = \sum_k h_0[k]\,x[2n-k] \tag{3.1}$$

$$d[n] = \sum_k h_1[2n-n]x[k] = \sum_k h_1[k]x[2n-k] \tag{3.2}$$

where integer $n = 0, \ldots, \infty$. Orthogonal filter sets with equal, even length are used and the lengths of the high-pass filter h_0 and low-pass filter h_1 are both 4.

3.2.2 Integration of DWT Transform and LMS Adaptive Filter

Fig. 3.3 gives the schematics of one of the most widely used finite impulse response (FIR) filters is briefly reviewed in the followings. Given a set of N filter coefficients, $w_j(n), j = 0, 1, \ldots, N-1$, and a data sequence, $\{x(n), x(n-1), \ldots, x(n-N+1)$, the output signal is computed using

$$y(n) = \sum_{k=0}^{N-1} w_k(n) \cdot x(n-k) \tag{3.3}$$

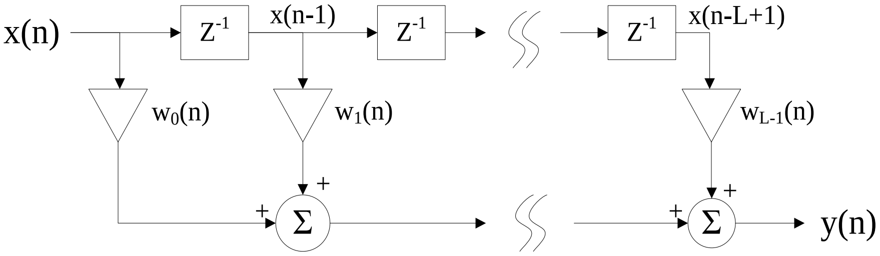

Fig. 3.3 Block diagram of digital FIR filter

The input vector and weight vector at time *n* can be defined as *X(n)* and *W(n)*, respectively.

$$X(n) = [x(n)\ \ x(n-1)\ \ \ldots\ \ x(n-N+1)]^T \tag{3.4}$$

$$W(n) = [w_0(n)\ \ \ w_1(n-1)\ \ \ \ldots\ \ w_{N-1}(n-N+1)]^T \tag{3.5}$$

Consider an $N \times N$ DWT transformation matrix, *T*. The output signal *y(n)* can be calculated and then compared with the desired response to determine the error signal through the following operations

$$y(n) = W^T(n)TX(n) \tag{3.6}$$

$$e(n) = d(n) - y(n) \tag{3.7}$$

The steepest-descent method is used to minimize the mean-square-error of the error signal. The least-mean-square (LMS) algorithm is used to update the weight vector as follows

$$w(n+1) = w(n) + \mu x(n)e(n) \tag{3.8}$$

where μ is the step size for the control of stability and convergence speed. A linear dispersive channel described in [68] that produces unknown distortion with a random sequence input $\{x_n\}$ is used to compare the performance of the wavelet-based LMS with

LMS, normalized LMS (NLMS), and recursive least squares (RLS) [68]. The impulse response of the channel is described by the raised cosine as follows

$$h_n = \begin{cases} \frac{1}{2}\{1+\cos[\frac{2\pi}{W}(n-2)]\}, & n = 1, 2, 3 \\ 0, & otherwise \end{cases} \tag{3.9}$$

where parameter W = 3.7 controls the amount of amplitude distortion produced by the channel. The signal-to-noise ratio is about 30dB and the filter tap is 32. The Level-1 Daubechies D4 wavelet is employed to show in Fig. 3.4 that the wavelet-based LMS is of a better convergence performance.

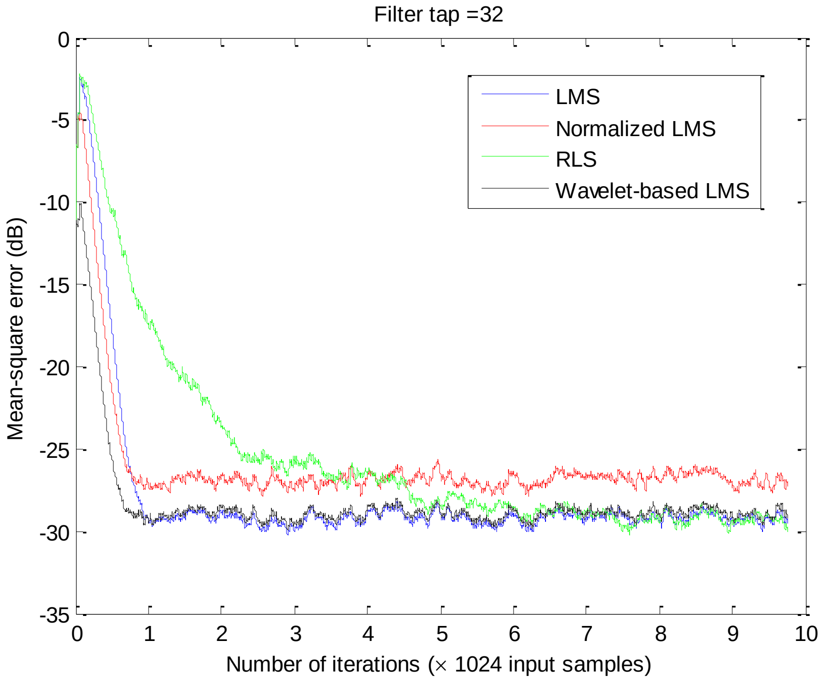

Fig. 3.4 Performances of LMS, NLMS, RLS and wavelet-based LMS

3.2.3 Simultaneous Time-Frequency Control Scheme

The FXLMS algorithm is a modification to the LMS algorithm [57]. Fig. 3.5 is an example of how FXLMS is applied to neutralize the noise inside a signal-channel duct-acoustic system. The noise source (reference input) is picked up by the reference microphone in the upstream, and an error microphone placed in the downstream is used to monitor the noise in the output. The reference signal *x(n)* and error signal *e(n)* are processed by active noise controller implemented by the FXLMX algorithm. It generates a control signal *y(n)* to drive a loudspeaker in order to cancel the noise.

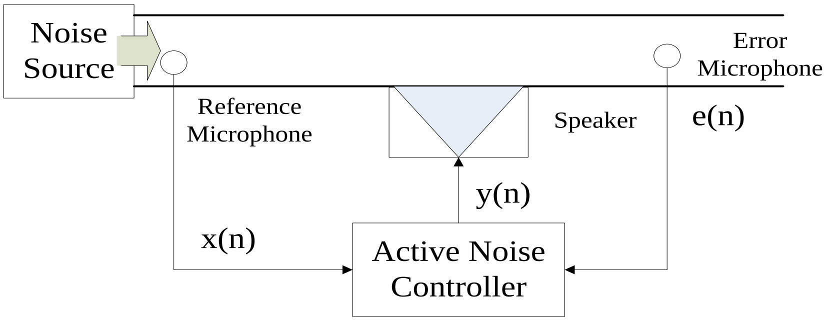

Fig. 3.5 Signal channel broadband feedforward active noise control system in a duct [57]

The concept of FXLMS is adopted and modified though with a different objective. FXLMS is based on the principle of superposition. Its adaptive filter uses the noise acquired near the source as a reference to generate a compensating signal that cancels the noise. The residual error is then exploited to adapt the coefficients of active filter to minimize the mean-square-error. This concept is followed to construct a wavelet-based time-frequency controller with parallel on-line modeling technique. The wavelet transformation matrix T is placed in front of two FIR adaptive filters to convert the time domain discrete signal into wavelet coefficient array. The wavelet coefficients are multiplied by the weights of the FIR filter and then summed up to reconstruct the time domain signals.

To incorporate the $N \times N$ transformation matrix T and the length-N adaptive filters, signal vectors are defined as

$$X(n) = [x(n) \quad x(n-1) \quad \cdots \quad x(n-N+1)]^T \tag{3.10}$$

$$U(n) = [u(n) \quad u(n-1) \quad \cdots \quad u(n-N+1)]^T \tag{3.11}$$

$$X'(n) = [x'(n) \quad x'(n-1) \quad \cdots \quad x'(n-N+1)]^T \tag{3.12}$$

$$E(n) = [e(n) \quad e(n-1) \quad \cdots \quad e(n-N+1)]^T \tag{3.13}$$

$$F(n) = [f(n) \quad f(n-1) \quad \cdots \quad f(n-N+1)]^T \tag{3.14}$$

These signal vectors are updated by adding the incoming data and dropping the N_{th} data in the array at each iteration.

3.2.4 Optimization of Parameters

Performance of the wavelet-based active controller depends on the selection of parameters such as the mother wavelet and the decomposition level. Two time domain indicators, kurtosis and crest factor, are optimized to identify the parameters that best represent the characteristics of the driving signal [69].

$$Kurtosis = \frac{\frac{1}{N}\sum_{n=1}^{N}(x(n)-\bar{x})^4}{[\frac{1}{N}\sum_{n=1}^{N}(x(n)-\bar{x})^2]^2} \tag{3.15}$$

$$Crest\ Factor = \frac{Crest\ Value}{RMS} = \frac{sup|x(n)|}{\sqrt{\frac{1}{N}\sum_{n=1}^{N}[x(n)]^2}} \tag{3.16}$$

where *x(n)* is the signal, *N* is the number of the samples, and $\bar{x}$ is the sample mean. The values of these two indicators that correspond to the Daubechies wavelet family [70] and decomposition level are shown in Fig. 3.6, which indicates that the Daubechies D6 (db3) wavelet best characterizes the signal given that it has the highest kurtosis and crest factors. Even though the decomposition level 5 has the highest Kurtosis value, decomposition level one is selected to ease the computational load.

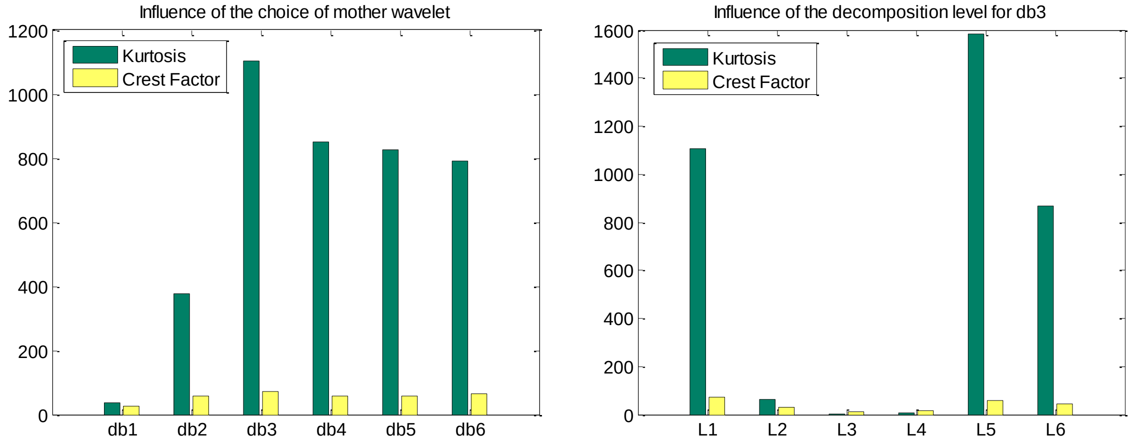

(a) (b)

Fig. 3.6 Selection of (a) mother wavelet and (b) decomposition level

When the wavelet-based active controller is applied to a system undergoing bifurcation, it is able to restrain both the time and frequency domain responses and keep the system in periodic motion. Hence the mitigation imposed by the controller effectively stabilizes the dynamics before it deteriorates dynamically to eventual chaos. Having the concepts of adaptive control, active noise control and wavelet-based FIR filters all integrated, the wavelet-based active controller exerts control in the joint time-frequency domain and therefore differentiates itself from all published controllers in philosophy, architecture, and performance in mitigating nonlinear non-stationary responses such as bifurcation and route-to-chaos.

3.3 Numerical Experiment

The philosophy of the proposed control scheme is that the controller must be able to inhibit the deterioration of time and frequency responses simultaneously before the frequency response is too broadband to be controlled. It employs adaptive filters for real-time system identification to cope with the nonstationary nature of the system during route-to-chaos. Additional adaptive filters are placed to adjust the input signal, compensate the emerging frequency during bifurcation and track the reference signal. As such, the proposed control scheme is able to regulate a chaotic system in both the time- and frequency-domain simultaneously. The architecture of the proposed controller adopts the active noise control algorithm (Filtered-x Least Mean Square) that uses one auto-adjustable Finite Impulse Response (FIR) filter to identify the system and another auto-adjustable FIR filter to eliminate the uncontrollable input. Analysis/synthesis wavelet filter banks are also incorporated. Analysis filter banks are used to decompose both input and reference signals before entering the controller and synthesis filter banks to combine the control input. By projecting input signal onto orthogonal subspaces spanned by the wavelet filter banks, the convergence performance of the least mean square algorithm is improved. In addition, the signal is resolved by DWT into components at various scales corresponding to successive octave frequencies, and moving wavelet filters are applied to extract temporal contents of the signal. The

Daubechies orthogonal D4 wavelet is employed in the study to control the period-doubling bifurcation generated by two types of Duffing oscillators. As Daubechies wavelet functions of higher order do not provide improved time and frequency resolutions or better performance of control for the particular Duffing oscillators, the D4 wavelet is chosen for its short filter length [71]. The control law incorporating the D4 wavelet is inherently constructed in the simultaneous time-frequency space.

A double-well Duffing oscillator with nonstationary external excitation is investigated using the following system parameters: $\mu = 0.4$, $\beta = 1$, $\alpha = -0.8$, $a = 0.32$, $b = 3\times10^{-5}$ and $\omega = 0.78$.

$$\ddot{x} + \mu\dot{x} + \beta x + \alpha x^3 = (a + bt)cos\,(\omega t) \tag{3.17}$$

The Duffing oscillator is selected for demonstrating the proposed control methodology for the reason that it exhibits period-doubling bifurcation undergoing route-to-chaos - a property shared by a broad set of nonlinear systems. An example of a periodically forced oscillator with a nonlinear elasticity, Duffing is among the most widely investigated equations. Time-frequency control of the Duffing oscillator, as established and reported in the followings, provides an alternative to all the control methodologies ever documented and available in the literature.

The time response and bifurcation diagram given in Figs. 3.7(a) and 3.7(b) show that the motion is initially periodic. When the excitation amplitude is increased in time, the motion becomes a period-doubling bifurcation. When multiple periods show up, the system becomes chaotic. Bifurcation becomes prominent at this stage with an increasing but bounded frequency bandwidth. When the excitation amplitude exceeds 0.42, the response becomes unbounded. The IF in Fig. 3.7(c) shows a dominant frequency oscillating between 0.1 and 0.15Hz, a second frequency between 0.05 and 0.1Hz, and a third frequency at around 0.03Hz. They all display temporal-modal behaviors and singularities signified by spectra of infinite bandwidth. The period-doubling bifurcation initiates at t = 2700s when the dominant frequency loses its characteristics and a second component shows up with a frequency half of the dominant one. With increasing excitation amplitude, the system undergoes route-to-chaos, in which all the frequencies are seen to engage in different patterns of temporal-modal oscillations indicative of dynamic deterioration. At t=3300s this state of instability reaches a point that renders the system no longer bounded. This phenomenon is analogous to many real-world complex nonlinear systems including the capsizing of a ship.

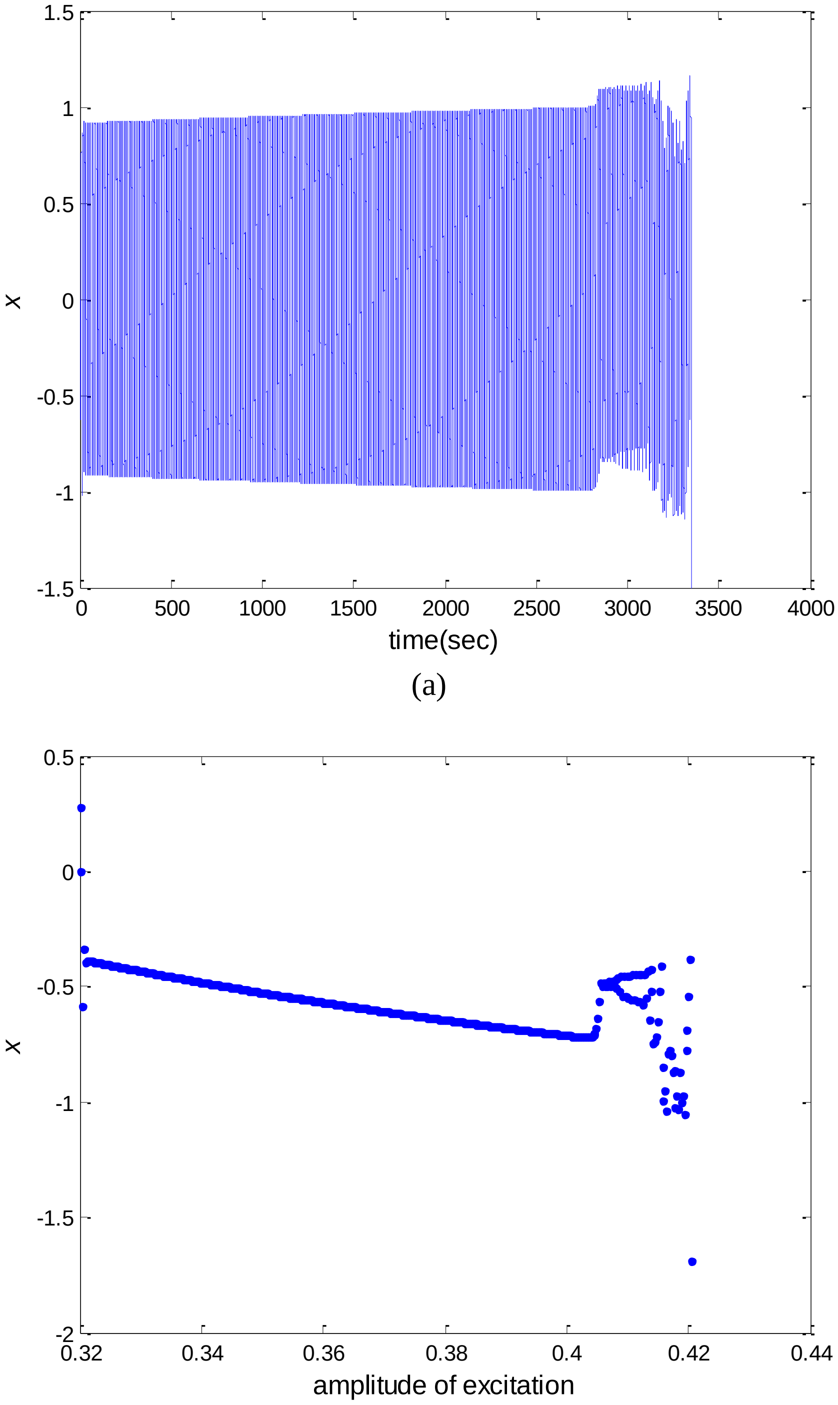

(a)

(b)

Fig. 3.7 (a) Time response, (b) bifurcation diagram, and (c) instantaneous frequency of the Duffing oscillator with nonstationary external excitation

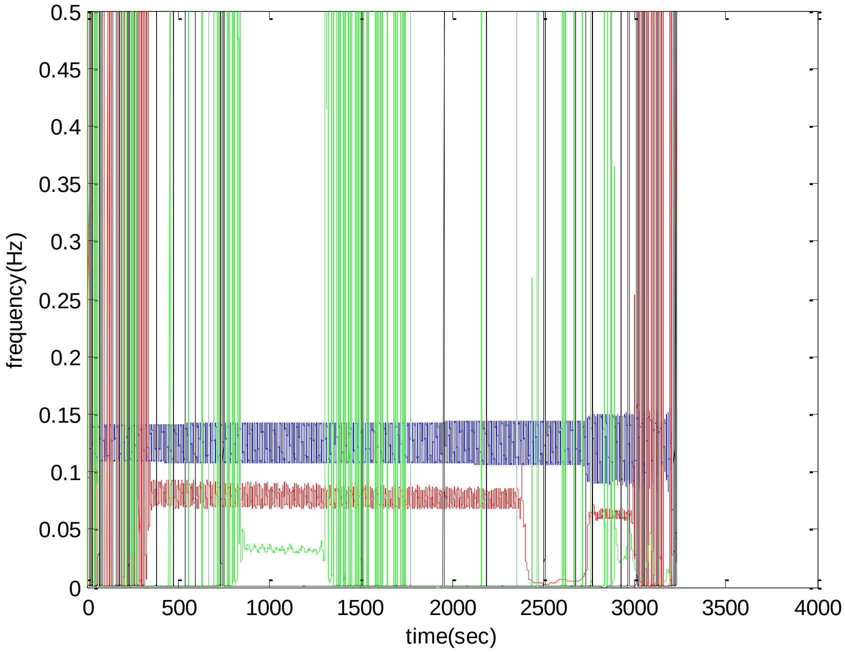

(c)

Fig. 3.7 Continued

To demonstrate the performance of the proposed controller in controlling route-to-chaos, two scenarios are considered against the baseline case in Fig. 3.7. First, the controller is turned on at the beginning of the bifurcation when the corresponding spectrum is still narrowband with a finite number of temporal-modal oscillations. Second, the controller is activated in the midst of chaos when the corresponding spectrum is already broadband. The result of the first scenario is shown in Fig. 3.8. Fig. 3.8(a) gives the time response of the controlled signal. The controller is turned on at t = 3000s, and the amplitude of the response is fast contained, thus a contrast to Fig. 3.7(a) when no controller is applied to negate the state of route-to-chaos. The desired signal for the controller is designed by using a stationary external excitation as the input to the linearized Duffing oscillator. The error between the output and the desired signal is shown in Fig. 3.8(b). The error before the onset of the controller is trivial and remains zero. The time domain error is bounded within a small range after the controller is turned on. Fig. 3.9(a) and 3.9(b) give the bifurcation diagram and instantaneous frequency, respectively, of the controlled response. Fig. 3.9(a) indicates that when the excitation amplitude is small the response is of a single, slow-changing frequency. The controller is activated when period-doubling bifurcation just initiates. After a short period of transient the bifurcation diagram shows a rapid restoration of dynamic stability. The instantaneous frequency in Fig. 3.9(b) shows that, after the transient response is stabilized, the characteristic of the dominant frequency is restored back to its status before bifurcation. At the same time the singularities of infinite bandwidth are eliminated and all frequencies are now of a well-defined temporal-modal structure. Figs. 3.8 and 3.9 together demonstrate that the proposed controller is able to mitigate a bifurcating system from deteriorating further in both the time- and frequency-domain. The second scenario, in which the controller is turned on at the state of chaos, is presented in Fig. 3.10. Fig. 3.10(a) is similar to but different from Fig. 3.8(a) in that the onset of the controller is postponed until t = 3200s when the system is in the state of chaos and on the verge of sudden divergence as seen in Fig. 3.7. The time response after the controller is engaged displays a steady amplitude. The response error in Fig. 3.10(b) is bounded within a small range after a short period of transient.

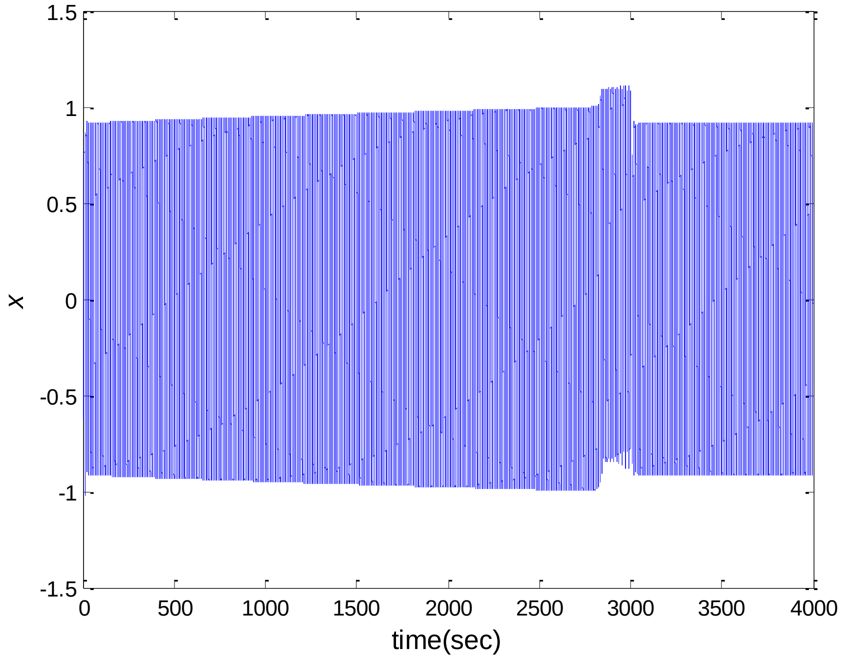

(a)

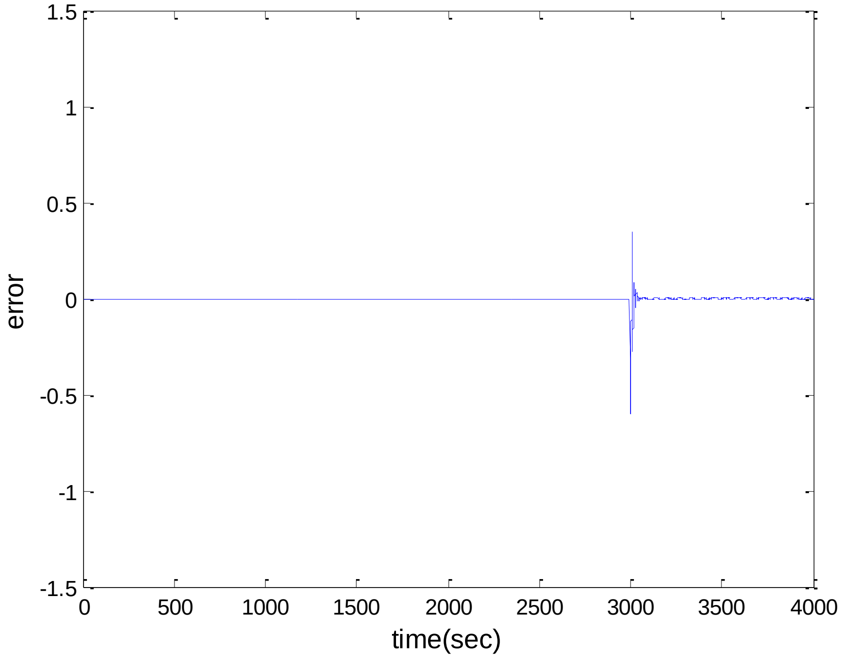

(b)

Fig. 3.8 (a) Time response (b) error response when the controller is turned on at the initial state of period-doubling bifurcation

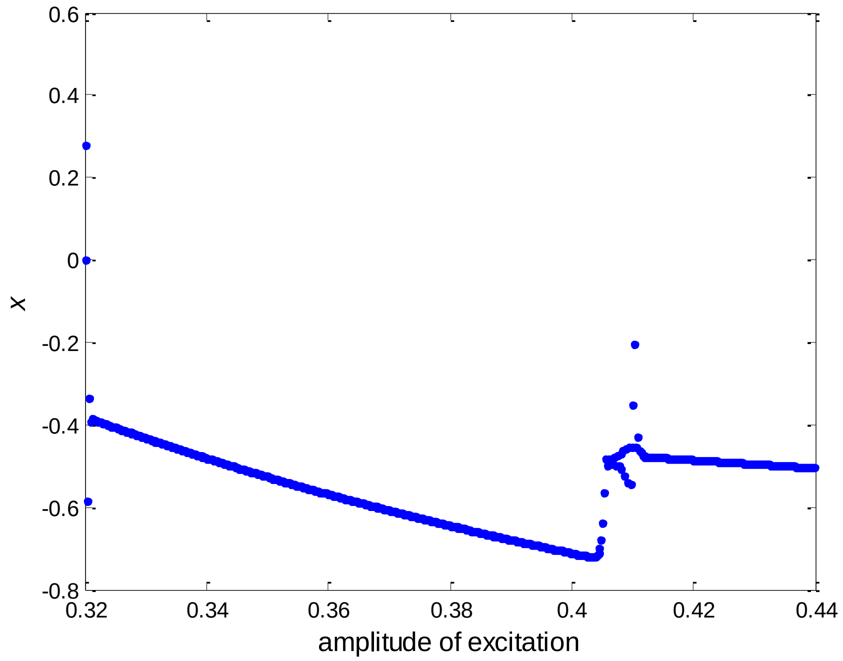

(a)

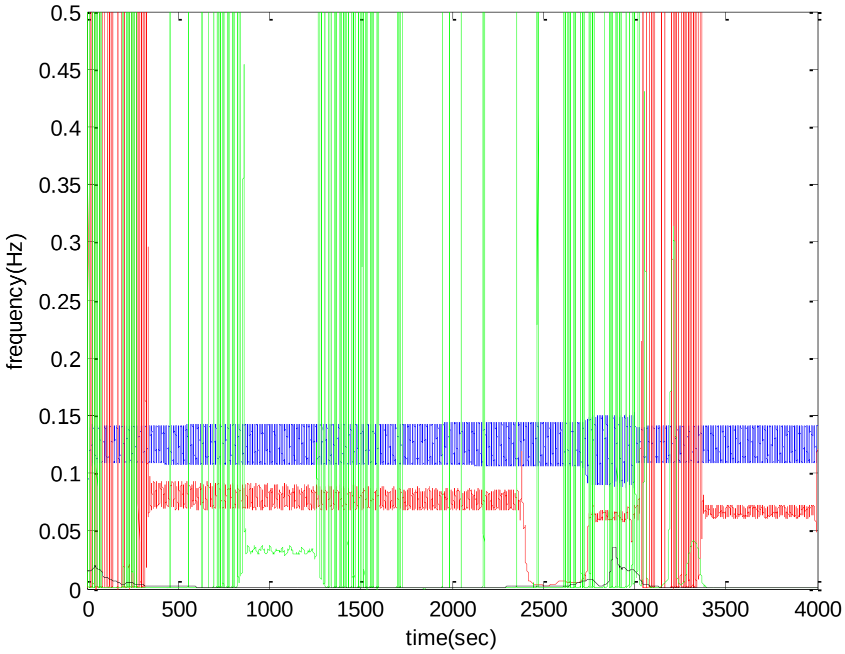

(b)

Fig. 3.9 (a) Bifurcation diagram (b) instantaneous frequency when the controller is turned on at the initial state of period-doubling bifurcation

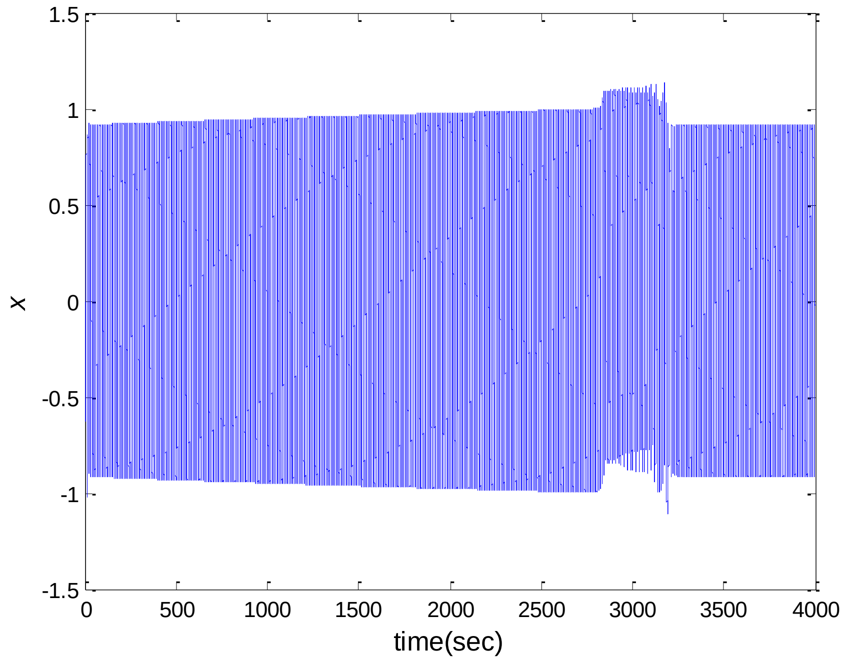

(a)

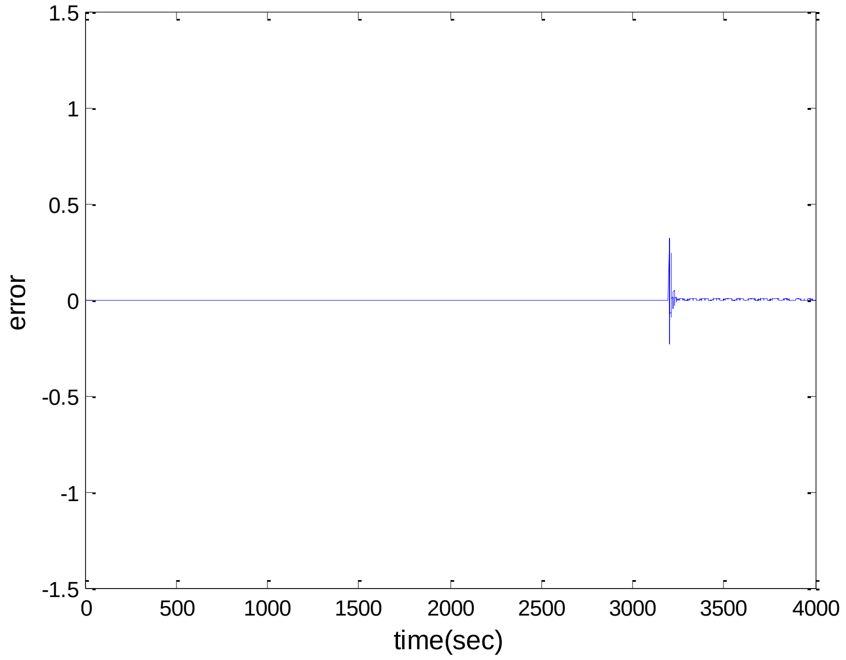

(b)

Fig. 3.10 (a) Time response and (b) response error when the controller is turned on at state of chaos

The bifurcation diagram and instantaneous frequency of the controlled response in Fig. 3.11 corroborate the same observation that the controller is both effective and robust. The bifurcation in Fig. 3.11(a) is a state of plethora of periods and indistinguishable trajectories, and also of an increasing but finite spectrum. The proposed controller is activated at this particular moment and state of dynamic instability. After a brief transient, the trajectory in the bifurcation diagram is stabilized and becomes a well-behaving line indicative of a state of single frequency. The corresponding IF is shown in Fig. 3.11(b), where multiple modes of frequencies coexist and temporal-modal aberration abounds. Upon controller turn-on at t = 3200s, the mode that the dominant frequency was in before bifurcation is seen restored and superfluous frequencies eliminated. Figs. 3.10 and 3.11 together conclude that the controller is able to negate dynamic instability and mitigate in both the time- and frequency-domain for chaos control.

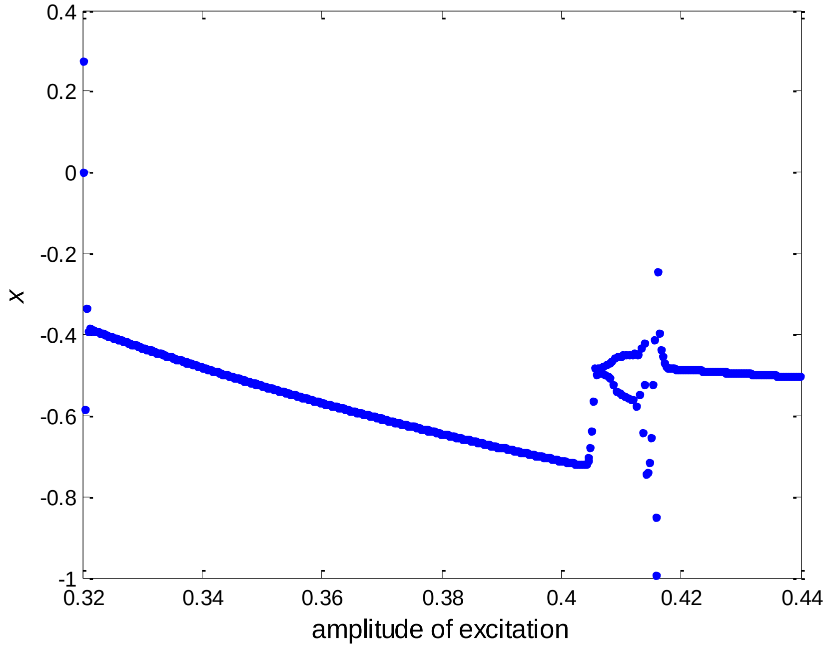

(a)

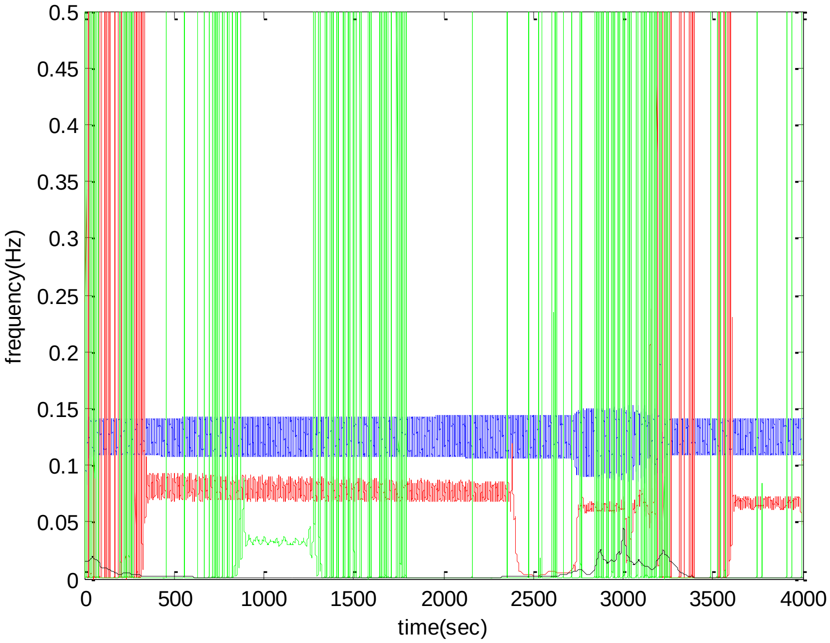

(b)

Fig. 3.11 (a) Bifurcation diagram and (b) instantaneous frequency when the controller is turned on at state of chaos

3.4 Summary

While most chaos control theories focus on controlling “static chaos,” the route-to-chaos is in fact “dynamic,” a transient, non-stationary process. A chaotic response is naturally bounded in the time-domain while in the mean time becoming unstably broadband in the frequency-domain. All control theories reviewed, either designed in the time-domain or frequency-domain, were insufficient to deal with the route-to-chaos process. *A priori* knowledge of the system must be available for them to work properly. They were shown to fail when the system state underwent severe changes. Hence it was necessary for the controller to be adaptive and able to identify the system and facilitate proper control in real-time. Two control theories, the OGY method and Lyapunov-based controller, were applied to stationary\nonstationary Hénon map and Duffing equation, respectively. It was shown that they were successful in controlling autonomous, stationary systems but failed when the systems were non-autonomous and nonstationary. Therefore a novel chaos control scheme was developed, having features that addressed the fundamental characteristics common of chaotic systems. Multiresolution analysis realized by filter banks that decomposed a signal into its high frequency and low frequency components was incorporated. Built in the wavelet domain, the presented controller was shown to render simultaneous manipulation in both the time and frequency domains. On-line identification and feedforward control were implemented via a revised version of the FXLMS algorithm. The proposed control scheme was able to suppress dynamical deterioration in both the time and frequency domains and properly regulated the response with the desired reference signal. The result implies that a chaos controller must be adaptive and developed in the joint time- frequency domain to be viable.

4. ON CONTROLLING MILLING INSTABILITY AND CHATTER AT HIGH SPEED*

4.1 Introduction

Milling is a machining operation whose high cutting efficiency is facilitated through the simple deployment of small tools of finite number of cutting edges at high spindle speed. When immersion rate is low and the time spent cutting is only a small fraction of the spindle period, interrupted cutting would ensure as a result. The regenerative effect could also be prominent, where the cutting force depends on the current as well as the delayed tool positions. In the stability analysis performed using a linear high speed milling model, Davies *et al* [72] showed that the fixed point of the model can lose its stability through either Neimar-Sacker bifurcation or period-doubling bifurcation. Szalai *et al* [73] further established that both bifurcations were subcritical using a nonlinear discrete model. They also demonstrated that a stable cutting can suddenly turn into chatter – a pronounced dynamic effect characterized by large tool vibration amplitude or frequency oscillation different from the spindle speed. Such a negative effect induces detrimental aperiodic errors such as waviness on the workpiece surface, inaccurate dimensions and excessive tool wear, among others [74].

---

*Part of this chapter is reprinted with permission from "On Controlling Milling Instability and Chatter at High Speed" by Liu, M. K. and Suh, C. S., 2012, Journal of Applied Nonlinear Dynamics, 1(1), pp. 59-72, Copyright 2012 by L&H Scientific Publishing

The onset of chatter has been investigated both analytically and numerically. Dynamic milling equations were transformed into linear maps and the eigenvalues of the transition matrix on the complex plane were used to predict stability [72,73]. Using numerical integration, stability was predicted by gradually increasing the axial depth-of-cut until instability occurred [74]. However, each method has its own shortcoming. Established methodologies use eigenvalues of the approximated transition matrix to determine the stability bound of the system. In route-to-chaos process, the way these eigenvalues leaves the unit circle on the complex plane is used to identify the type of bifurcation. But as long as the high order nonlinear terms are omitted and the solution is projected into orthogonal eigenvectors, the response is obscured and cannot be considered as a genuine representation of the nonlinear system. In numerical study, the stability of the system is decided by the emergence of additional frequencies in the corresponding Fourier spectrum. As a mathematical averaging scheme in the infinite integral sense, Fourier transform generates spectra that are misinterpreted and fictitious frequency components that are non-physical [31]. Thus, stability determined by Fourier spectrum would necessarily be erroneous. It has been demonstrated that to characterize route-to-chaos process, both time and frequency responses need be considered [75]. The concept of instantaneous frequency (IF) [33] is adopted in this section to help manifest the dependency of frequency on time – an attribute common of all nonlinear responses including milling chatter.

In general, contemporary control theories are developed either in the frequency domain or time domain alone. When a controller is designed in the frequency domain, the equation of motion is converted into a transfer function. Frequency response design methods, such as Bode plot and root locus, can be used to help developed frequency domain based controllers [76]. When a controller is designed in the time domain, the differential equations of the system are described as a state space model by state variables. Once controllability and observability are established, time domain control laws can then be applied. Controllers of either construct can only be applied exclusively either in the frequency or time domain, and they have been shown to be suitable for linear, stationary systems. However, for a nonlinear, nonstationary system, when undergoing bifurcation to eventual chaos, its time response is no longer periodic and broadband frequency spectrum emerges. Controllers designed in the time domain confine the time error while unable to suppress the expanding spectrum. On the other hand, controllers designed in the frequency domain constrain the frequency bandwidth while losing control over time domain error. Neither frequency domain nor time domain based controllers are sufficient to deal with bifurcation and chaotic response. This is also ascertained by the Uncertainty Principle, which states that time and frequency resolutions cannot be simultaneously achieved.

In sections that follow, a high-speed, low immersion milling model is explored without linearization so as to retain the inherent physical attributes of the nonlinear system. Because neither linearization nor eigenvectors are attempted, tools commonly adopted for identifying various types of bifurcations are no longer applicable. As an alternative, instantaneous frequency is deployed to characterize the route-to-chaos process in the simultaneous time-frequency domain. The novel wavelet-based active controller first introduced in Ref. [75] along with its fundamental features that enable simultaneous time-frequency control is also utilized. The wavelet-based active controller owes its inspiration to active noise control [57], though of a different objective. While active noise controls serve to minimize acoustic noise, the wavelet-based active controller is configured to mitigate the deterioration of the aperiodic response in both time and frequency domains when the system undergoes dynamic instability including bifurcation to chaos. The most prominent property of the controller is its applicability to nonlinear systems whose responses are non-autonomous and non-stationary. Such a powerful attribute is made possible by incorporating adaptive filters, so that system identification can be executed in real-time and control law can be timely modified according to the changing circumstances. Components of the wavelet-based active controller, including discrete wavelet transform (DWT) in the time domain, wavelet-based finite impulse response (FIR) filter, and filtered-x least mean square (FXLMS) algorithm, will be considered later in the presentation.

4.2 High Speed Low Immersion Milling Model

The one-degree-of-freedom milling model found in Ref. [73] that governs the tool motion of the cutting operation at high speed is adopted, as shown in Fig. 4.1. The tool has even number of edges and operates at a constant angular velocity, Ω. Its mass, damping coefficient and spring coefficient are denoted as m, c, and k, respectively. The feed rate is provided by the workpiece velocity V_0. The dynamic equation of milling motion that corresponds to Fig. 4.1(b) is

$$\ddot{x}(t) + 2\xi\omega_n\dot{x}(t) + \omega_n^2 x(t) = \frac{d(t)}{m} F_c(h(t)) \tag{4.1}$$

where x(t) is the tool tip vertical position, $\omega_n = \sqrt{c/m}$ is the undamped natural frequency, and $\xi = c/(2m\omega_n)$ is the relative damping factor.

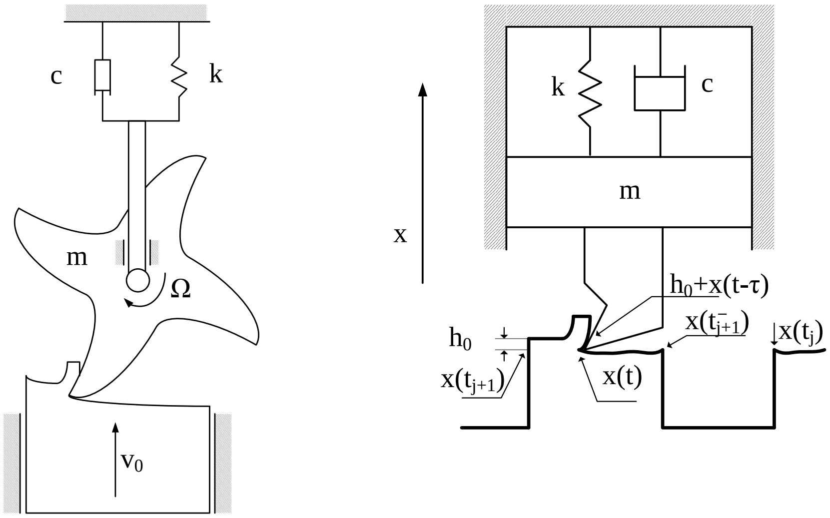

(a) (b)

Fig. 4.1 (a) Configuration and (b) mechanical model of high speed milling [73]

F_c , the nonlinear cutting force, is derived from the empirical three-quarter rule [73] as a function of the workpiece thickness, h(t),

$$F_c(h(t)) = Kw[h(t)]^{3/4} \tag{4.2}$$

where K is an empirical parameter and w is chip width. h(t) equals the feed per cutting period h_0 plus the previous tool tip position, x(t-τ), and minus the current tool tip position, x(t),

$$h(t) = h_0 + x(t-\tau) - x(t) \tag{4.3}$$

with d(t) being a delta function defined as

$$d(t) = \begin{cases} 0 & if \quad \exists j \in \mathbb{Z}: \quad t_j \le t < t_{j+1}^- \\ 1 & if \quad \exists j \in \mathbb{Z}: \quad t_{j+1}^- \le t < t_{j+1} \end{cases} \tag{4.4}$$

The cutting force is applied to the system only when the tool edge physically engages the workpiece ($t_{j+1}^- \le t < t_{j+1}$). After the tool edge disengages the workpiece, the tool starts free vibration until the next edge arrives ($t_j \le t < t_{j+1}^-$). As is noted in [73], the time spent on cutting is relatively small compared to the time spent on free vibration.

4.3 Route-to-Chaos and Milling Instability

Following Ref. [72], the mass of the tool *m* is 0.0431kg, stiffness coefficient *k* is 1.4 MN/m and damping coefficient *c* is 8.2 Ns/m. Time delay τ is defined by considering the number of cutting edges deployed (N) and the spindle speed (Ω) as $\tau = \frac{2\pi}{N\Omega}$, where *N* = 2 in the study. In investigating the route-to-chaos displayed by Eq. (4.1), the axial depth-of-cut (ADOC) is kept at 1.0 mm while the spindle speed is stepped down from 15,000rpm to 12,000rpm. Fig. 4.2(a) shows the milling response at 15,000 rpm. It is a stable cutting condition having a time response that oscillates with an amplitude smaller than 0.1mm. Its Fourier spectrum in Fig. 4.2(b), however, is one of relatively broad bandwidth having multiple high frequency components, thus indicating dynamic instability. With a major frequency oscillating between 1000Hz and 1300Hz and a second frequency oscillating about 500Hz, the instantaneous frequency in Fig. 4.2(c) further asserts that the motion as a period-doubling bifurcation. As oppose to the Fourier spectrum in Fig. 4.2(b), the corresponding marginal spectrum in Fig. 4.2(d) shows that the bandwidth is confined and narrow, thus signifying the response as dynamically stable. With the decrease of the spindle speed, the milling response undergoes a route-to-chaos process.

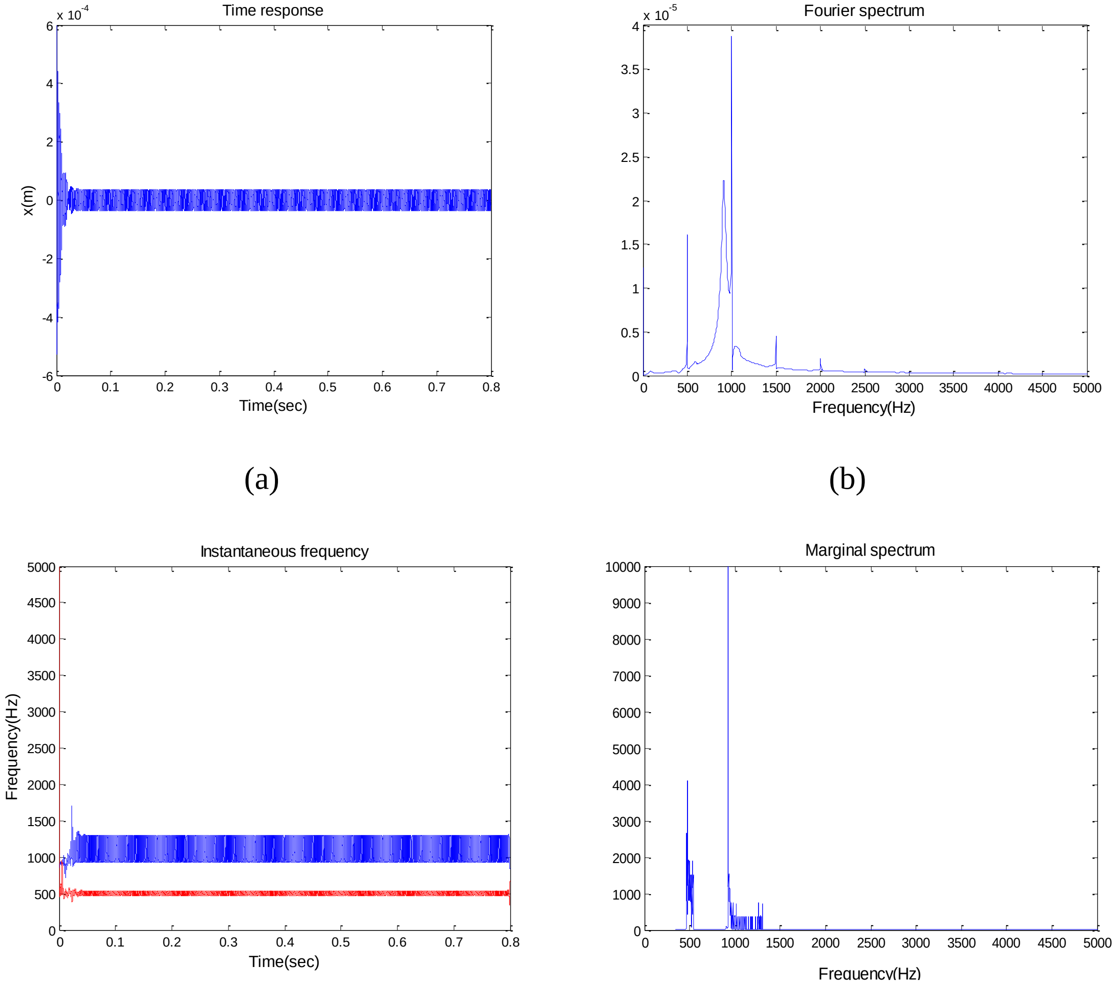

(a) (b)

(c) (d)

Fig. 4.2 (a) Time response (b) Fourier Spectrum (c) Instantaneous frequency (d) marginal spectrum when Ω = 15000 rpm and ADOC = 1.0mm (stable cutting condition)

When the spindle speed is at 14,000 rpm, new frequencies that are ½ and ¼ of the 500Hz component are registered in Figs. 4.3(c) and 4.3(d), meaning that the response is bifurcating towards chaos. This 4T period-doubling bifurcation state of instability is not resolved in the Fourier spectrum in Fig. 4.3(b). Fig. 4.3(b) literally misinterprets the response as one that is not experiencing bifurcation. When the spindle speed is further reduced to 13000rpm, the Fourier spectrum in Fig. 4.4(b) remains almost unchanged from the previous one with an unmistakably lower time response amplitude. The corresponding instantaneous frequency and marginal spectrum in Figs. 4.4(c) and 4.4(d), however, depict a scenario in which the system response is engaging in a state of very different temporal-spectral structure. With the expanding frequency bandwidth, the system is on the verge to becoming chaotic.

The Fourier spectrum in Fig. 4.5(b) that corresponds to a lower spindle speed at 12000rpm is neither intuitively nor physically correct. The instantaneous frequency in Fig. 4.5(c) shows that the major frequency oscillates between 1000Hz and 3000Hz, a character of a chaotic motion. This is further confirmed by the marginal spectrum in Fig. 4.5(d) where a plethora of frequency components constitute a broadband spectrum. The lesson learned from Figs. 4.2-4.5 is that, while Fourier spectrum misinterprets the state of the response, instantaneous frequency along with the marginal spectrum is preferred for resolving route-to-chaos process and deterioration of stability.

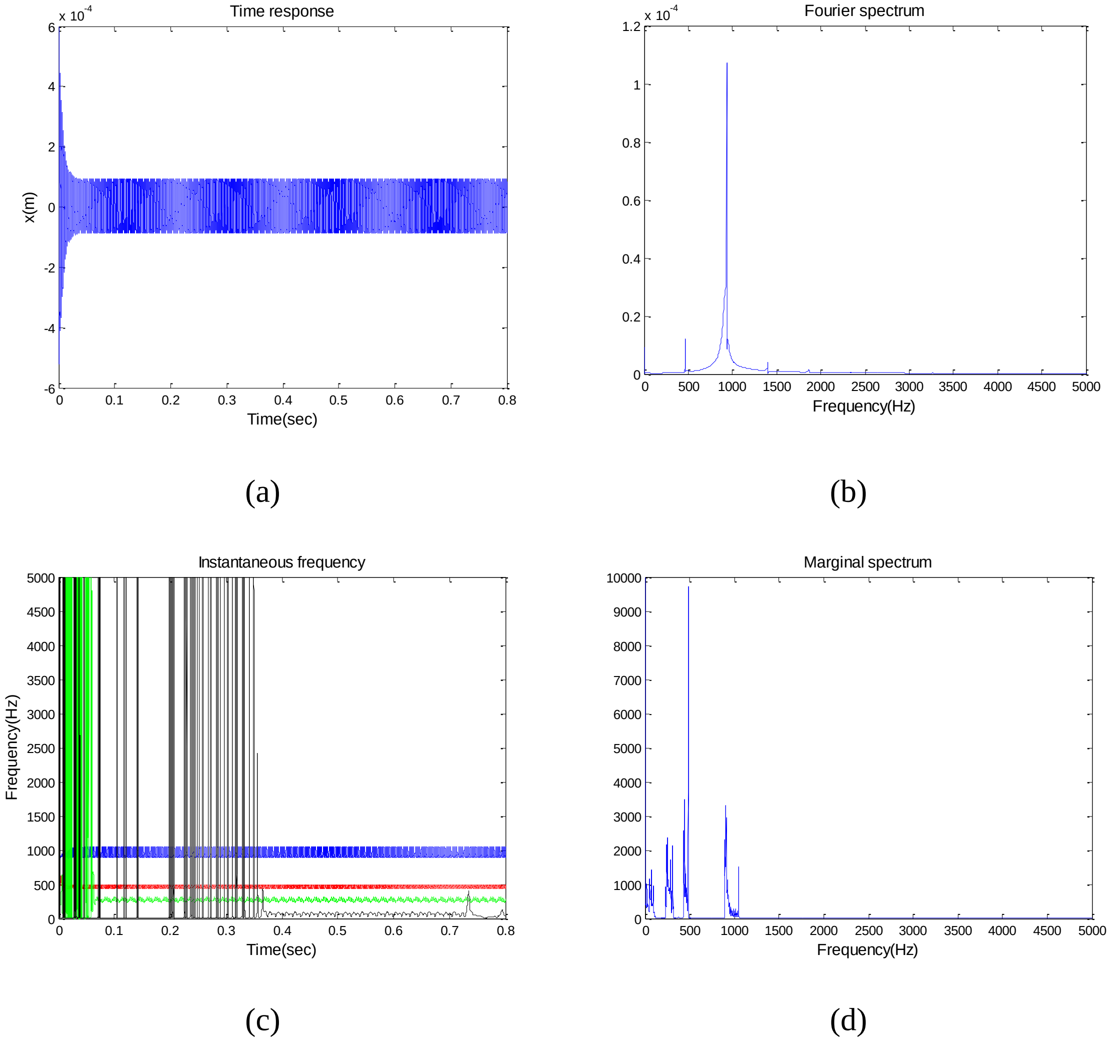

Fig. 4.3 (a) Time response (b) Fourier Spectrum (c) Instantaneous frequency (d) marginal spectrum when Ω = 14000 rpm and ADOC = 1.0mm (4T period-doubling bifurcation)

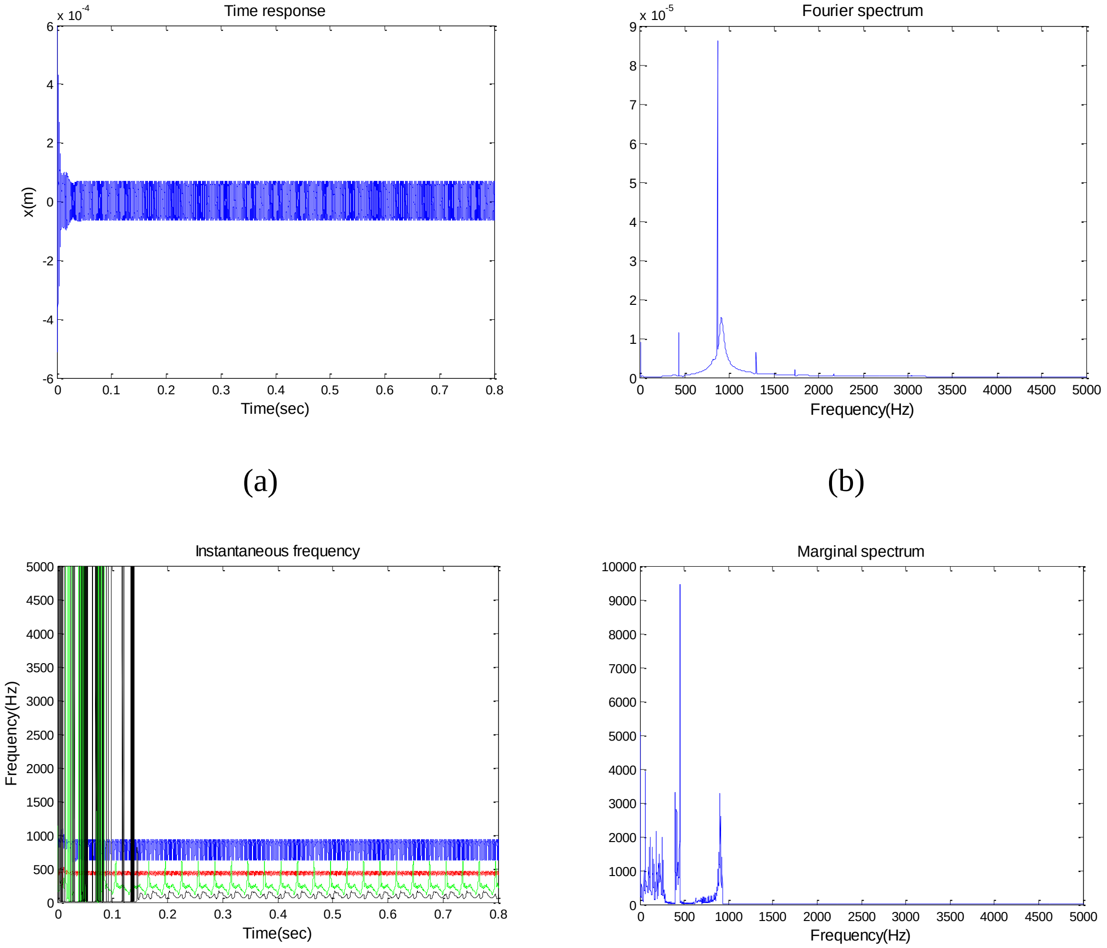

(a) (b)

(c) (d)

Fig. 4.4 (a) Time response (b) Fourier Spectrum (c) Instantaneous frequency (d) marginal spectrum when Ω = 13000 rpm and ADOC = 1.0mm (unstable cutting condition)

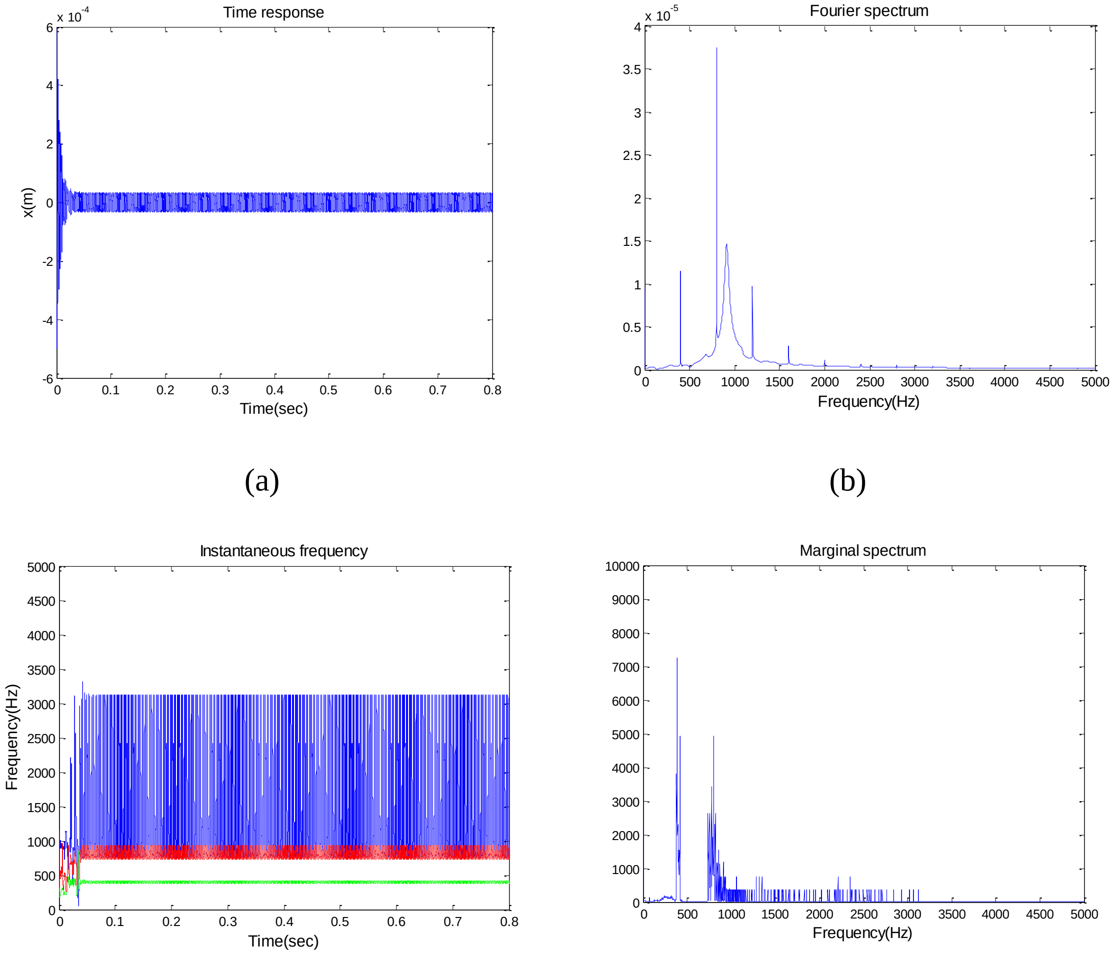

(a) (b)

(c) (d)

Fig. 4.5 (a) Time response (b) Fourier Spectrum (c) Instantaneous frequency (d) marginal spectrum when Ω = 12000 rpm and ADOC = 1.0mm (chaotic motion)

4.4 Numerical Experiment

When milling at high speed, the corresponding time response would become aperiodic and the frequency response would deviate away from well-defined harmonics and become unstably broadband. Such responses are highly nonlinear and could lead to tool chatter if unattended. In this section the milling model in Eq. (4.1) is again investigated in response to a 50,000 rpm spindle speed and 2 different ADOCs at 0.003m and 0.001m. Given that Fourier spectra were shown to obscure the genuine characteristics of all the responses considered in the previous sections, instantaneous frequency and marginal spectrum are adopted instead. The orthogonal Daubechies D4 wavelet is once again selected as the mother wavelet in the wavelet-based active controller. The filter length of the identifying filter and the controlling filter are both 256. At ADOC = 0.003m the wavelet-based controller is turned on at t = 0.2s to align the response with zero, the target trajectory. When $t \leq 0.2$s, the vibration amplitude in Fig. 4.6(a) is aberrational. There are four distinct frequencies in the instantaneous frequency in Fig. 4.6(c), each oscillating with the temporal-modal structure typical of a highly bifurcated response. Before controller is applied, the marginal spectrum in Fig. 4.6(b) sees a spectrum with frequencies ranging from 0 to 1500 Hz. When the controller is online at t = 0.2s, the time response is greatly reduced and the frequency response is a well-behaved temporal-modal narrowband structure confined between 1400Hz and 2200Hz. As a further verification, the phase plots for the before and after scenarios are compared in Fig. 4.7. The response is seen in the state space to reduce to a manifold after the controller is applied, thus explaining the restraining of bandwidth and frequencies. It can be concluded from the fact that these two phase plots belong to different basins and have fundamentally different geometric structures that the controller alters the underlying signature of the system, effectively negates further deterioration, and ensures dynamic stability at 50,000 rpm.

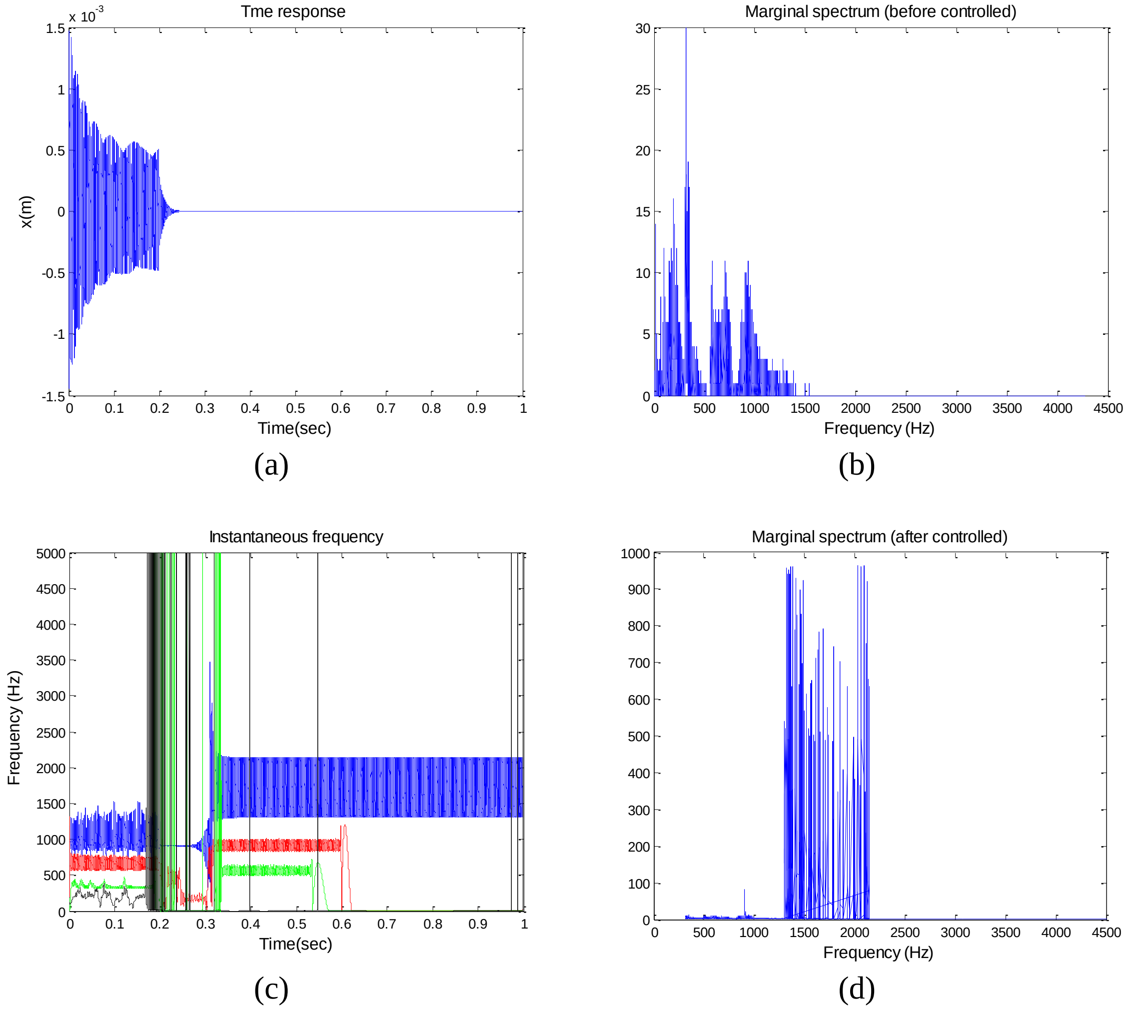

(a) (b)

(c) (d)

Fig. 4.6 (a) Time response (b) marginal spectrum (before controlled) (c) instantaneous frequency (d) marginal spectrum (after controlled) when controller applied at t = 0.2s with Ω = 50,000 rpm and ADOC = 0.003m

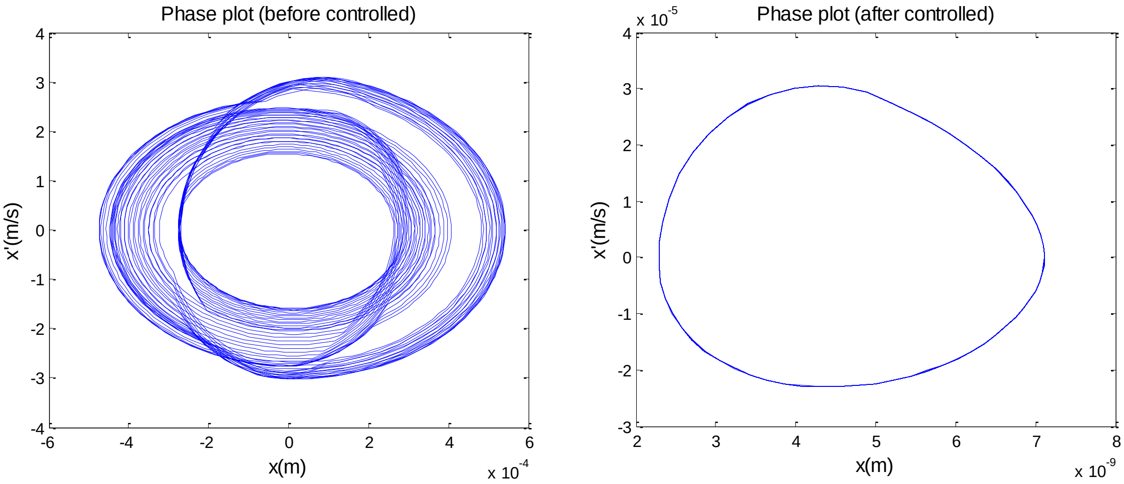

(a) (b)

Fig. 4.7 Phase plots of (a) uncontrolled and (b) controlled responses

The next case studied is with a smaller milling ADOC set at 0.001m. Because the amplitude of the time response remains small, the motion as seen in Fig. 4.8 seems suggest a stable cutting operation. However the instantaneous frequency shows that there are prominent temporal-modal oscillations, indicative of a complex nonlinearity that is the precursor of tool chatter. After controller is turned on at t = 0.2s, both the time response and marginal spectrum are effectively restrained. The phase plots of the controlled and uncontrolled responses are placed next to each other for comparison in Fig. 4.9. The 2 manifolds are indications that the motions, both before and after the controller is activated, are stable. However, while it remains in the same basin after the controller is on, the scale and magnitude of the trajectory are significantly reduced by a factor of 100 in Fig. 4.9(b).

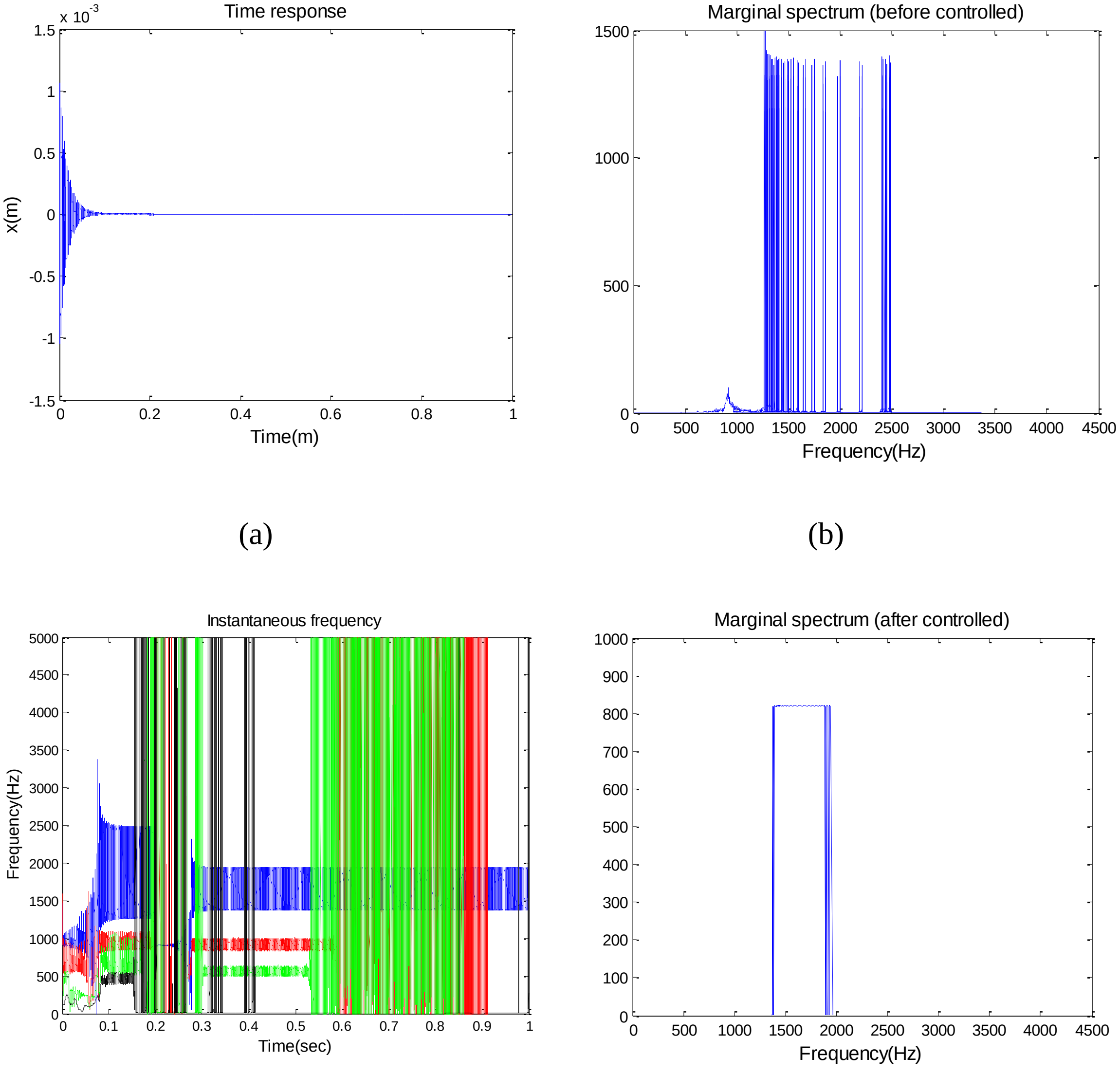

(a) (b)

(c) (d)

Fig. 4.8 (a) Time response (b) marginal spectrum (before controlled) (c) instantaneous frequency (d) marginal spectrum (after controlled) when controller applied at t = 0.2s with Ω = 50,000 rpm and ADOC = 0.001m

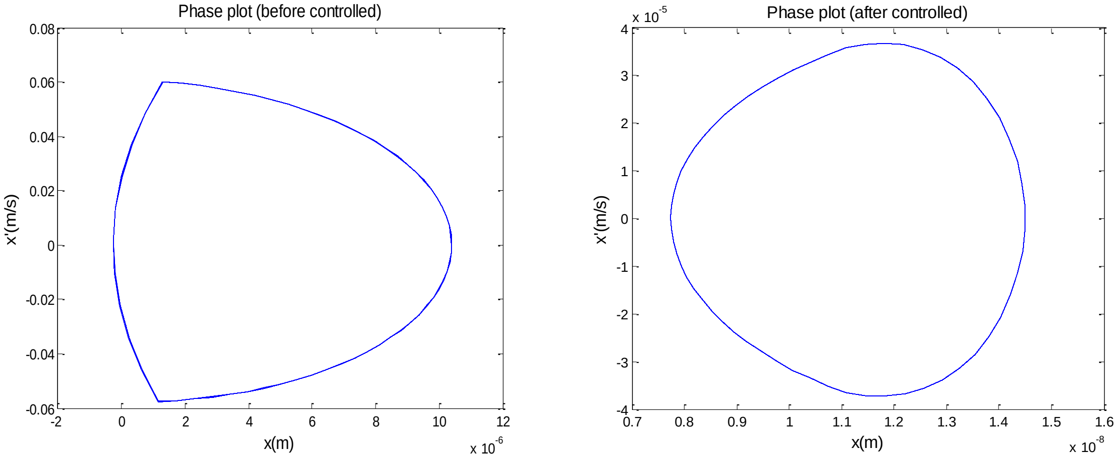

(a) (b)

Fig. 4.9 Phase plots of (a) uncontrolled and (b) controlled responses

A few observations can be made with regard to the figures above. First the wavelet-based active controller not only reduces the aberrational vibrations in the time domain. It also simultaneously regulates the frequency response in the frequency domain. Thus the nonlinearity of the response is mitigated from further deterioration. Second, the motion of the milling tool transforms dramatically after the controller is applied, as a low-amplitude oscillation in the time domain that manifests a reduction manifold in the state space. Even though the control target is set to zero and the time domain error achieved is satisfactorily small, however, the spectral response does not contain just one single frequency. The frequency spectrum still varies, but is now strictly confined within a limited bandwidth.

4.5 Summary

Milling tool dynamics was shown using instantaneous frequency, in lieu of Fourier spectra, to be transient and nonlinear due to the regenerative effect. Milling response was seen to be highly sensitive to machining condition and external perturbation, easily deteriorating from bifurcation to chaos. When losing stability, milling time response was no longer periodic and the frequency response became broadband, rendering tool chatter and probable tool damage. The marginal spectrum derived from instantaneous frequency was considered to be more suitable than Fourier spectrum to define the stability boundary for high speed milling operation. For the route-to-chaos process in which both time and frequency responses deteriorate at the same time, it is necessary to control them simultaneously. The wavelet-based active controller having DWT, wavelet-based adaptive FIR filter, and FXLMS algorithm as its physical features was demonstrated to successfully negate bifurcations and chaotic responses by adjusting the input. Integration of DWT in the controller effectively manipulated the wavelet coefficients, hence facilitating the control of milling tool response in both the time and frequency domains simultaneously. The concept adopted from the FXLMS algorithm enabled the identification and control of the system in *real-time*. Unlike conventional control law design approach that always requires the system to be controlled be mathematically explicit, the construction of the wavelet-based controller has no such a requirement. Since no mathematical linearization is needed, the inherent characteristics of the system to be controlled are faithfully retained and its underlying dynamics can be resolved without distortion. The several cases of milling instability investigated using the wavelet-based active controller together indicate that to properly control a nonlinear system whose responses are transient and nonstationary, it is necessary for the control law to have certain properties including being able to identify the system in real-time and apply mitigation in both the time and frequency domain simultaneously.

5. MULTI-DIMENSIONAL TIME-FREQUENCY CONTROL OF MICRO-MILLING INSTABILITY*

5.1 Introduction

Essential to producing complex three-dimensional products out of a wide range of materials, micro-milling is critical to the advancement of technology for many industries as components are continuously being reduced in size and require increased functionality. However, micro-milling is subject to unpredictable tool life and premature tool failure which can ruin a workpiece and instigate costly and inefficient product inspection and resetting [77, 78]. Thus it would be of direct impact to improve the efficiency of the process. Chip clogging, fatigue, and excessive stress related failure are identified as the three common micro-mill breakage mechanisms [77]. When the stress is below the endurance limit but above the normal operation level the tool will not fail immediately [77]. However, the stress on the shaft will change repeatedly while the tool is rotating causing the strain distribution to change repeatedly at the tool shaft, thus inducing fatigue. Vibrations with high or multiple frequency components increase the speed at which the strain distribution changes, inevitably resulting in fatigue failure occurring at an accelerated rate. The excessive stress related breakage occurs when there

---

*Part of this chapter is reprinted with permission from “Multi-Dimensional Time-Frequency Control of Micro-Milling Instability” by Liu, M. K., Halfmann, E. B., and Suh, C. S., 2012, Journal of Vibration and Control, Manuscript ID: JVC-12-0264, Copyright 2012 by SAGE Publications Ltd.

is a sudden increase in the cutting forces indicative of dynamically unstable cutting due to excessive vibration magnitudes. Also, excessive machining vibrations (chatter) affect the workpiece surface finish and tolerances, and result in larger cutting forces which are key indicators of tool performance [79]. Thus, micro-milling performance and failure are directly affected by the dynamic response of the tool, rendering controlling dynamic instability fundamental to improving micro-milling efficiency.

Physical models are important for the characterization of dynamic instability, development and testing of control algorithms, and providing insight needed to designing empirical research. Micro-milling cannot directly adopt the methods used for modeling macro-milling due to different cutting force mechanisms at work such as the increased impact of material plowing. When the chip thickness is too small a chip will not form and the material will be plowed under the tool [80]. This phenomenon is more prominent in micro-milling due to the increased feed-rate to tool nose radius ratio. Micro-milling is a highly nonlinear process due to these additional nonlinear characteristics and the high spindle speeds which are commonly employed. To address the issue of micro-milling chatter an uncut chip thickness model is coupled with a finite element orthogonal cutting model in [81]. Stability lobes are generated using statistical variances and chatter is defined as a statistical variance larger than 1 μm. However, the uncut chip thickness model reported in [81] fails to consider the elastic recovery of the material due to the plowing mechanism, thus hindering its veracity. Micro-milling stability lobes are produced in [82, 83] but the stability lobes have limited accuracy when compared with the experimental data, and it is shown that the dynamic properties of the system have a substantial impact on the resulting stability. These stability lobes are generated through linearization which obscures the nonlinear characteristics of the process that are prominent in micro-milling. The experimental data in [82, 83] shows high frequency components and multiple chatter frequencies that are characteristics of a nonlinear process. The modeling and control analysis of the process should retain the inherent nonlinearities to effectively address dynamic instability. An effective method for modeling the nonlinear forcing mechanism of the micro-milling process is through slip-line field models. It is shown in [84] that the comprehensive slip-line field model developed in [85] outperforms the finite element model when predicting the magnitude of the cutting forces. A comprehensive slip-line model is developed in [86] for modeling the cutting process near the tool edge. Earlier slip-line models in [87, 88] predicted the shearing and plowing forces, and the force mechanism equations were improved upon in [89]. The research reviewed above focuses on the development of force mechanisms for predicting cutting forces and does not investigate dynamic instability. Ref. [90] adopts the slip-line field force mechanism presented in [89] and accounts for material elastic recovery in the chip thickness calculation, the effective rake angle, and the helical angle of the tool for numerically studying the dynamic response. This model captures all the prominent nonlinear characteristics of micro-milling and will be adopted in this investigation to explore nonlinear micro-milling control.

There are several challenges in controlling micro-machining. In addition to the distinct cutting dynamics which differentiates micro-machining from macro-machining, the performance of miniaturized end-mill is greatly affected by the vibrations and excessive force. The influence of noise and the inadequate bandwidth of force sensors due to high rotational speeds make it difficult to measure cutting forces [84]. Unlike macro-machining, impulse hammer tests for investigating tool tip dynamics are not practical in microstructure due to the fatigue nature of miniature tools, and the accelerometers cannot be effectively attached due to their size and weight, which influence the overall dynamics [91]. To estimate the microstructure tool dynamics, Receptance Coupling (RC) was implemented to mathematically couple the tool tip and the remainder of the tool using non-contact sensors [92]. However, the development of micro-machining controllers still suffers from the challenges of miniature microstructure. There are only a few research papers related to the control of micro-machining. Commend shaping method was followed to reduce the tracking error of the micro-mills in [93]. It properly chose the acceleration profile of the DC motors on the precision linear stage to counteract the vibration caused by the internal force from high speed motion of the tool. The contour error was reduced by cross-coupling, which established the real-time contour error model and returned error correction signal to the motor of each axis [94]. Piezoelectric stack actuators were mounted to directly control the relative motion between the tool-spindle and the workpiece of a micro-milling machine, and Active Vibration Control (AVC) was used to suppress the vibration of the tool tip point [95]. As the response time of piezoelectric actuators cannot catch up with the high rotating speed of the spindle, the method can only apply to low-speed micro-machining.

From the literature review, it is concluded that there are no effective solutions for controlling chatter in micro-machining. One crucial factor is to regulate the highly nonlinear cutting forces. The cutting forces cannot exceed the critical limit of the tool in which sudden tool failure would occur. This limits the chip load and thus the material removal rate that can be achieved. Higher spindle speeds are then desired to increase the material removal rates of the process without increasing the chip load. However, the nonlinearities of the force mechanism become more prominent at higher spindle speeds causing the increased excitation frequencies to result in dynamic instability. Another factor is that the control method has to adapt to the uncertainties of the cutting process as well as the changing dynamics. However, cutting instability in fact consists of the deterioration in both time and frequency domains due to the highly nonlinear nature of micro-milling process. A simultaneous time-frequency control scheme was developed to restrain the deterioration of time and frequency responses in the instability states of bifurcation and chaos [96]. It has been demonstrated to effectively deny milling chatter at high speed and restore milling stability as a limit cycle of extremely low tool vibrations [97]. The following sections together present a nonlinear micro-milling model that captures the intrinsic characteristics of the cutting process. Deriving from the simultaneous time-frequency controller design in [96], a multi-variable nonlinear control scheme is then developed to facilitate the proper mitigation of micro-milling instability.

5.2 Nonlinear Micro-Milling Model

The micro-milling model to be controlled is the one presented in [90] accounts for the prominent nonlinear characteristics of the process. The forcing mechanism for the model adopts the slip-line force model developed in [89] which expanded upon the model in [88] by accounting for the dead metal cap and adding an additional slip-line on the clearance face of the tool. The model in [90] neglects this additional slip-line assuming that, since the material takes time to recover and the feed rates used are larger than the tool nose radius, this additional slip-line will have negligible effect on the cutting forces. When the chip thickness is greater than the critical chip thickness, it is assumed that both shearing and plowing forces are present. The shearing and plowing forces in the cutting and thrust directions as given in [88 - 90] are provided in Eqs. (5.1) – (5.4),

$$dF_{sc} = \tau\, da[(\cos\varphi_S + a_\theta \sin\varphi_S)\, l_S + (\cos(2\eta_2)\sin\alpha_e + a_2\cos\alpha_e)\, l_b] \tag{5.1}$$

$$dF_{st} = \tau\, da[(a_\theta \cos\varphi_S - \sin\varphi_S)\, l_S + (\cos(2\eta_2)\cos\alpha_e - a_2\sin\alpha_e)\, l_b] \tag{5.2}$$

$$dF_{pc} = \tau\, da[\, (\cos(2\eta_1)\cos\psi + a_1\sin\psi)\, l_b] \tag{5.3}$$

$$dF_{pt} = \tau\, da[\, (a_1\cos\psi - \cos(2\eta_1)\sin\psi)\, l_b] \tag{5.4}$$

where, referring also to Fig. 5.1, τ is the material shear flow stress, da is the axially depth of cut, φ_s is the chip flow angle, α_e is the effective rake angle, and l_s, l_b, a_θ, a_1, a_2, η_1, η_2, and ψ are the slip-line field variables as defined in [89, 98]. The force equations and associated variables in Eqs. (5.1) – (5.4) are all functions of the instantaneous chip thickness, $tc(t)$. In micro-milling, when $tc(t)$ is less than the minimum chip thickness, $tc_{\min}$, then only plowing forces are present, and when the tool jumps out of the cut, there are no forces acting on the system. Thus, the three force cases considered in [90] are:

Case I: $tc(t) > tc_{\min}$ $\{ \begin{matrix} dF_t = dF_{st} + dF_{pt} \\ dF_c = dF_{sc} + dF_{pc} \end{matrix}$

Case II: $0 < tc(t) < tc_{\min}$ $\{ \begin{matrix} dF_t = dF_{pt} \\ dF_c = dF_{pc} \end{matrix}$

Case III: $tc(t) < 0$ $\{ \begin{matrix} dF_t = 0 \\ dF_c = 0 \end{matrix}$

These three cases indicate that accurately determining $tc(t)$ is important to faithfully realizing the forces acting on the system and thus the resulting dynamics. The model utilizes a method which accounts for the elastic recovery of the plowing phenomenon and the tool jumping out of the cut. Eqs. (5.5) – (5.7) are utilized for determining $tc(t)$ where subscript, j, refers to the tooth 1 and 2 of the micro-mill, fc is the feed rate, N is the number of teeth, Ω is the spindle speed, $\Delta x = x(t) - x(t-\delta)$, $\Delta y = y(t) - y(t-\delta)$, and time delay $\delta = {}^{60}\!/_{(N\Omega)}$.

$$tc_j(t-\delta) > tc_{\min}: \quad tc_j(t) = fc \cdot \sin\varphi_j(t) + \Delta x \sin\varphi_j(t) + \Delta y \cos\varphi_j(t) \tag{5.5}$$

$$0 < tc_j(t-\delta) < tc_{\min}: \quad tc_j(t) = fc \cdot \sin\varphi_j(t) + \Delta x \sin\varphi_j(t) + \Delta y \cos\varphi_j(t) + p_e \cdot tc_j(t-\delta) \tag{5.6}$$

$$tc_j(t-\delta) < 0: \quad tc_j(t) = fc \cdot \sin\varphi_j(t) + \Delta x \sin\varphi_j(t) + \Delta y \cos\varphi_j(t) + tc_j(t-\delta) \tag{5.7}$$

The model also accounts for the effective rake angle and the helical angle. The derivation for the helical angle results in the following equations of force components,

$$F_x = -F_t \sin\varphi_j(t) + F_c' \cos\varphi_j(t) \tag{5.8}$$

$$F_y = -F_t \cos\varphi_j(t) - F_c' \sin\varphi_j(t) \tag{5.9}$$

$$F_z = F_c \sin\theta_h \tag{5.10}$$

where θ_h is the helical angle and $F_c' = F_c \cos\theta_h$.

To account for the helical angle, it is also assumed that the tool can be broken up into axial elements. Thus, the immersion angle $\varphi_j(t)$ shown in Fig. 5.1 for each tooth and axial element must be determined to know if that tooth and axial element is engaged in the workpiece and thus contributing to the overall force of the system. The equation to find the immersion angle φ for each tooth, j, and axial element, k, is given in Eq. (5.11)

$$\varphi_{jk}(t) = [\varphi_{ij} - (\frac{da}{2} + k\,da)\frac{\tan\theta_h}{R} + \frac{2\pi\Omega t}{60}] \tag{5.11}$$

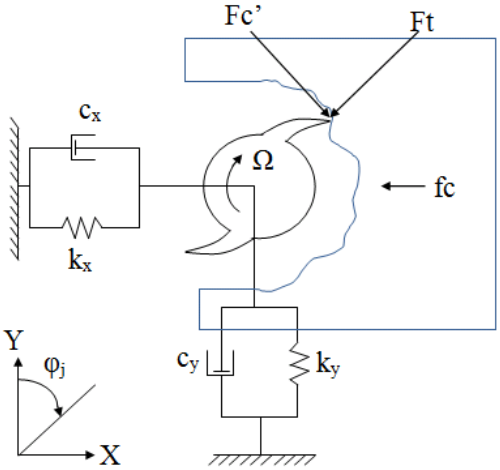

Fig. 5.1 The 2D lumped mass, spring, damper model of the micro-tool

It is assumed that the tool can be modeled as the lumped mass-spring-damper system seen in Fig. 5.1. It is also assumed that because of the very high stiffness in the Z-direction, tool vibrations along the spindle axis are negligible. This results in two coupled equations of motion governing the X- and Y-direction motions of the tool as follows

$$m\ddot{x} + c_x \dot{x} + k_x x = F_x(t, \Delta x, \Delta y) \tag{5.12}$$

$$m\ddot{y} + c_y \dot{y} + k_y y = F_y(t, \Delta x, \Delta y) \tag{5.13}$$

5.3 Multi-Variable Simultaneous Time-Frequency Control

The novel nonlinear control law presented in [96] was formulated to address the fundamental characteristics inherent of dynamic instability including bifurcation and chaos. Unlike modern control theories which focus on eliminating time domain errors, the control law restrains the deterioration of the time and frequency responses concurrently. The system response to be controlled is adjusted by Least Mean Square (LMS) adaptive filters to force the system to follow a target signal, which is the response of a stable state before dynamic deterioration. Because neither linearization nor closed-form solution is required, all the genuine features of the nonlinear response are retained. The control scheme manipulates the corresponding discrete wavelet transform (DWT) coefficients of the system response to realize control in the joint time-frequency domain. The control scheme has been demonstrated to successfully negate the rich set of bifurcated and chaotic responses of a time-delayed milling model in [97]. The control theory is applied to the multi-dimensional micro-milling model described in Eqs. (5.12) – (5.13). By following the multi-variable control architecture shown in Fig. 5.2, X- and

Y-direction motions are determined using the force components that are defined by the feed and the instantaneous chip thickness in Eqs. (5.5) – (5.7). To achieve multi-variable control, two independent nonlinear controllers are placed in front of the micro-milling model of each direction to mitigate the excitation force components. These two controllers operate in parallel and use different parameters.

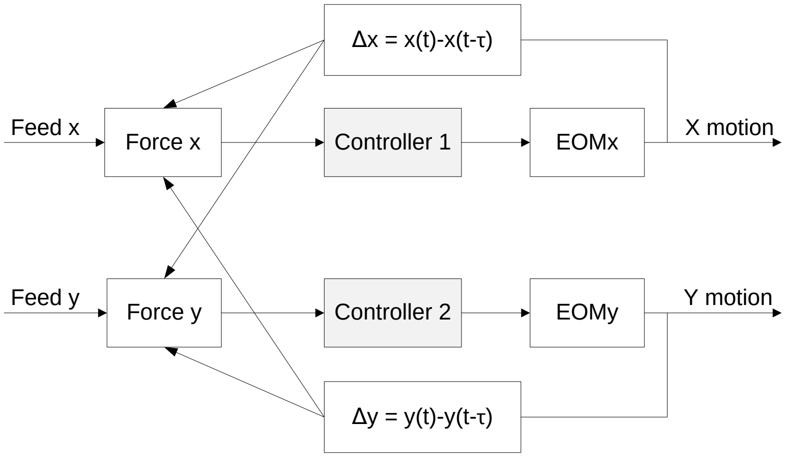

Fig. 5.2 Configuration of multi-variable micro-milling control

The target signal is formulated using the truncated Fourier series of a desired micro-milling state of response. The desired state is defined by a stable vibration amplitude and a bounded frequency response containing the elementary modes that differentiate itself from the instability states of bifurcation and chaos. When the controller is turned on, the system will be restored back to the desired stable state defined by the target signal. The construction of the target signal is briefly reviewed in the followings, followed by an illustrative example in the next section. Fourier series provides an alternate way of presenting a time signal by using harmonic functions of different frequencies. Suppose f is a T-periodic function defined within $[-T/2, T/2]$, then its Fourier series is

$$f(x) \sim \sum_{n=-\infty}^{\infty} c_n e^{2\pi in/T} \tag{5.14}$$

where

$$c_n = \frac{1}{T} \int_{-T/2}^{T/2} f(x) e^{-2\pi in/T} dx \tag{5.15}$$

Assume that *f(k)* is the discrete form of *f(x)* having N points within $[-T/2, T/2]$. The values of *f(k)* outside the interval are assumed to be zeros. Then c_n can be represented as

$$c_n = \frac{1}{T}\frac{T}{N}\sum_{k=-\frac{N}{2}+1}^{\frac{N}{2}} f(k) e^{-\frac{2\pi ink}{N}} = \frac{1}{N} F_n, \;\; n = -\frac{N}{2}+1, \cdots \frac{N}{2} \tag{5.16}$$

where F_n is the Discrete Fourier Transform (DFT) of *f(k)*. A target signal can be reconstructed using Eq. (5.14) by retaining only the frequency components in Eq. (5.16) that represent the fundamental modes of a desired dynamic state that is physically stable.

5.3.1 Control Procedure

The model is simulated at a constant feed rate of 5μm/tooth for different spindle speeds and axial depth-of-cuts (ADOC). The micro–dimensions used in [89] are adopted along with the pearlite material parameters found in [98]. The modal parameters for the tool are assumed to be equal in the X- and Y-direction, and are adopted from [99] since this research utilized a similar 500μm micro-mill. These simulation parameters are summarized in Table 5.1.

Table 5.1: Simulation parameters utilized

Tool Properties from [98]	
Number of Teeth	2
Tool Diameter	500 μm
Tool Nose Radius, Re	2 μm
Rake Angle	8°
Helical Angle	30°
Modal Paramters from [99]	
Tool Natural Frequency	4035 Hz
Stiffness	2142500 N/m
Damping Ratio	0.016

An unstable response is observed for a spindle speed of 63,000 rpm and 100 μm ADOC. Under these cutting conditions, irregularity is observed in both the time and frequency responses using instantaneous frequency (IF) [100]. The time response and IF of the X- and Y-motion are shown in Fig. 5.3. A tool natural frequency at 4,035 Hz and tooth passing frequency at 2,100 Hz are observed. The tooth passing frequency is highly bifurcated as seen in the IF plots of Fig. 5.3 which contain multiple frequency modes below the tooth passing frequency. When the spindle speed is reduced to 60,000 rpm and the ADOC is maintained at 100 μm, the tool response is one of stability (Fig. 5.4). The vibration response has improved with lower vibration amplitude and the IF plot now shows a stable dynamic response containing the 4,035 Hz tool natural frequency and the 2,000 Hz tooth passing frequency. The goal of the research is to improve the dynamic stability of the process. Thus, it is desirable for the unstable response at 63,000 rpm and

100 μm axial DOC (Fig. 5.3) to better compare to the stable response at 60,000 rpm and 100 μm axial DOC (Fig. 5.4). The target signal for the controller is then developed based on the characteristics of the particular stable cutting. The target signal must contain the physically meaningful modes of the process as well as have acceptable vibration amplitudes. Then, the physically meaningful frequencies are retained while the undesirable frequency components are discarded. For the 63,000 rpm case, the target signal contains vibration amplitudes similar to the 60,000 rpm stable response and consists of only the tool natural frequency and tooth passing frequency modes. The reconstructed signal and the reconstruction error of the signal can be seen in Fig. 5.5. The reconstructed signal is fed into the controller as a reference signal. Fig. 5.6 shows that unstable cutting at 63,000 rpm now has a controlled vibration and frequency response when the controller is turned on at 0.2 seconds. The vibration amplitude is reduced to a level similar to that of the stable cutting which will significantly improve the workpiece tolerance and surface quality. The IF plot in Fig. 5.6 also demonstrates an improved frequency response in which the individual modes are now bounded and range over a narrow bandwidth. The phase diagrams and Poincaré sections in Fig. 5.7 indicate that the dynamic state of motion has improved once the controller is initiated. The uncontrolled phase plot and Poincaré section indicate a fractal-like limit cycle while the controlled phase plot and Poincaré section demonstrate quasi-periodic motion with reduced amplitudes and a finite number of well-behaved frequency components.

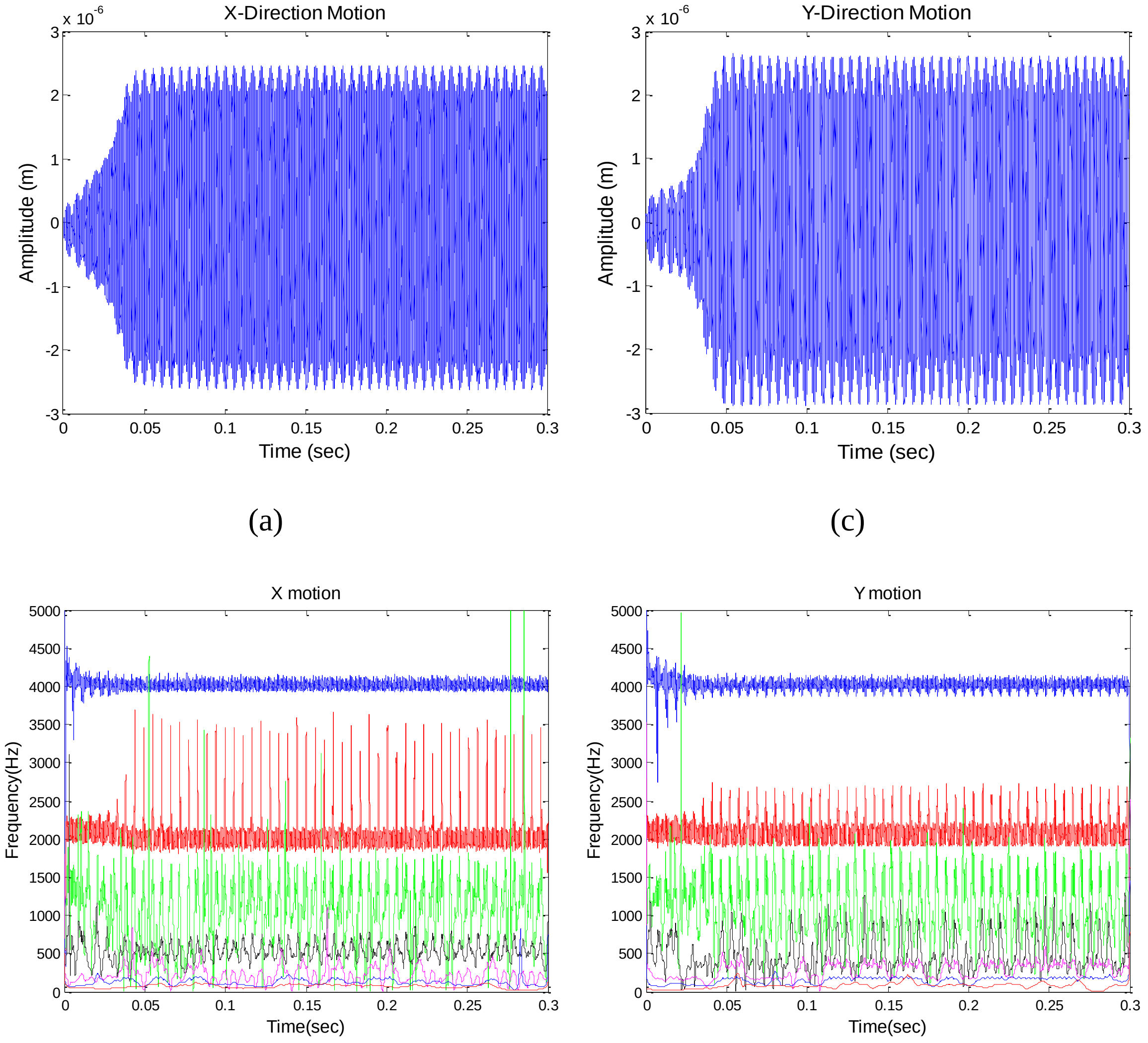

(a) (c)

(b) (d)

Fig. 5.3 (a) Time response and (b) instantaneous frequency of x motion, and (c) time response and (b) instantaneous frequency of y motion when spindle speed = 63,000 rpm and ADOC = 100 μm

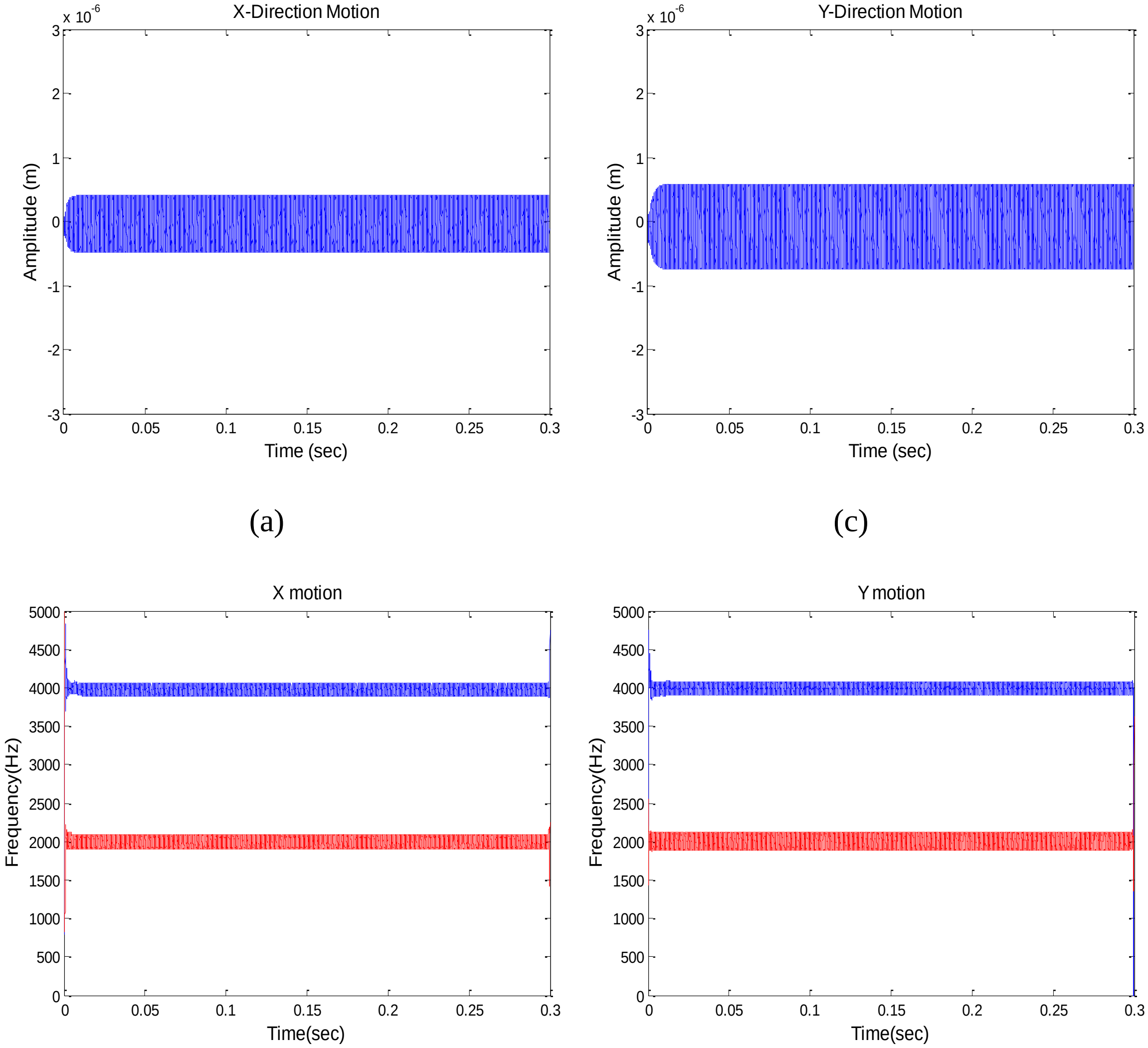

(a)

(c)

(b)

(d)

Fig. 5.4 (a) Time response and (b) instantaneous frequency of x motion, and (c) time response and (b) instantaneous frequency of y motion when spindle speed = 60,000 rpm and ADOC = 100 μm

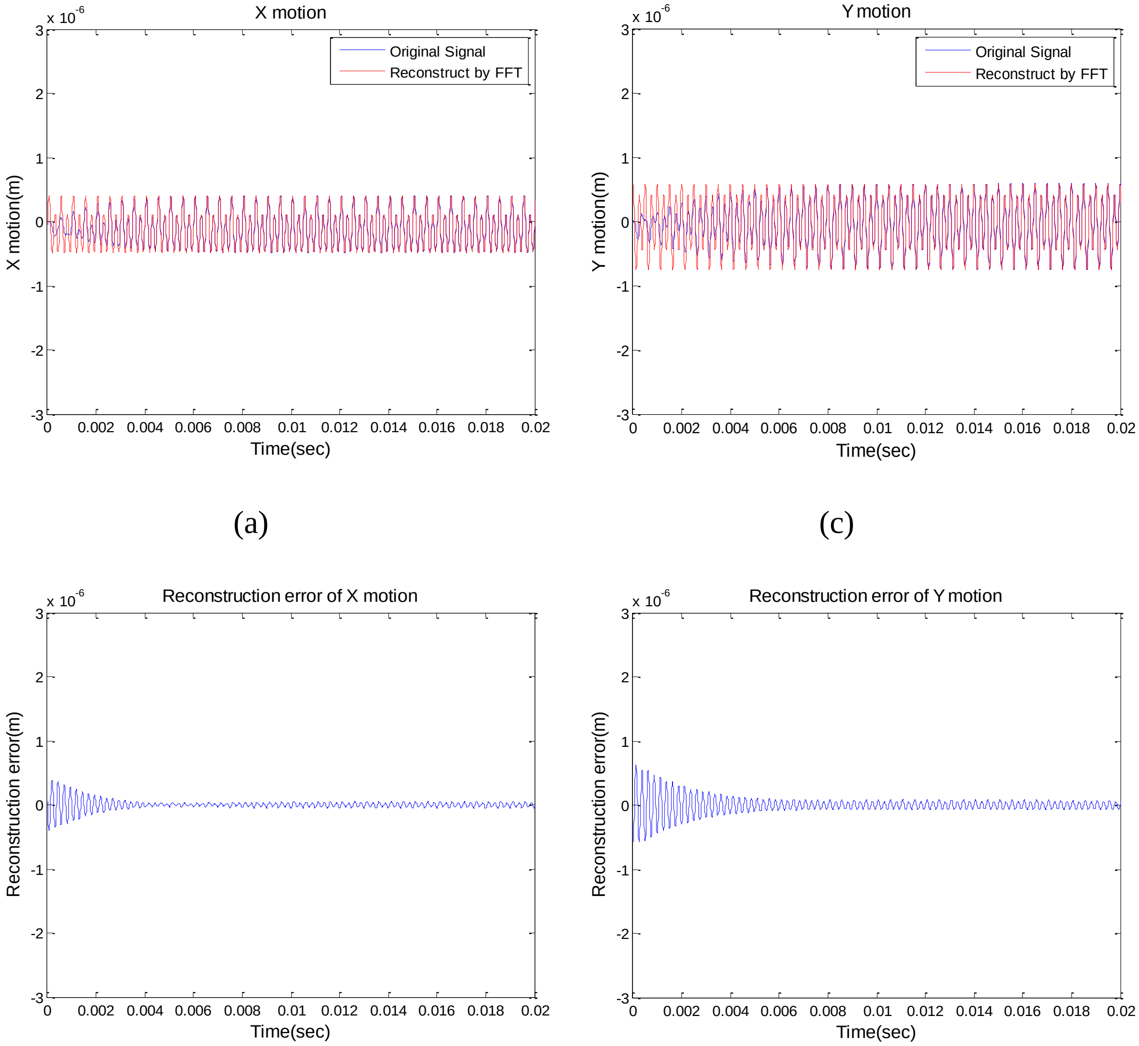

(a) (c)

(b) (d)

Fig. 5.5 (a) Reconstructed target of x motion and (b) reconstruction error of x motion, and (c) reconstructed target of y motion and (d) reconstruction error of y motion

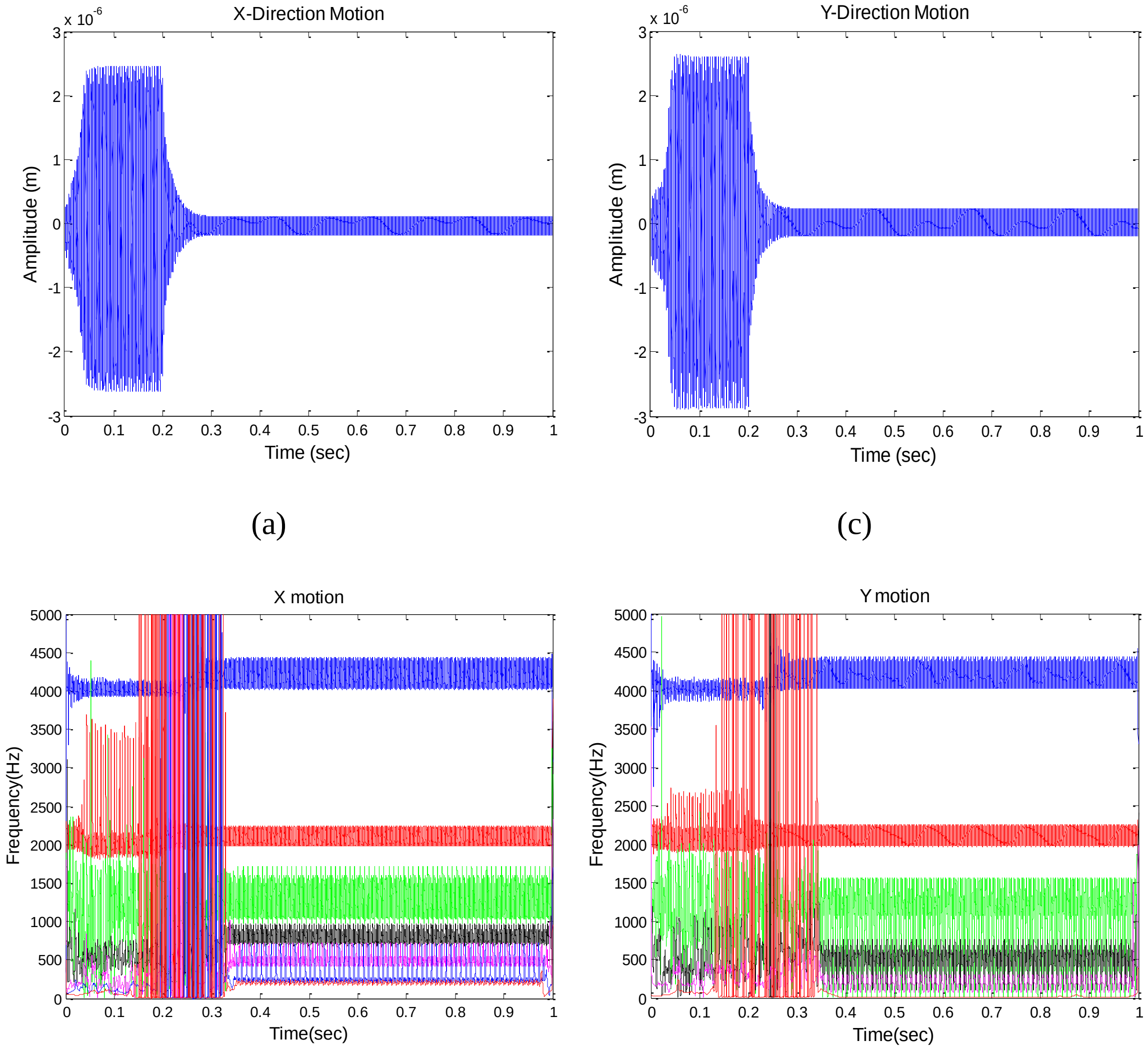

(a)

(c)

(b)

(d)

Fig. 5.6 (a) Time response and (b) IF of x motion, and (c) time response and (b) IF of y motion when spindle speed = 63,000 rpm and ADOC = 100 µm. The controller is turned on at 0.2 second

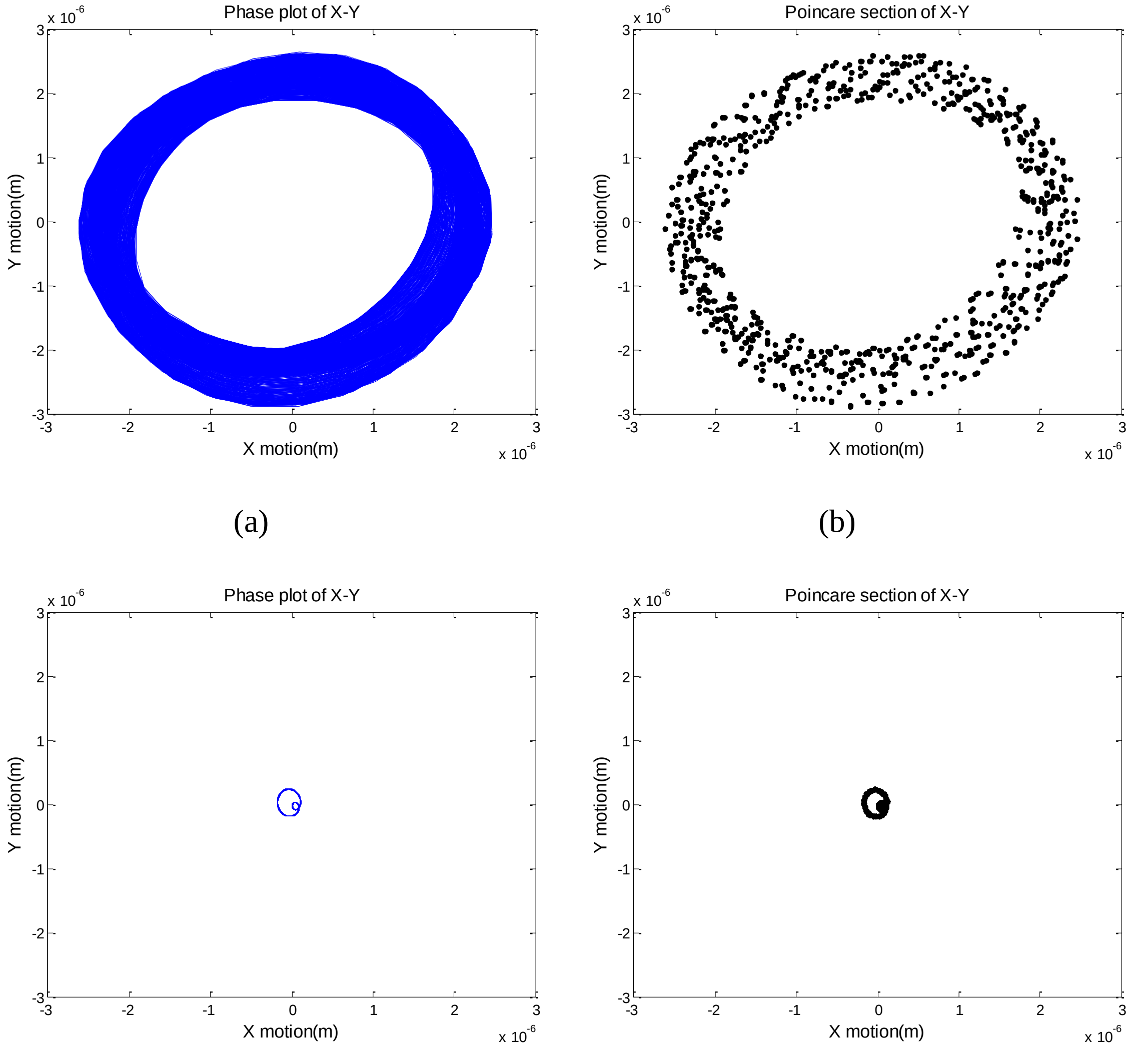

(a) (b)

(c) (d)

Fig. 5.7 (a) Phase plot of x-y and (b) Poincaré section of x-y before controlled, and (c) phase plot of x-y and (b) Poincaré section of x-y after controlled when spindle speed = 63,000 rpm and ADOC = 100 μm

5.4 Numerical Experiment

Control of the micro-milling model for different spindle speed and ADOC are investigated with the assistance of phase portrait, Poincaré section, time response, IF, and cutting forces. Fig. 5.8 shows the phase diagram and Poincaré section when the spindle speed is at 75,000 rpm with an ADOC of 40μm. Before the controller is activated, scattering on the Poincaré section in Fig. 5.8(b) suggests that it is a broadband, chaotic response even though the time response is bounded. After controlled, the phase plot in Fig. 5.8(c) becomes a limit cycle with an amplitude that is 4 times smaller and the Poincaré section in Fig. 5.8(d) shows a periodic motion of a finite number of commensurate frequencies. Fig. 5.9 shows the time response and IF for controlling the milling process. The controller is turned on at 0.1 second and the target signal is designed using the response under the same spindle speed but a smaller ADOC of 30μm. Before 0.1 seconds, the uncontrolled response has an irregular time response amplitude and broadband unstable frequency in both the x- and y-direction. After the controller is on line at 0.1 seconds, the time response amplitude is reduced and the IF is restrained to a narrowband spectrum with a finite number of spectral components. The amplitude of cutting force in both directions is slightly reduced after controlled as shown in Fig. 5.10. The controller maintains the force amplitude around the stable cutting force limit for this particular chip load effectively offsetting the negative impact of increased cutting forces due to dynamic instability.

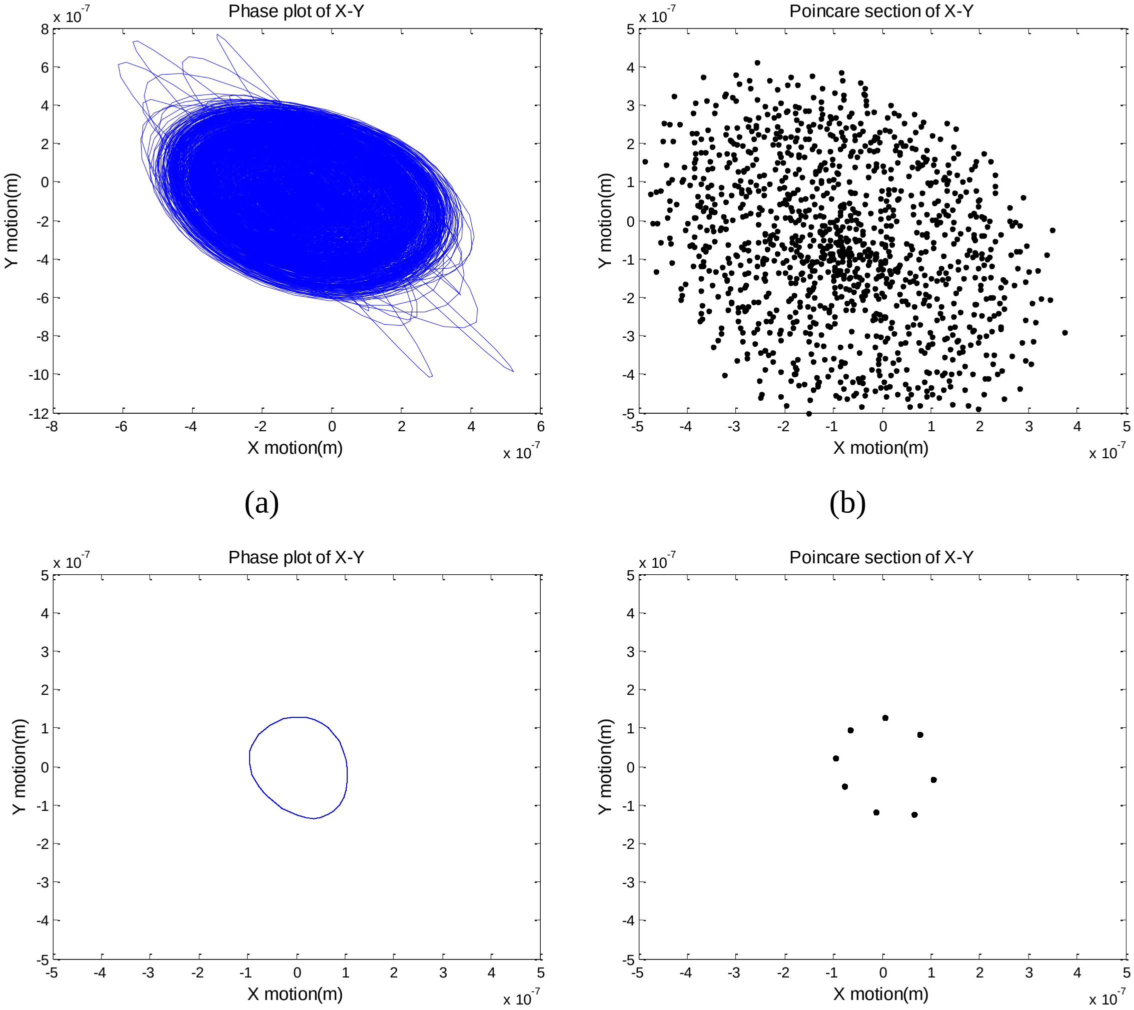

(a) (b)

(c) (d)

Fig. 5.8 (a) Phase plot of x-y and (b) Poincaré section of x-y before controlled, and (c) phase plot of x-y and (b) Poincaré section of x-y after controlled when spindle speed = 75,000 rpm and ADOC = 40 μm

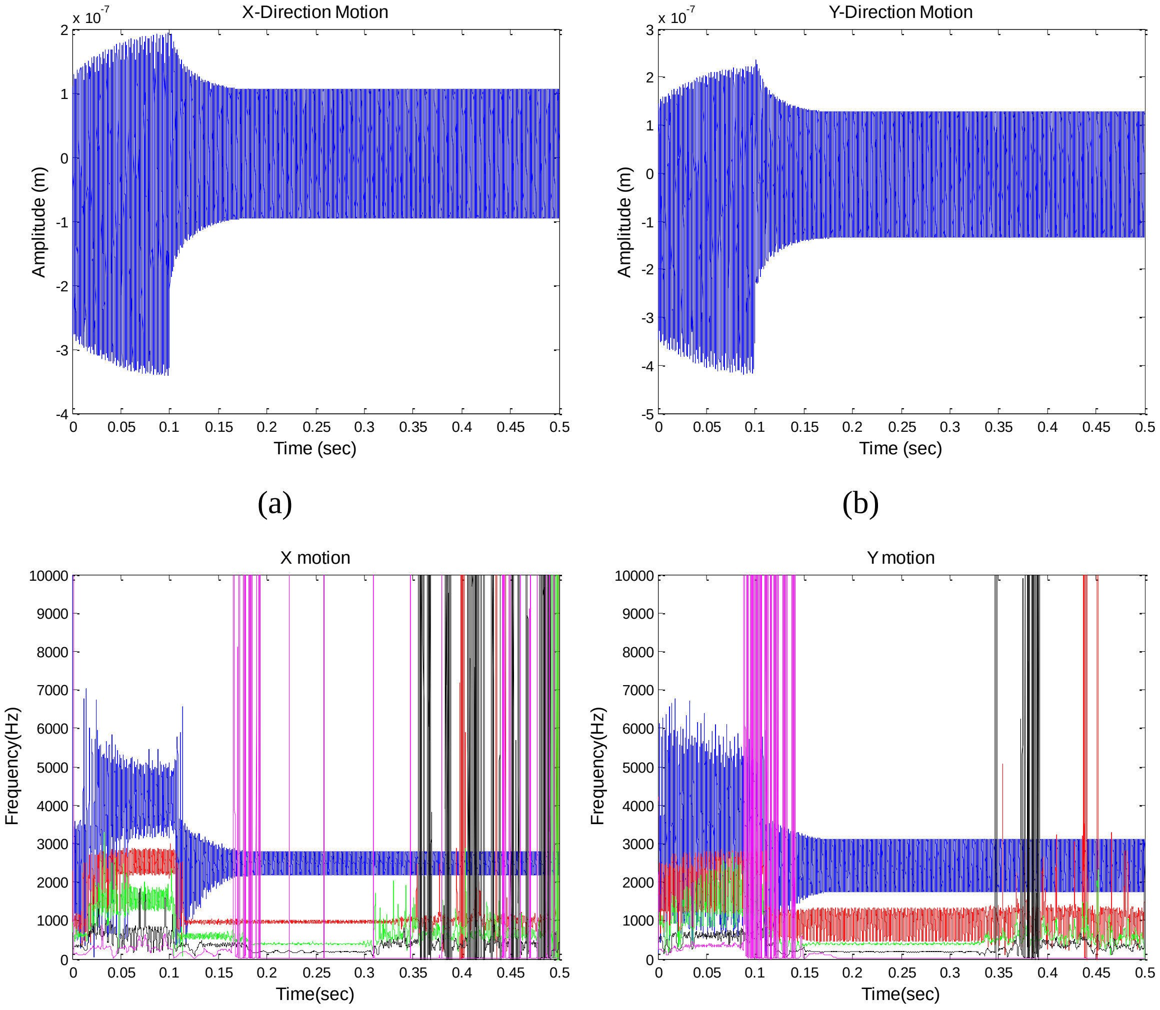

(a) (b)

(c) (d)

Fig. 5.9 (a) Time response and (b) IF of x motion, and (c) time response and (b) IF of y motion when spindle speed = 75,000 rpm and ADOC = 40 μm. The controller is turned on at 0.2 second

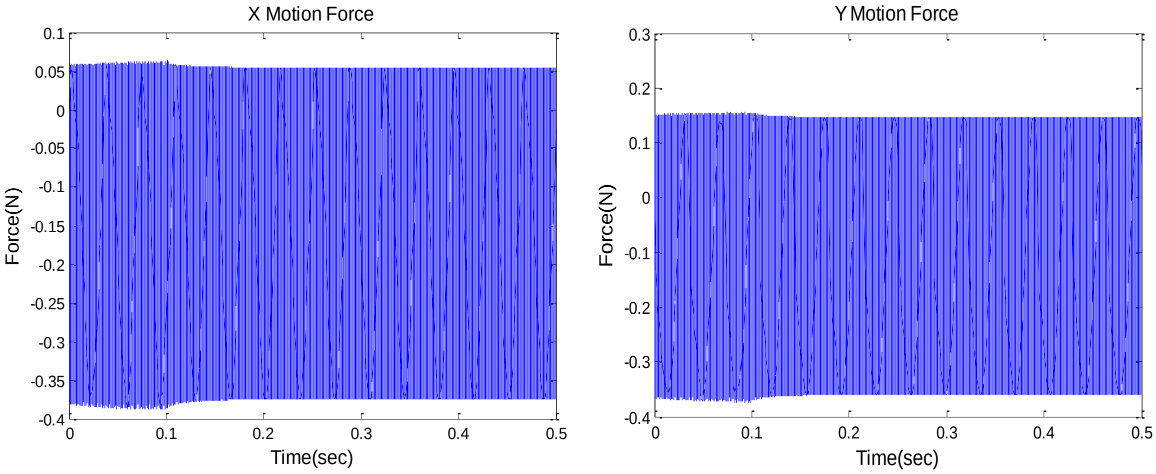

(a) (b)

Fig. 5.10 (a) Force in x-direction (b) force in y-direction when spindle speed = 75,000 rpm and ADOC = 40 μm. The controller is turned on at 0.1 second

When the spindle speed is increased to 90,000rpm with 85μm ADOC, its phase plot represents an unstable limit cycle in Fig. 5.11(a) and the corresponding Poincaré section in Fig. 5.11(b) shows a fractal structure. While not chaotic, it is of a broadband, varying spectrum and thus difficult to control. The target signal is composed from the same spindle speed with a 50μm ADOC. When the controller is on, the response on the phase plot becomes one order-of-magnitude smaller and the Poincaré section becomes localized as shown in Figs. 5.11(c) and 5.11(d), which means that the motion is now an attracting manifold having a frequency response whose bandwidth is significantly reduced. The time response and IF for controlling the milling process are shown in Fig. 5.12. After the controller is applied at 0.1 second, the time response amplitude in both the X- and Y-direction is quickly decreased, thus helping to improve workpiece tolerance. The aberrational temporal oscillation of the instantaneous frequency is regularized and becomes steady oscillation with limited bandwidth, as shown in Fig. 5.12 (c) and (d). The cutting force on both directions is effectively mitigated and restrained after controlled (Fig. 5.13), thus improving the tool life of the process under these cutting conditions.

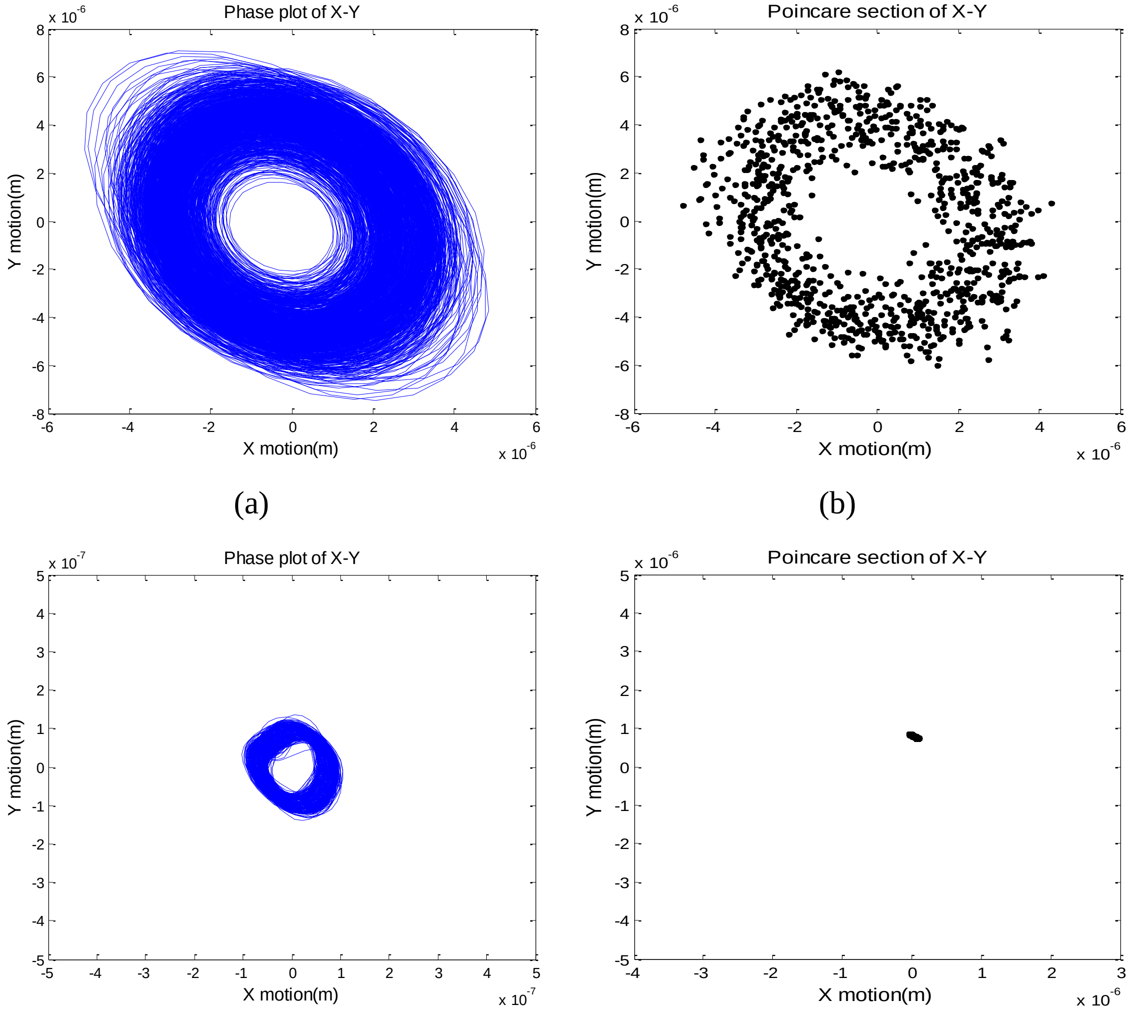

(a) (b)

(c) (d)

Fig. 5.11 (a) Phase plot of x-y and (b) Poincaré section of x-y before controlled, and (c) phase plot of x-y and (b) Poincaré section of x-y after controlled when spindle speed = 90,000 rpm and ADOC = 85 μm

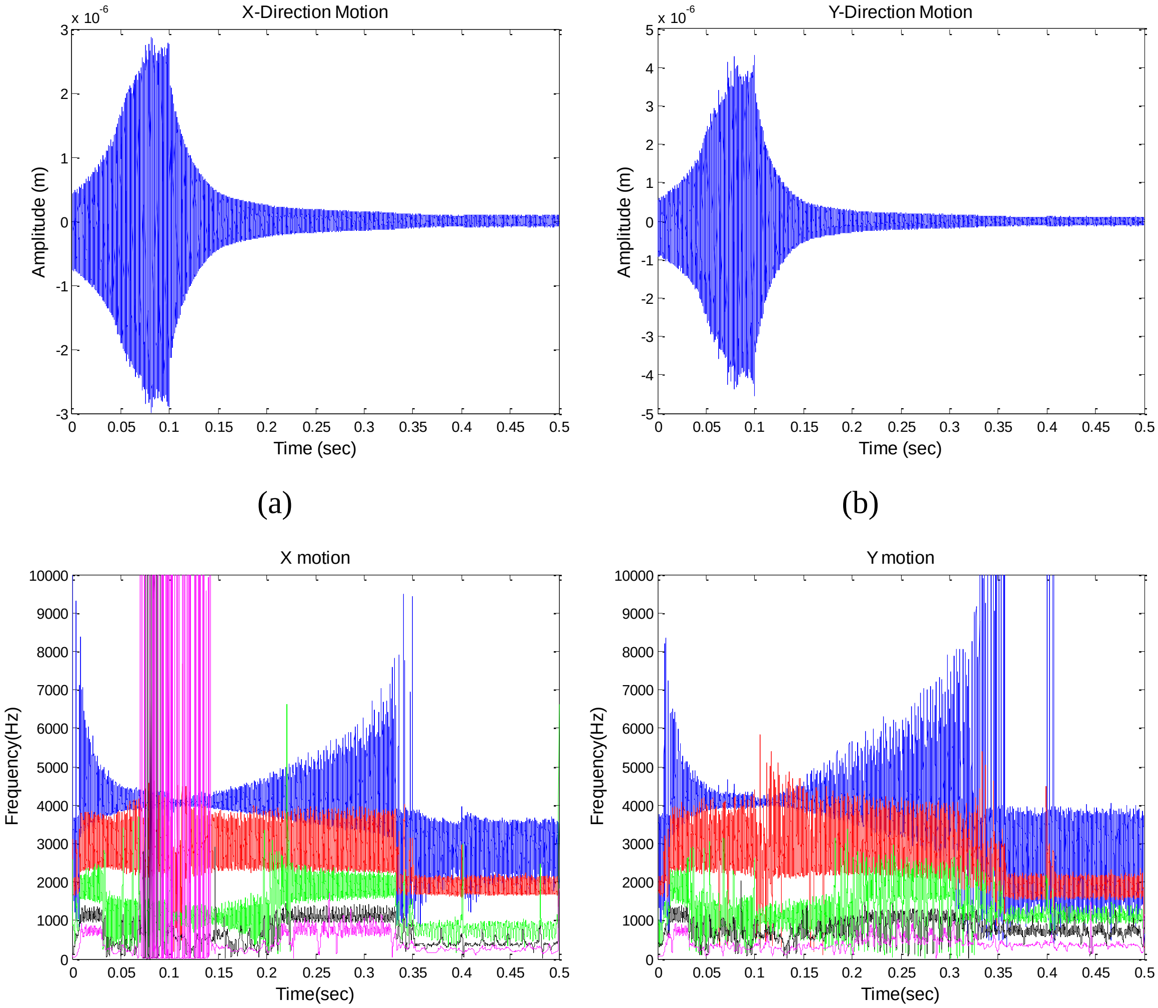

(a) (b)

(c) (d)

Fig. 5.12 (a) time response and (b) IF of x-motion, and (c) time response and (b) IF of y-motion when spindle speed = 90,000 rpm and ADOC = 85 μm. The controller is turned on at 0.1 second

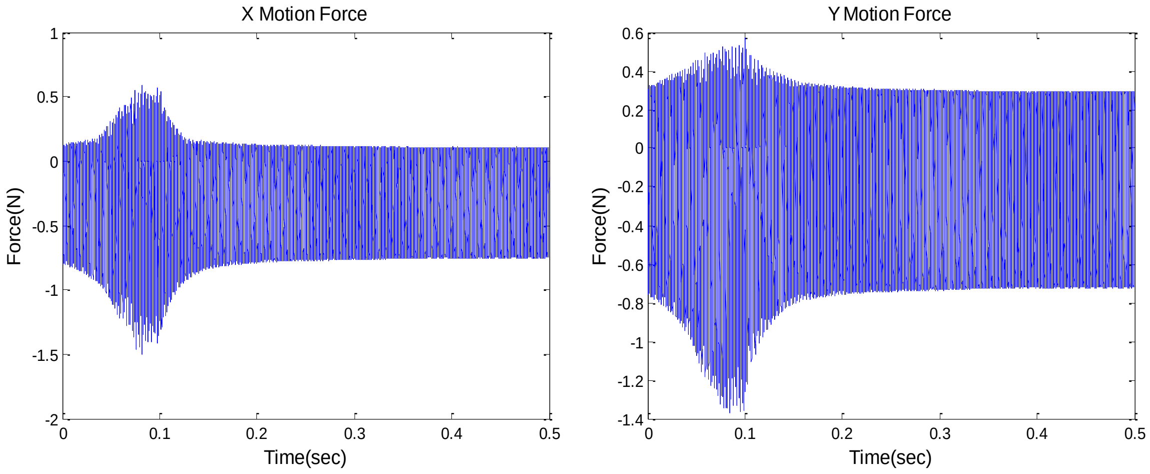

(a) (b)

Fig. 5.13 (a) Force in x-direction (b) force in y-direction when spindle speed = 90,000 rpm and ADOC = 85 μm. The controller is turned on at 0.1 second

At a spindle speed of 180,000 rpm with ADOC of 50 μm, the time response amplitude is increased and becomes extremely irregular. For this case, the target signal is designed from the same spindle speed with a 30 μm ADOC. As all trajectories are seen being repelled from the manifold, the phase diagram and Poincaré section in Fig. 5.14 show an unstable limit cycle with multiple frequencies before controlled. After controlled, the response is reduced to a (quasi) periodic motion with incommensurate frequencies demonstrating an improved dynamic state of motion. Both time response and instantaneous frequency are stabilized in Fig. 5.15 after 0.1 seconds when the controller is brought online. Time response amplitude is reduced and aberrational oscillations in instantaneous frequency are erased when the controller is applied resulting in narrowband frequency components. The cutting force is also reduced as shown in Fig. 5.16 and maintains the stable cutting force limit.

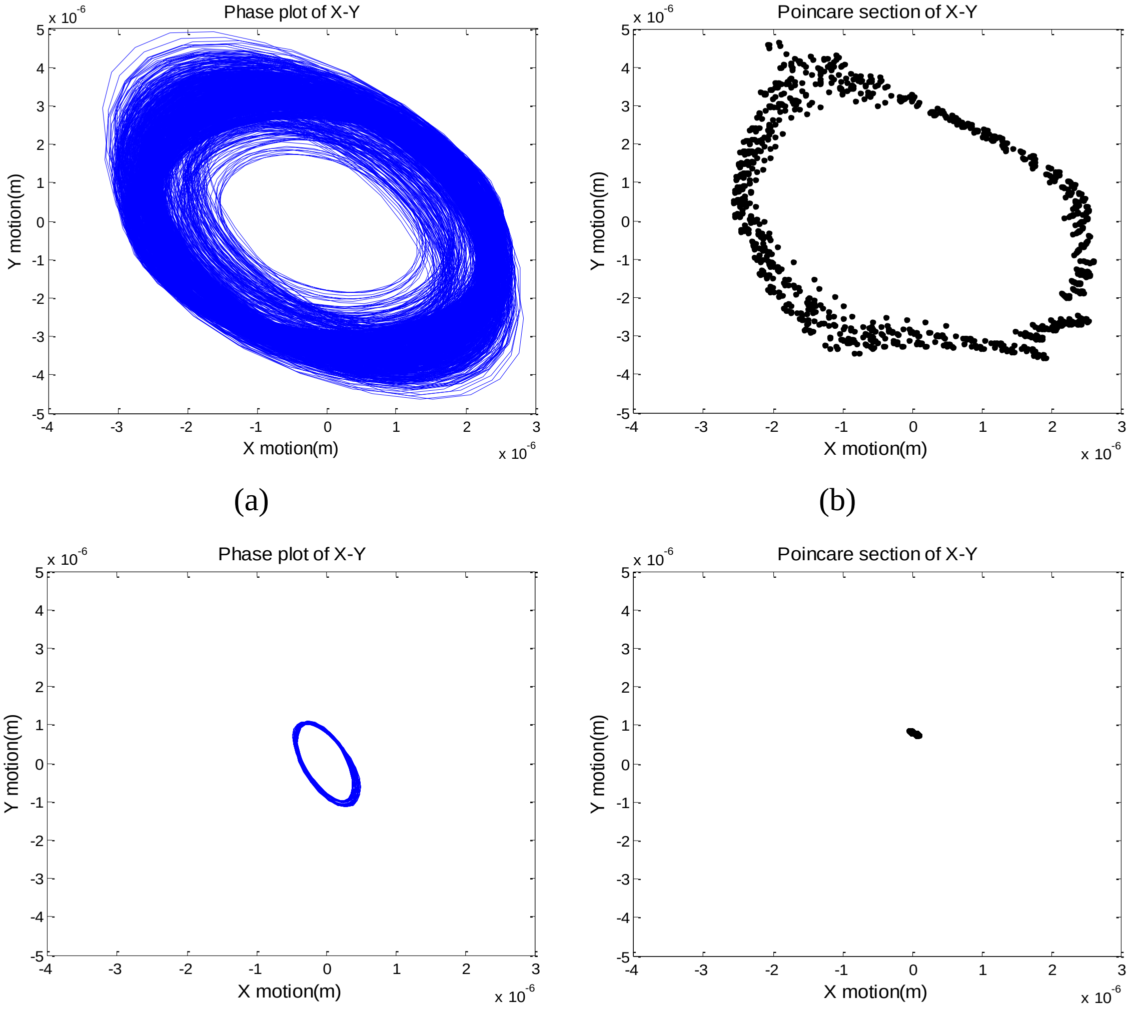

(a) (b)

(c) (d)

Fig. 5.14 (a) Phase plot of x-y and (b) Poincaré section of x-y before controlled, and (c) phase plot of x-y and (b) Poincaré section of x-y after controlled when spindle speed = 180,000 rpm and ADOC = 50 μm

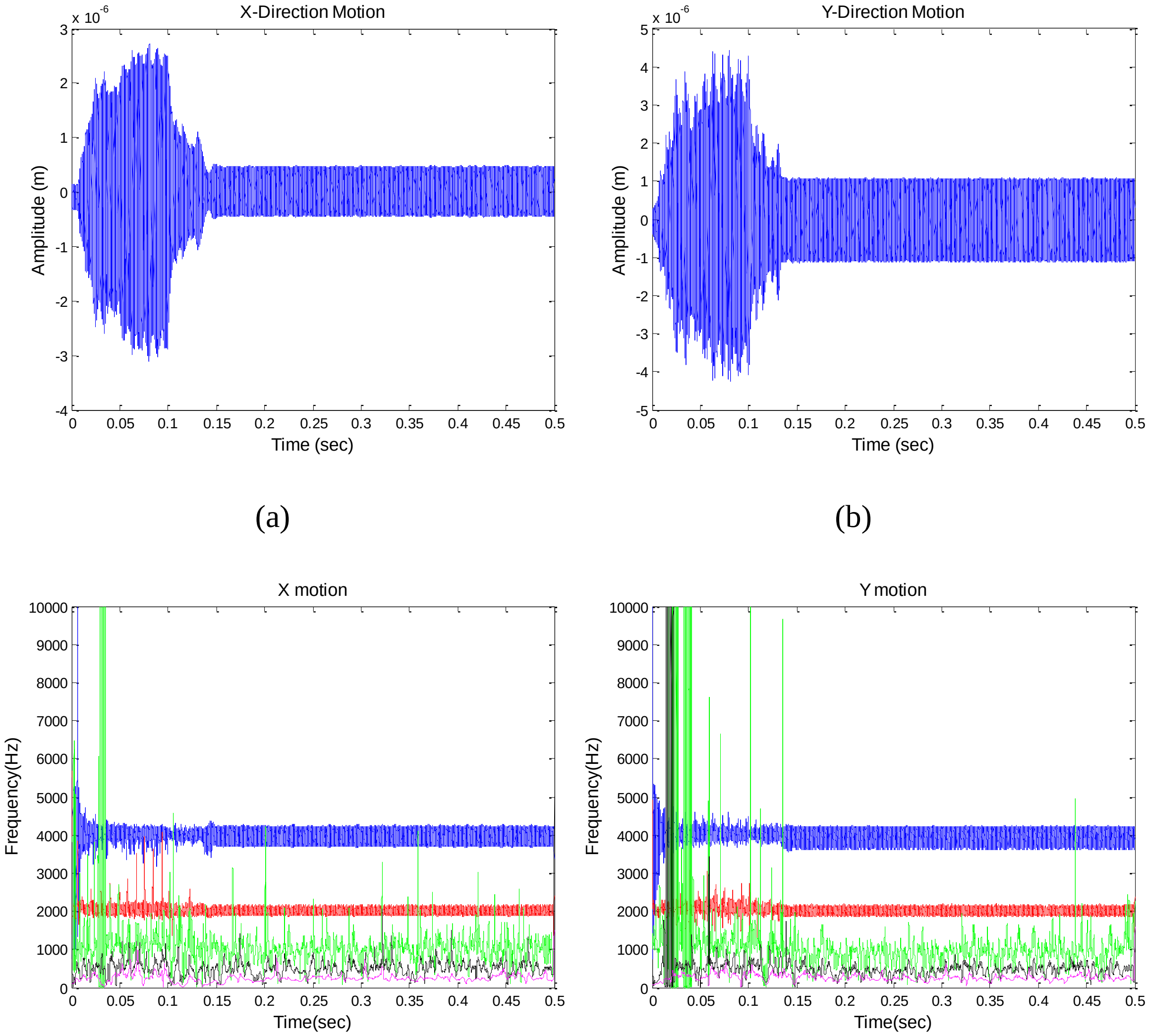

(a) (b)

(c) (d)

Fig. 5.15 (a) time response and (b) IF of x motion, and (c) time response and (b) IF of y motion when spindle speed = 180,000 rpm and ADOC = 50 µm. The controller is turned on at 0.1 second

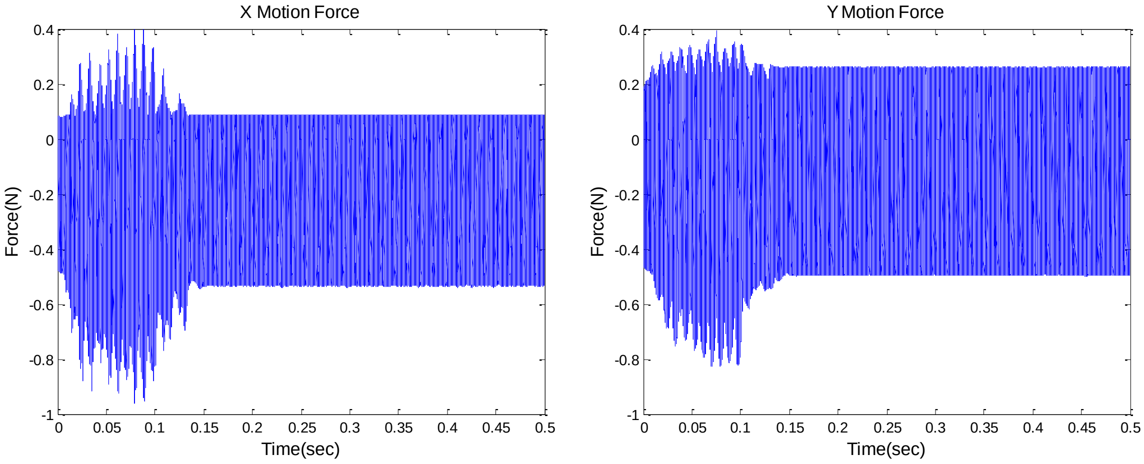

(a) (b)

Fig. 5.16 (a) Force in x direction (b) force in y direction when spindle speed = 180,000 rpm and ADOC = 50 μm. The controller is turned on at 0.1 second

When the spindle speed is 120,000rpm with a 50 μm ADOC, resonance response is generated at the tooth passing frequency which is now coincident with the tool natural frequency. The phase plot and Poincaré section in Figs. 5.17(a) and 5.17(b) show a periodic motion with a single frequency. After the controller is turned on, it indicates a reduction of amplitude in Fig. 5.17(c). The time response and instantaneous frequency in Fig. 5.18 show resonance amplitude and a signal frequency at 4,000Hz. The target signal is designed from the same spindle speed with 30 μm ADOC. The time response amplitude is reduced and its frequency response remains the same after the controller is applied. The amplitude of cutting force on both directions remains the same after controlled (Fig. 5.19). The reduction of the vibration amplitude is significant for improving product quality for high speed cutting.

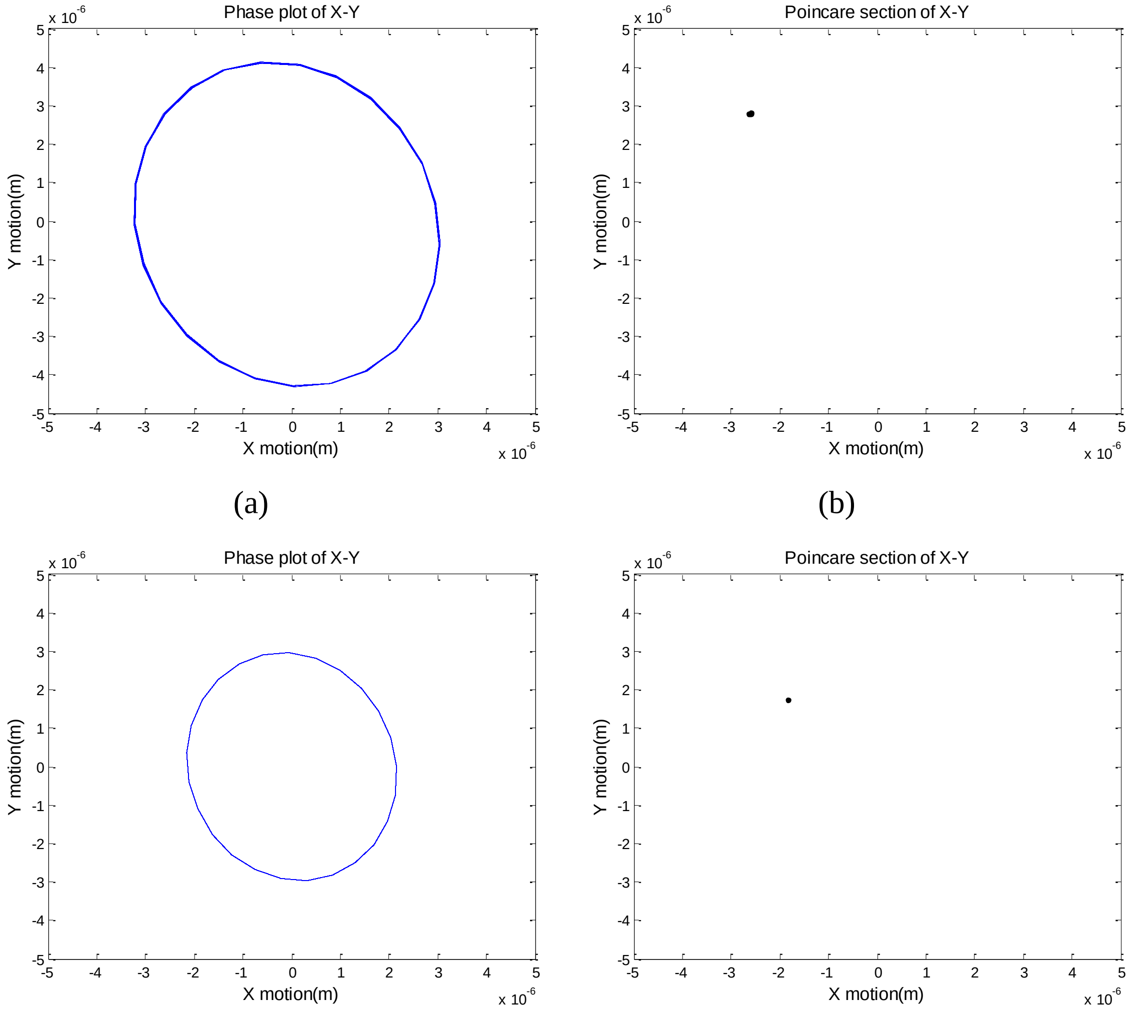

(a) (b)

(c) (d)

Fig. 5.17 (a) Phase plot of x-y and (b) Poincaré section of x-y before controlled, and (c) phase plot of x-y and (b) Poincaré section of x-y after controlled when spindle speed = 120,000 rpm and ADOC = 50 μm

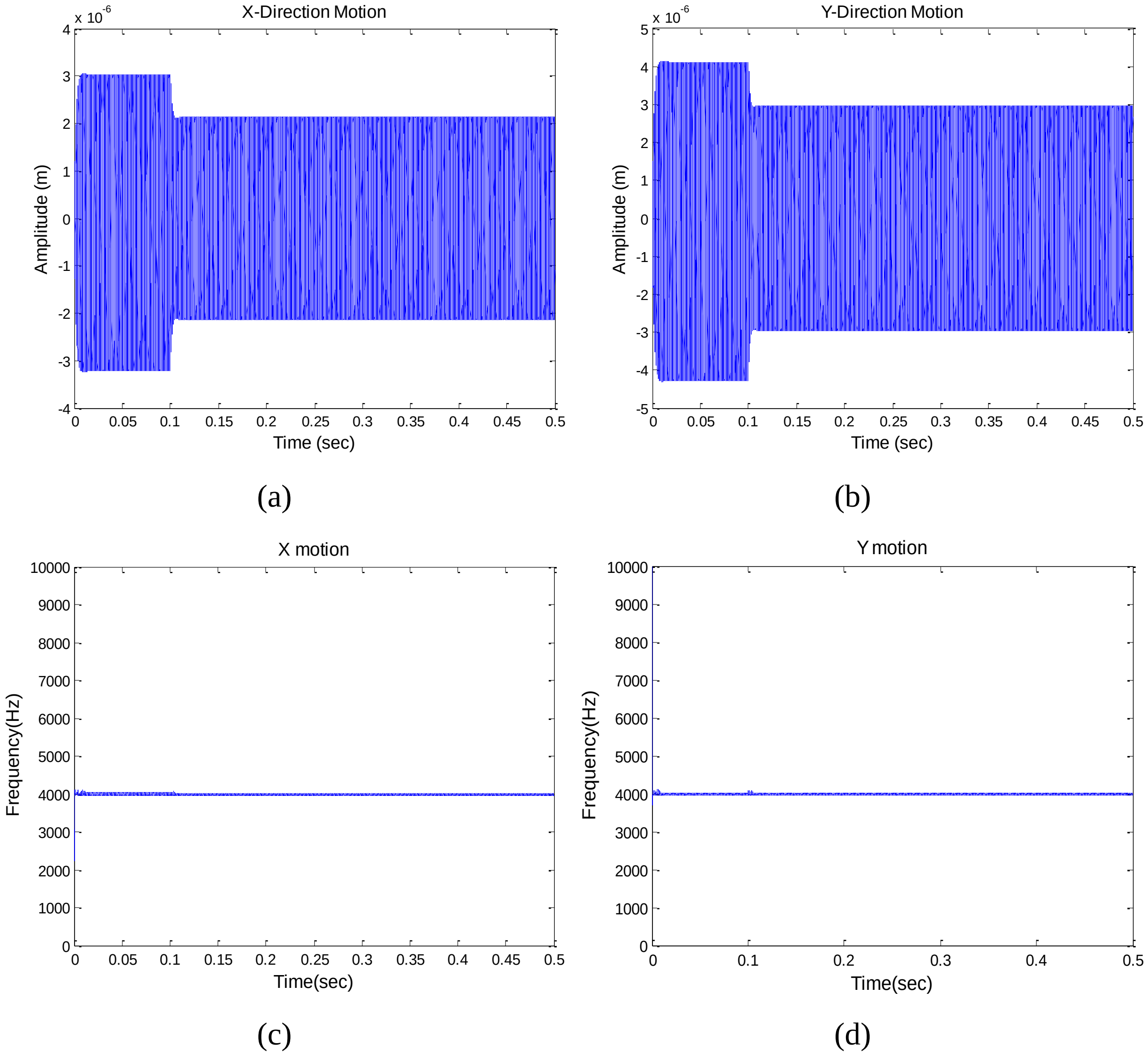

(a) (b)

(c) (d)

Fig. 5.18 (a) Time response and (b) IF of x motion, and (c) time response and (b) IF of y motion when spindle speed = 120,000 rpm and ADOC = 50 μm. The controller is turned on at 0.1 second

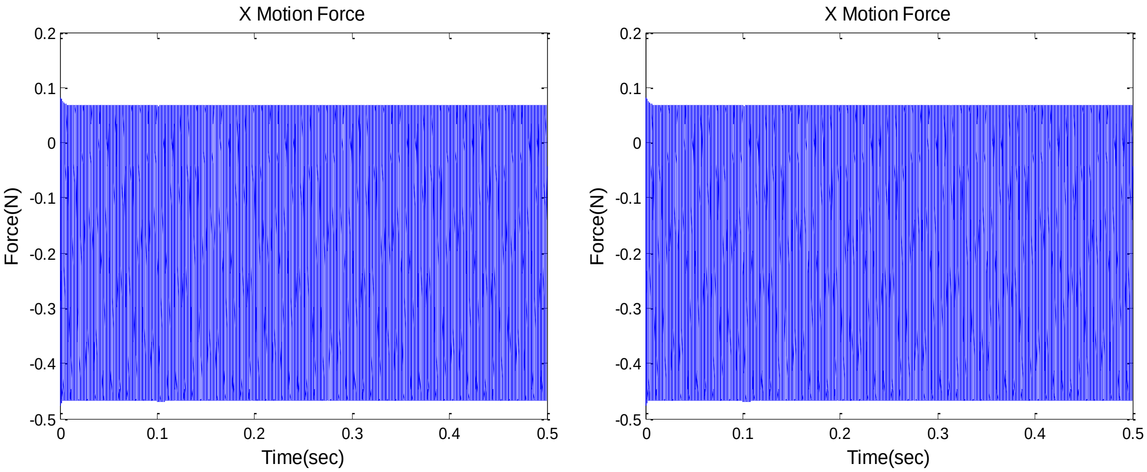

Fig. 5.19 (a) Force in x direction (b) force in y direction when spindle speed = 120,000 rpm and ADOC = 50 μm. The controller is turned on at 0.1 second

5.5 Summary

The micro-milling process is highly sensitive to dynamic instability which can result in premature tool breakage, increased wear rates, and poor workpiece quality. To achieve reasonable material removal rates while keeping the chip load at a minimum, high spindle speeds are desired in micro-milling. This high frequency excitation of the system increases the effect of nonlinearity on the dynamic response negatively impacting cutting performance by introducing increasingly broad frequency spectra as instability develops. This suggests that both the time and frequency domains should be considered to effectively control micro-milling, and a micro-milling model capable of capturing the high frequency signature of the process is required for testing control algorithm. A simultaneous time-frequency controller was applied to a nonlinear multi-dimensional micro-milling model in order to control and improve the dynamic response under various spindle speed and ADOC conditions which resulted in an unstable dynamic state of motion. To control the process, two independent nonlinear controllers were placed in front of the model to regulate the cutting force excitation, and a target signal having all the physically meaningful frequency modes and acceptable amplitudes was utilized. The controller was applied to unstable cutting for spindle speed excitations ranging from 63,000 rpm to 180,000 rpm. For each case, the controller demonstrated the ability to reduce the vibration amplitude of the system, which is important for improving process efficiency and achieving and maintaining high precision cutting at a wide range of spindle speeds. The cutting forces were also observed to be properly mitigated and controlled to the stable cutting force values for that particular feed rate and ADOC. The controller prevented the negative effect of increasing cutting forces due to dynamic instability, thus simultaneously improving the life of the tool and negating immediate tool failure for unstable high speed excitation. The instantaneous frequency plots, phase portraits, and Poincaré plots illustrated the improved dynamic state of motion in the time-frequency domain after the controller was applied. This was observed by a reduction in the bandwidth of the frequency response, ultimately improving tool life and the wear rate. The application of the simultaneous time-frequency controller to the highly nonlinear micro-milling process at high speed excitation demonstrated the capability of mitigating the process in both the time and frequency domains with significantly improved tool performance and workpiece quality.

6. SYNCHRONIZATION OF CHAOS IN SIMULTANEOUS TIME AND FREQUENCY DOMAIN

6.1 Introduction

Chaos synchronization can be categorized into complete, practical, partial, and almost synchronization [101, 102]. The simplest synchronization method is complete replacement, which substitutes the variable in the response system with the corresponding variable being passed from the drive system [101]. The stable synchronization can also be achieved by replacing the variable only in certain locations, called partial replacement. The drive and response systems can also be coupled by adding a damping term that consists of a difference between the drive and the response variables. However, most studies have the configuration of the synchronization scheme determined through trial by error.

Lyapunov stability theory is often adopted when formulating chaos synchronization methods. Proper rule of update for unknown parameters and control law for compensating the external excitation are designed to make the Lyapunov function candidate compatible with the stability requirement [103]. Synchronization can be robustly achieved for identical or dissimilar chaotic systems without the calculation of the conditional Lyapunov exponents. Adaptive backstepping control law is applied to ensure that the error between the drive and response system is asymptotically stable [104, 105]. It derives Lyapunov function candidate in sequence for each variable, progressively stepping back from the overall system and securing the stability for each variable. To identify the chaotic system simultaneously, adaptive control law is derived from Lyapunov theory to define the convergence and stability of the error dynamic equation [106-108]. It is able to accommodate the unknown parameters and system uncertainty. An adaptive sliding mode controller is used to synchronize non-autonomous system with a sinusoid driving term [109, 110]. Designed to make the derivative of the Lyapunov function negative, the switching control law is formulated from Lyapunov theory to guarantee the asymptotical stability and convergence on the sliding surface of the error state space equation. The continuous input thus obtained can withstand uncertainties and disturbances. This is a quality common of all synchronization methods. Control laws thus formulated, nevertheless, are neither intuitive nor lending themselves to sound physical interpretation. In addition, they require that the system structure and parameters be explicitly known. This requirement is even more mandatory for non-autonomous and nonstationary systems, so that the control law can be properly designed to cancel out the external forcing term. The Lyapunov function needs to be found based on heuristic methods and can only be applied to relatively simple systems. Thus, methods based on the Lyapunov stability theory are not viable for complex, nonstationary systems of unknown or unspecified nature.

Linear control theories are also applied to synchronization of chaos. Two different chaotic systems are synchronized by assigning proper control law to make the error dynamic equation linear [111, 112]. Linear stability theory, such as calculating the eigenvalues of the state matrix, is used to define stability. Linear feedback control is applied to synchronize two identical chaotic systems [113]. The system is linearized by Jacobin and the Routh-Hurwitz stability criterion is followed to identify the feedback gain to suppress chaos to unstable equilibria. Two linearly coupled chaotic systems are synchronized by assigning the proper parameters to satisfy the Routh-Hurwitz stability criterion [114]. Synchronization method of the particular construct either designs a linear error dynamic equation by choosing a specific drive-response chaotic system pair or adopts Jacobin to the state matrix. However, linear error dynamic equation can only be acquired for limited drive-response pair and uncertainties of the system are not allowed. Such is basically a trial-and-error method with limited applicability. Jacobin is in fact a linearization method that can only be applied to the adjacent area of the pre-determined fixed point. Its sensitivity to disturbances renders its suitability only for stationary systems. For nonstationary systems, once the trajectory deviates away from the fixed point, the stability is no longer valid.

Synchronization of delayed differential equations is also reported, including identical dissipative chaotic systems with nonlinear time-delayed feedback that are unidirectionally coupled and synchronized [115]. The synchronization threshold of the coupled time-delay chaotic system is analytically estimated by calculating the Lyapunov exponents [116]. Time-delayed feedback term is added into the control law to synchronize two identical Lur’s systems by using the Lyapunov stability theory to ensure stability [117-119]. The delay time is often heuristically decided, however. If more than one variable needs to be passed to the response system, synchronous substitution is used to define a new variable as a function of multiple variables [120].

This new variable is transmitted to the response system and recovered by inverting the transformation. The synchronization of a non-autonomous chaotic system in [121] specifies an identical sinusoidal forcing term of different phases to both the drive and response systems. A strobe signal is used to form a feedback loop and modulate the frequency of the function generator to provide the sinusoidal excitation for the response circuit. In general, chaos synchronization methods of late, though functional, are with limited applications only for the well-defined situations. The chaos control concept in [96] that demonstrates feasibility in dealing with chaotic systems whose responses deteriorate in the time and frequency domains concurrently will be applied in the following sections to synchronize the non-autonomous chaotic system discussed in [121] with different external excitations. Instantaneous frequency (IF) along with marginal spectrum will also be employed to resolve the nonlinearity of the response as well as evaluate the performance of the presented synchronization scheme.

6.2 Dynamics of a Non-autonomous Chaotic Circuit

A non-autonomous chaotic circuit with a sinusoidal forcing term [121] is explored for the study. The circuit, which is a periodically forced chaotic system preferred for its superior insensitivity to noise than the autonomous systems, is as follows

$$\frac{dx}{dt} = \beta(y - z) \tag{6.1}$$

$$\frac{dy}{dt} = \beta\big(-\Gamma_y y - g(x) + \alpha\cos(\omega t)\big) \tag{6.2}$$

$$\frac{dz}{dt} = \beta(f(x) - \Gamma_z z) \tag{6.3}$$

where $g(x) = -3.8 + (1/2)(|x + 26| + |x - 2.6| + |x + 1.2| + |x - 1.2|)$ and $f(x) = \frac{1}{2}x + |x - 1| - |x + 1|$. *g(x)* and *f(x)* are piecewise linear functions based on a diode function generator. Parameters $\alpha = 0.2,\ \Gamma_y = 0.2,\ \Gamma_z = 0.1, \text{and}\ \beta = 10^4$ follow from [121] and ω = $2\pi f_d$ has the linear forcing frequency f_d = 769Hz. The circuit configuration described by Eq. (6.1)-(6.3) is illustrated in [121]. The circuit is numerically time-integrated using a 10^{-4} s time step subject to the [*x y z*] = [0 0 0] initial conditions. Fig. 6.1 shows the phase diagram and Poincaré section of the chaotic responses in the *x*-*y*, *x*-*z*, and *y*-*z* planes. The phase portraits in Fig. 6.1(a)-(c) have limit cycle-like trajectories overlapping each other, representing a nonstationary frequency oscillation with a limited spectral bandwidth; while the Poincaré sections in Fig. 6.1(d)-(f) demonstrate fractal structures in each dimension. To resolve the hidden nonlinearity indicated in Fig. 6.1 for the non-autonomous chaotic circuit, instantaneous frequency (IF) along with marginal spectrum [96] is applied in the following sections.

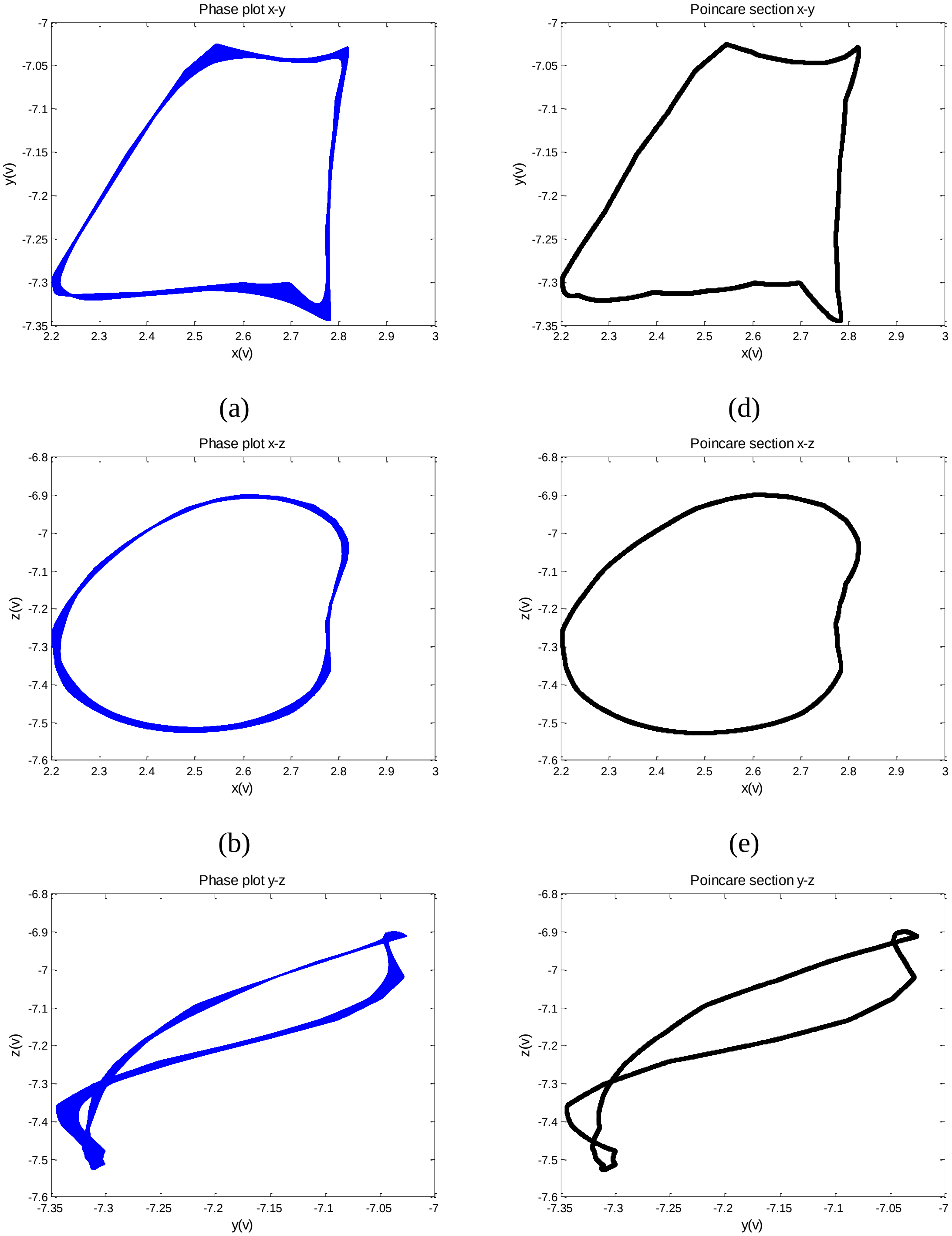

(a) (d)

(b) (e)

(c) (f)

Fig. 6.1 Phase diagram and Poincaré section

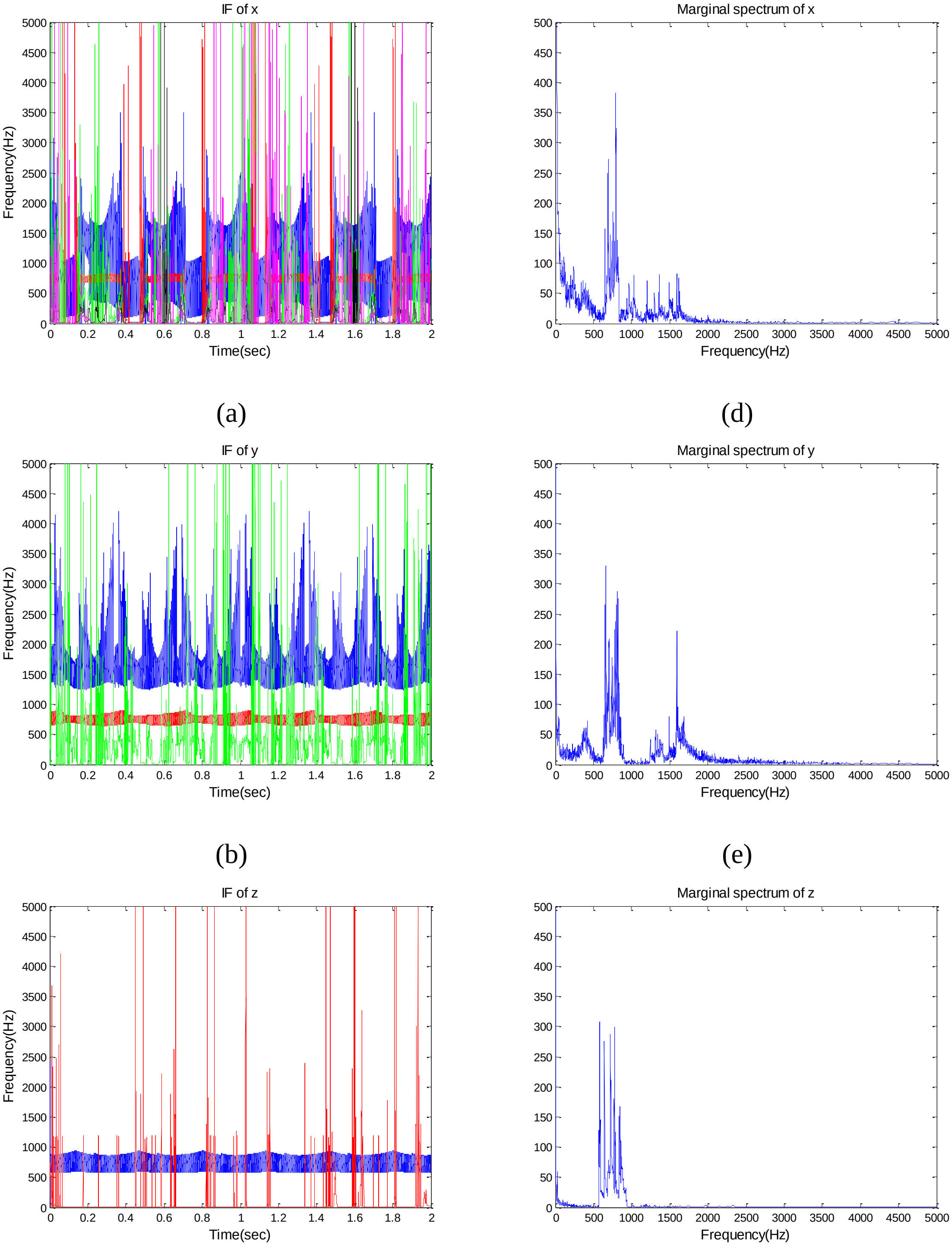

(a) (d)

(b) (e)

(c) (f)

Fig. 6.2 Instantaneous frequency (IF) and marginal spectrum

The IF of the x-motion in Fig. 6.2(a) shows prominent temporal oscillations of the first frequency mode along with other aberrational irregular modes. The corresponding marginal spectrum in Fig. 6.2(d) indicates a broad bandwidth response up to 2500 Hz and a frequency cluster at 500-1000Hz. The IF and marginal spectrum of the y-motion in Figs. 6.2(b) and 6.2(e) are similar to those of the x-motion, both demonstrating temporal oscillations of the IF and broad marginal spectra. Showing also oscillating broadband frequencies at 500-1000Hz, Figs. 6.2(c) and 6.2(f) likewise indicate that the non-autonomous circuit generates chaotic responses subject to certain parameters.

6.2.1 Synchronization Scheme

The scheme of cascaded drive-response in [122] is adopted to synchronize the drive and the response circuits. As shown in Fig. 6.3, the variable x of the drive system in Eq. (6.1), completely replaces the corresponding variable x_1 in the subsystem in Eq. (6.4) to determine the secondary driving variable z_1. Then z_1 is used to substitute the corresponding variable z_2 in Eq. (6.5) to solve for x_2 and the variable y_2 in Eq. (6.6), the response system. Thus when synchronized, all the variables in the driving system (x, y, z) equal to the corresponding variables (x_2, y_2, z_2). The objective of the synchronization is to reproduce the chaotic response of the driving system. In Fig. 6.3, a sinusoidal forcing term, $\alpha_r \cos(\omega t + \theta)$, which has the same frequency as the forcing term in the driving system but different amplitude and phase shift, is used in the response system. The chaotic controller is used to eliminate the difference between the chaotic signal x and the corresponding signal x_2 by adjusting the sinusoidal forcing term.

A high frequency noise during the transmission is infused as *d(t)*. The dynamic equation of the response system is as follows,

$$\frac{dz_1}{dt} = \beta(f(x_1) - \Gamma_z z_1) \tag{6.4}$$

$$\frac{dx_2}{dt} = \beta(y_2 - z_2) \tag{6.5}$$

$$\frac{dy_2}{dt} = \beta\left(-\Gamma_y y_2 - g(x_2) + \alpha_r \cos(\omega_r t + \theta)\right) \tag{6.6}$$

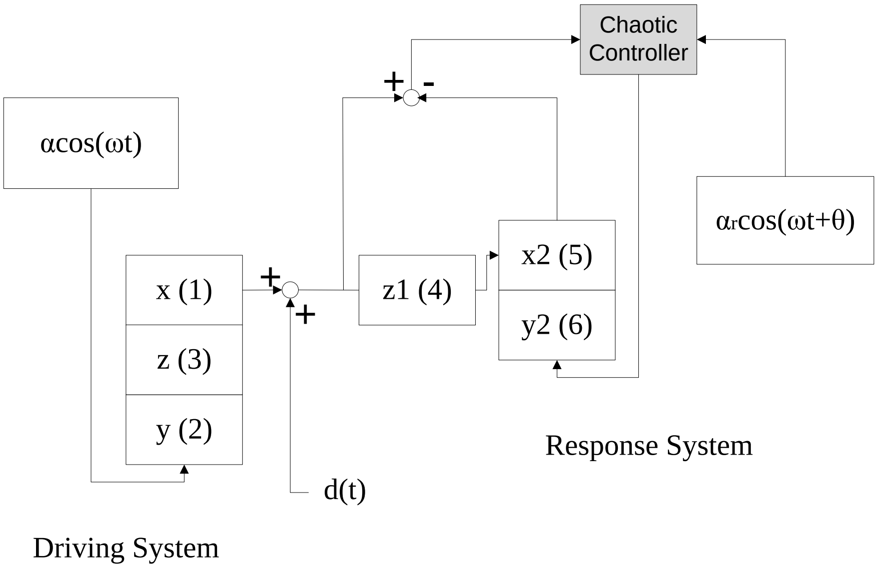

Fig. 6.3 Synchronization scheme

6.3 Synchronization of Chaos

6.3.1 Scenario I

The drive and response systems are subject to different initial conditions and driving forces of dissimilar amplitudes and phases. The chaotic circuit in Eqs. (6.1) – (6.3) is the drive system and the variable x is transmitted to the response system defined in Eqs. (6.4) – (6.6). The initial conditions specified for the response system are $[x, y, z] = [2, 2, 2]$ and the driving term is set as $\alpha_r \cdot \cos(2\pi \cdot \omega_d + \theta)$, with $\alpha_r = 0.4, \omega_d = 769,$ and $\theta = \pi/2$. To observe the difference between the drive and the response systems, their phase portrait are drawn on the same scale and compared in Fig. 6.4. Their output trajectories locate at the same basin in the state space. It is shown that the output of the drive and the response systems share the same traits but are of different magnitudes, indicating that they are unsynchronized and of different chaotic responses.

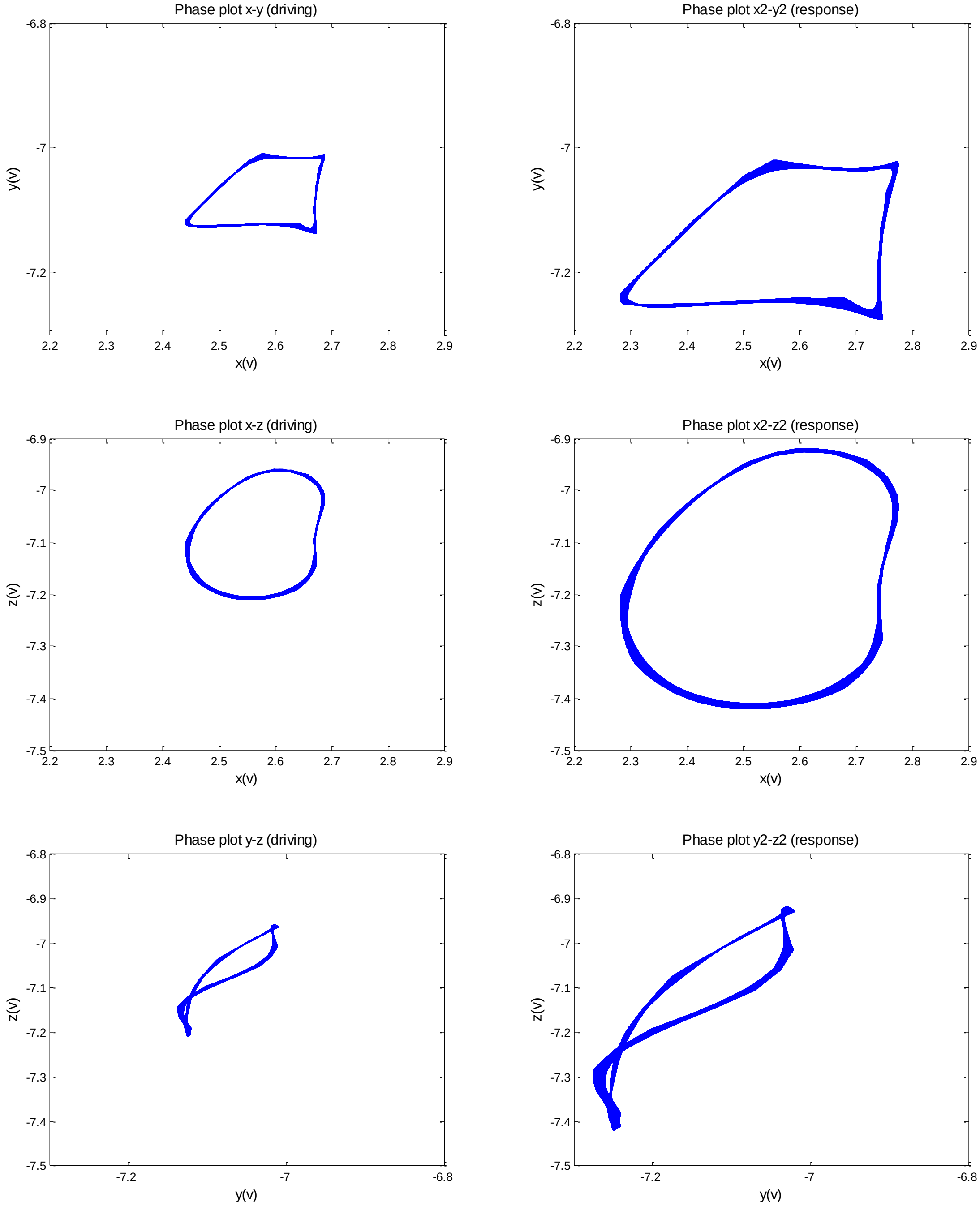

Fig. 6.4 Phase diagrams of the output of the drive (left) and response (right) systems

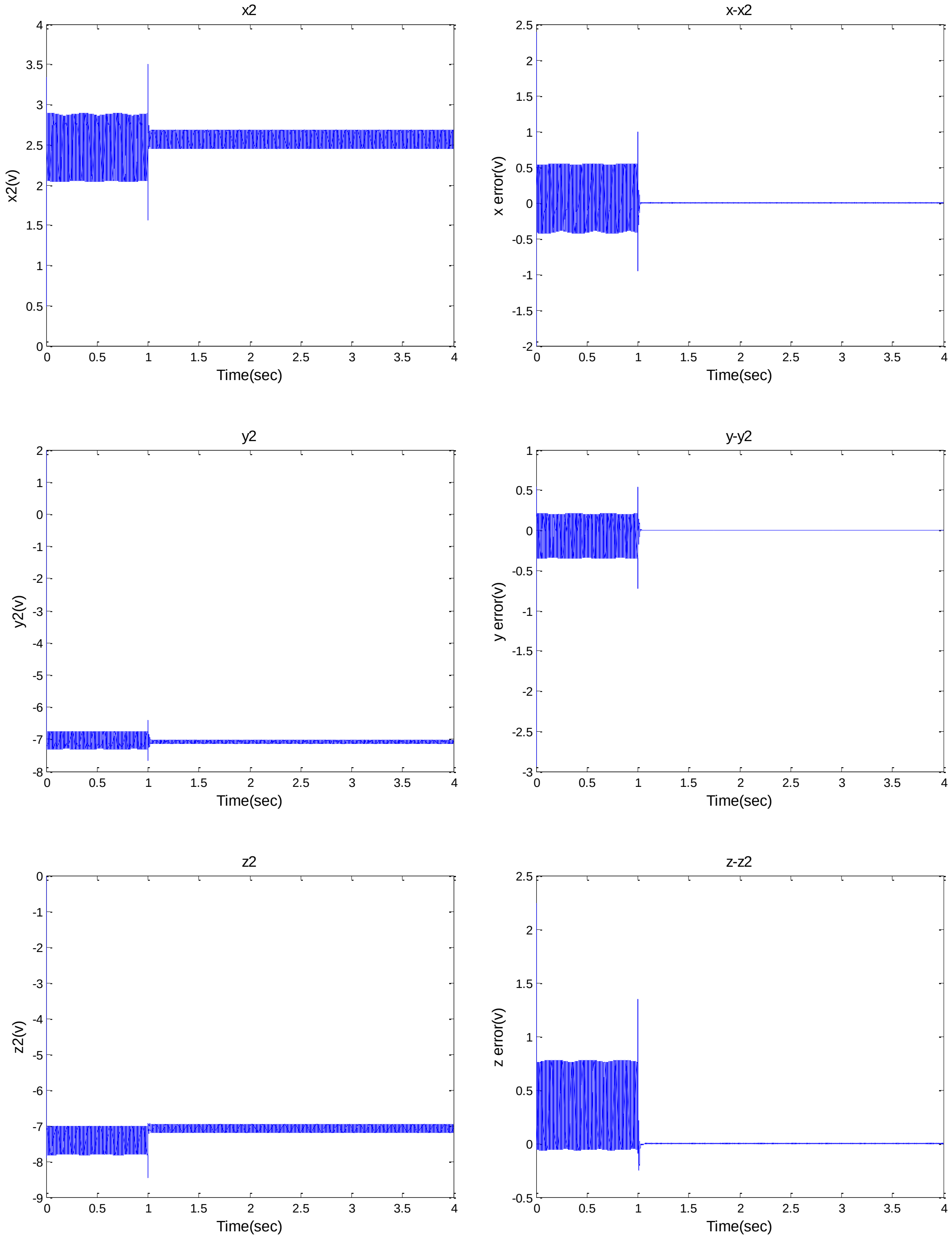

Fig. 6.5 Response when controller is applied at 1 second (left); Error between drive and response signals (right)

Daubechies D6 wavelet with 1st decomposition level is deployed to construct the transformation matrix *T*. The left column in Fig. 6.5 shows the output of the response system. When the controller is turned on at 1 second mark, the output of the response system is converged to match the output of the drive system after a short transient. The 3 plots on the right indicate that the error between the drive and the response systems is reduced to almost zero after the controller is brought online. To observe the influence on the frequency response by the controller, the instantaneous frequency (IF) of the controlled response signal in Figs. 6.6(d-f) is compared with the driving signal in Figs. 6.6(a-c). For clarity, only the first one or two frequency modes are illustrated. It is seen that the IF of the response signal is restored to follow the driving signal with great fidelity after the controller is activated at 1 second. That the two oscillators share the same IF characteristics is a strong indication that the wavelet-based controller is highly effective in synchronizing the drive-response system with conspicuous correspondence and accuracy in both the time and frequency domains.

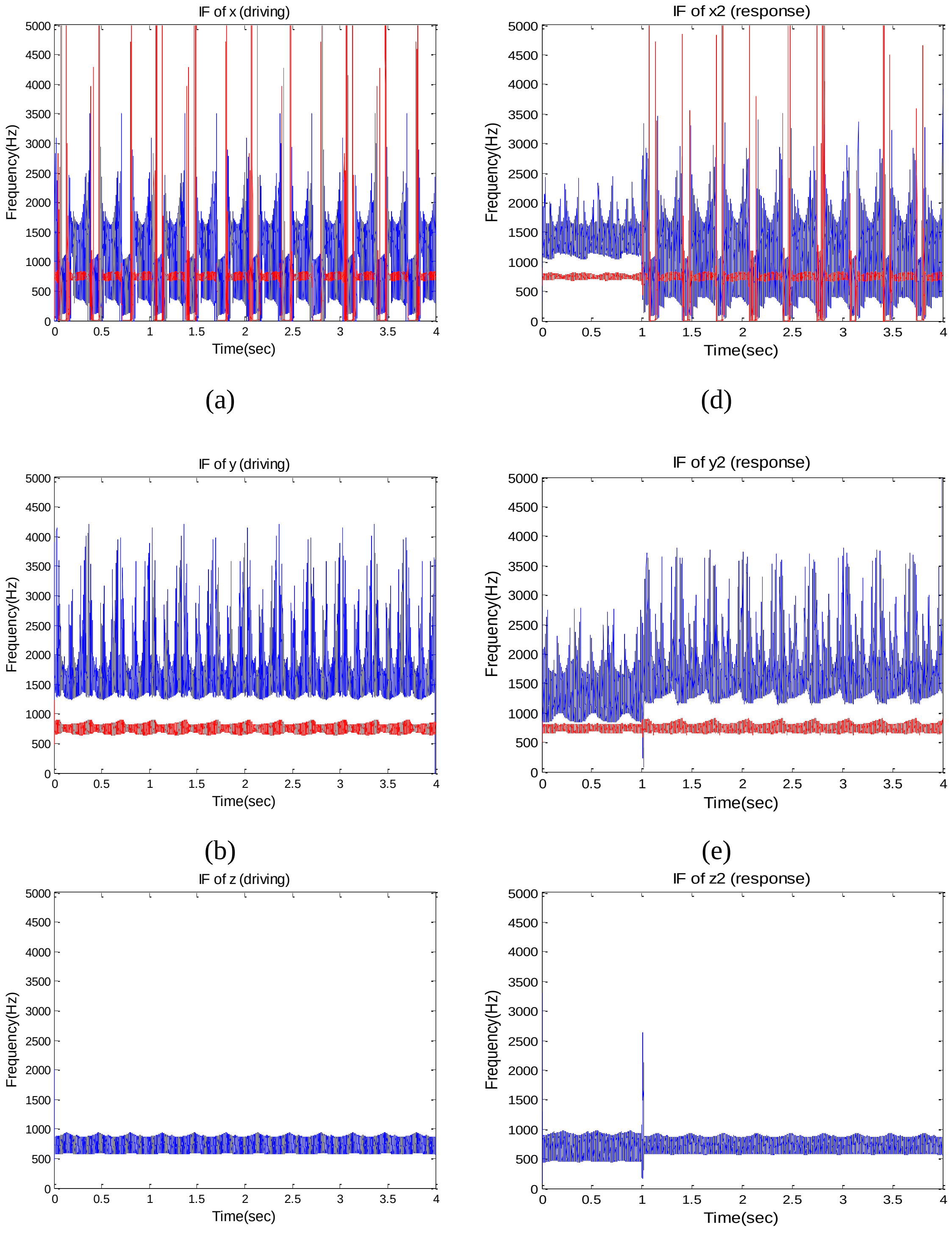

(a) (d)

(b) (e)

(c) (f)

Fig. 6.6 IF of driving signal (left); IF of response signal (right)

6.3.2 Scenario II

Synchronization of the first scenario is re-considered with a high frequency noise *d(t)* being added to variable x during the transmission from the drive to the response system in Fig. 6.3. The noise, which is a random signal of -0.5 to 0.5 volts in amplitude, is passed through a high-pass filter with a cut-off frequency at 4800Hz. The x signal of the drive system is compared with the noise-scrambled signal received by the response system (*xd*) in Fig. 6.7. Figs. 6.8(a-c) give the differences between variables in the drive system and those recovered in the response system. Even though the driving signal *x* is corrupted with the high frequency noise during transmission, the time-domain error between the driving and the response signals remains adequately constrained within a negligible range, a phenomenon understood as practical synchronization [101]. The frequency spectra in Figs. 6.8(d-f) are restored to be of the same bandwidth as the driving system's (Fig. 6.6(a-c)), though not of the exact spectral characteristics of the driving signals. The result of synchronization not being affected by the transmitted noise indicates the level of robustness of the scheme of chaos synchronization.

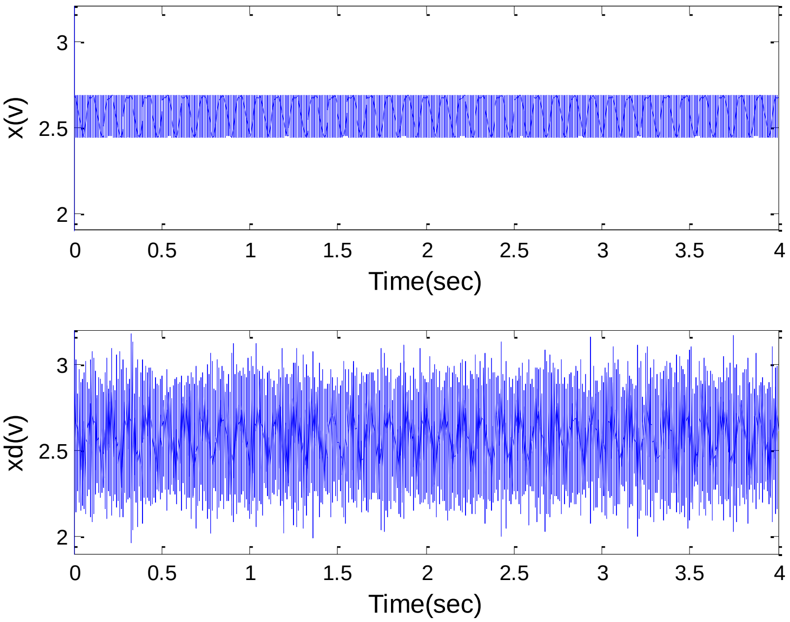

Fig. 6.7 Signal *x* in the drive system and signal *xd* received by the response system

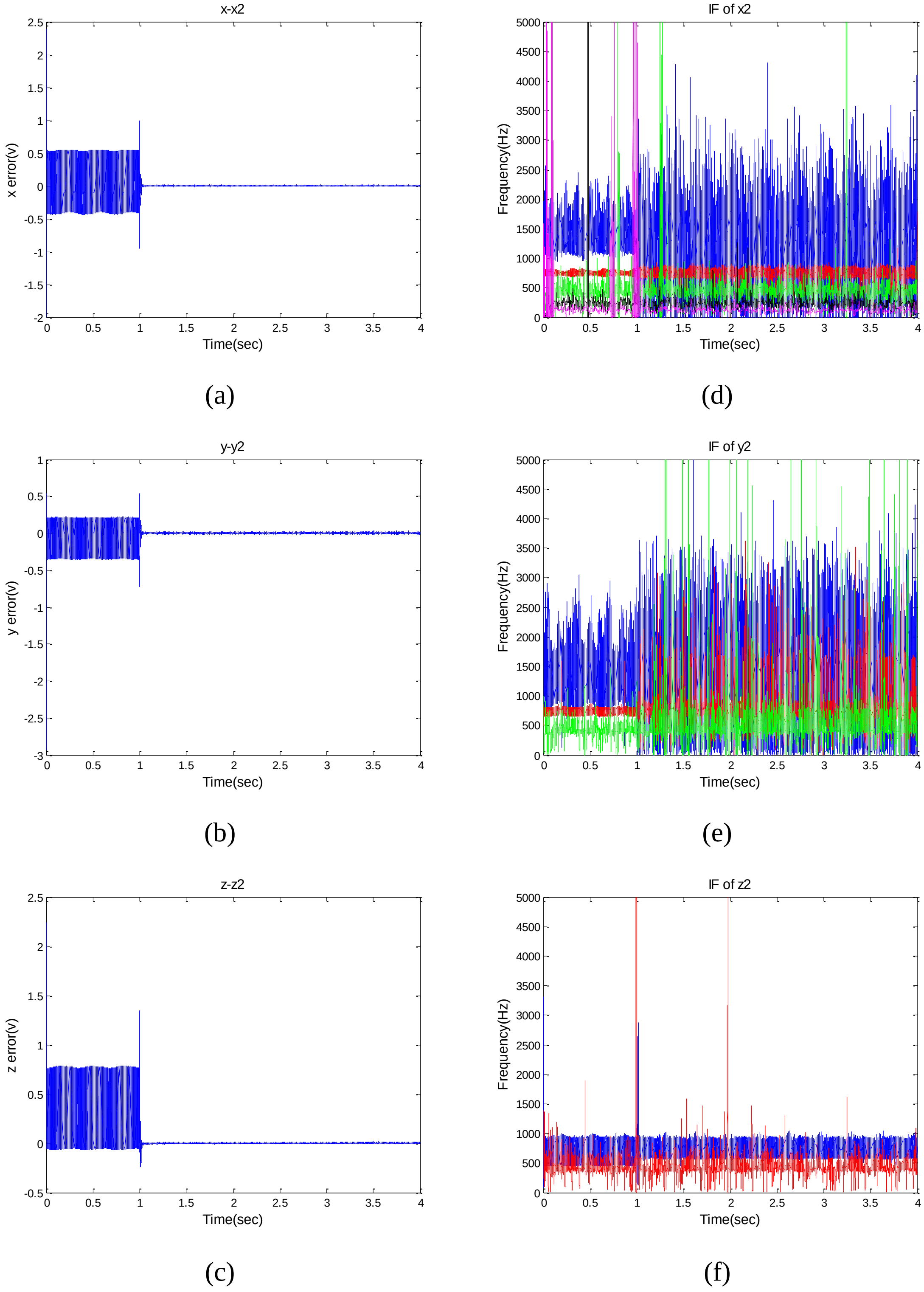

Fig. 6.8 Difference between drive and response signals (left); IF of response signal (right)

6.4 Summary

Unlike other controllers, which focus mainly on the reduction of time domain error, the objective of the wavelet-based active control scheme is to mitigate the aberrant frequencies when the system undergoes nonstationary route-to-chaos process. The parallel adaptive filters configuration allows on-line identification of unknown parameters without resorting to closed-form linearization, hence preserving the inherent characteristics of a chaotic system and minimizing the impact of external disturbance as well as internal perturbation. As oppose to contemporary control practices in which feedback loop is predominantly favored, the feedforward configuration prohibits the error from re-entering the control loop, thus reducing the risk of unintentionally exciting the sensitive chaotic system with adverse outcome. The fundamental making of the controller dictates that, through manipulating wavelet coefficients, control is simultaneously exerted and achieved in the joint time-frequency domain. It is able to mitigate and properly restrain time and frequency responses of the chaotic system at the same time, regardless of the increasing spectral bandwidth that necessarily serves to invalidate and render ineffective common time- or frequency-domain based controller design. This is also attested by the robustness demonstrated in effectively moderating the impact of high frequency noise. Time-domain wavelet transform greatly reduces the computational load of the controller. As convergence time and time-delay are expedited, the nonlinear effect of the controller itself is also minimized. The numerical study indicates that the proposed controller not only synchronizes the non-autonomous chaotic systems in the time domain. It also recovers the underlying features of the driving signal in the frequency domain without the complete knowledge of the system parameters being available. The on-line identification feature of the controller allows the response system to start at arbitrary initial conditions and to be driven by sinusoidal forcing terms of different amplitudes and phases.

7. SIMULTANEOUS TIME-FREQUENCY CONTROL OF FRICTION-INDUCED INSTABILITY

7.1 Introduction

Friction consists of two different states. In the state of “stick”, the two contacting bodies are at rest and the static friction force acts against the start of the relative motion. Once there is relative motion, the state of “slip” characterized by a force-velocity curve having negative slopes at low relative velocities would ensue. The friction is reduced when the two contacting bodies start to move but it is increased again at high relative velocity. Friction-induced oscillations switch between these two states intermittently and display stick-slip motion [123]. The stick-slip motion can be treated as the limit cycle of a self-excited vibration system where its stability is determined by the energy flowing into and dissipating from the system [124]. If the energy from the energy source flowing into the system is greater than the dissipated energy, the vibration amplitude increases. Otherwise the vibration amplitude decreases. A limit cycle is formed when the energy input and dissipated energy during each period are in balance [125]. Few studies show that friction-induced oscillations could undergo subcritical bifurcation and a slight intrusion into the unstable regime could result in large amplitude vibrations [126]. Friction-induced vibrations are the reason for brake squeal, excessive wear, fatigue, position inaccuracy, and oftentimes physical damage.

The mechanism for the generation of friction-induced vibration has been investigated experimentally [125]. It was shown that self-excited friction-induced vibrations could be caused by decreasing friction characteristic, fluctuating normal force, geometrical effect and non-conservative restoring force. When the dependence of kinetic friction coefficient on relative velocity is negative, the steady sliding at equilibrium point becomes unstable and the instability leads to the generation of vibration [127]. Stick-slip vibrations induced by alternate friction models have also been researched numerically [128]. Shooting method was applied as a periodic solution finder in combination with the alternate friction model to find periodic stick-slip solutions. Stick-slip motion and quasi-harmonic vibration were observed in phase portraits. Several methods to control friction induced vibrations are proposed in the literature. Time-delayed displacement feedback control force is applied to a mass-on-moving belt model in directions parallel and normal to the friction force, respectively [126]. It is shown to change the nature of the bifurcation from subcritical to supercritical that is globally stable in the linearly stable regime. The friction induced vibration on a disc brake is controlled by a time-delayed displacement feedback force [129]. It is able to reduce the vibration amplitude to nearly zero. A recursive time-delayed acceleration feedback control is applied to a mass-on-moving belt model in [130]. The control signal is determined recursively by an infinite weighted sum of the acceleration of the vibrating system measured at regular time intervals in the past.

High frequency oscillations with small amplitudes are applied to a mass-on-moving belt model parallel to the friction force in [123]. Adding high frequency harmonic excitation prevents self-excited oscillations from occurring. In addition to reducing self-excited oscillations to an absolute rest, the approach also transforms oscillations into small amplitude vibrations at very high frequency. The dynamics of a Coulomb friction oscillator subjected to two harmonic excitations on a moving belt is investigated in [131]. The system dynamics is affected by the value of frequency ratio and the amplitude of excitation. With high frequency ratio and large amplitude, it is able to restore chaotic motions back to periodic. A fluctuating normal force consisting of a constant force and a superimposed sinusoidal force is applied to a moving belt model in [132]. It is able to suppress stick-slip motion and reduce the vibration amplitude.

A modulated normal load in an on-off fashion depending upon the state of the system is applied to a single DOF oscillator model on a moving belt in [133]. The primary form of the control law is derived from Lyapunov's second method to ensure dissipating energy. It is able to quench the unstable limit cycle and transform it to a stable stick-slip limit cycle. Active control law is used to vary the normal contact force in a joint by a piezoelectric actuator in [134]. The Lyapunov's function-based control law is designed similar to a bang-bang controller to maximize energy dissipation instantaneously. The controller is shown to substantially reduce the vibration compared to joints with constant normal force. Active control techniques are adopted to improve the performance in eliminating the limit cycle and the steady-state error caused by unknown friction and external disturbance [135]. Adaptive fuzzy inference system is employed to model the unknown friction dynamics and a proportional-derivative (PD) compensation controller is applied. Lyapunov stability criterion is used to guarantee the convergence of the adaptive fuzzy model with PD controller.

However, all control methods reviewed previously have certain drawbacks. For time-delayed feedback control methods, the way to synthesize the control force and the amount of delayed time interval can only be determined heuristically. The same disadvantage is shared by applying high frequency oscillation and fluctuating normal force. They lack a systematic way to design the controller and predict performance. Because linear approximation is adopted to determine controller parameters for stability study, they all are unable to precisely determine the stability boundary of the friction-induced dynamics. Lyapunov stability criterion is commonly applied to design the active control law. But the Lyapunov function candidate is difficult to retrieve for a complex system. Therefore controller design based on Lyapunov stability criterion is only applicable to simple systems or models that are significantly simplified through linear approximation. Linear approximation methods are unable to realize the genuine characteristics of a route-to-chaos process [75]. Because both time and frequency responses deteriorate simultaneously in route-to-chaos, it is crucial to design a nonlinear controller in the time and frequency domains concurrently. This is especially so for the highly nonlinear, intermittent friction-induced vibration system. A simultaneous time-frequency control scheme was developed in [96] to restrain the concurrent time-frequency deterioration associated with the instability states of bifurcation and chaos. The controller is effective in denying milling chatter at high speed and restoring milling stability back to a state of limit cycle of extremely low tool vibrations [97]. In this research, finite element method along with finite difference method is used to simulate the friction-induced vibration caused by pressing a flexible cantilever beam against a rigid rotating disc. Because no approximation method is adopted, the model genuinely preserves the underlying features of the friction induced route-to-chaos. Then the time-frequency control scheme proposed in [96] is directly applied to the numerical model without resorting to closed-form solution.

7.2 Continuous Rotating Disk Model [129]

A simplified friction-induced vibration model from [129] is considered for the investigation. The model includes the discontinuity between static and kinetic frictions and the dependence of the kinetic friction on the relative velocity. It consists of a cantilever beam with an end mass that is in frictional contact with a rigid rotating disc, as shown in Fig. 7.1. The disc rotates at a constant angular velocity, ω_d. The disc is assumed to be rigid displaying no bending vibration or wobbling motion. A concentrated mass is attached to the end of the cantilever beam and a constant normal force F is used to push the mass against the rigid disk, thus generating a frictional force, F_r, in the X-Y plane, that is also a function of the relative velocity, V_r.

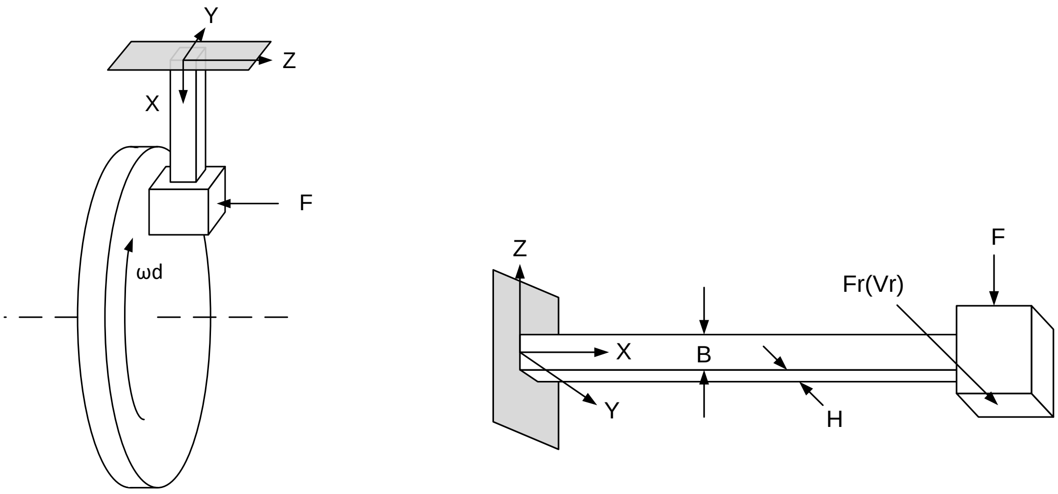

(a) (b)

Fig. 7.1 (a) Disc brake model (b) the flexible beam with end mass [129]

The continuous rotating disk model is governed by

$$\frac{\partial^4 y}{\partial x^4} + \frac{\partial^2 y}{\partial \tau^2} = 0 \tag{7.1}$$

and subject to the following boundary conditions

$$y(0,\tau) = 0, \quad \left.\frac{\partial y}{\partial x}\right|_{x=0} = 0, \quad \left.\frac{\partial^2 y}{\partial x^2}\right|_{x=1} = 0 \tag{7.2}$$

and

$$\left.\frac{\partial^2 y}{\partial \tau^2}\right|_{x=1} - r_m \left.\frac{\partial^3 y}{\partial x^3}\right|_{x=1} = N_0 \mu(v_r) \tag{7.3}$$

where the non-dimensional variables are defined as

$$x = \frac{X}{L}, \quad y = \frac{Y}{L}, \quad \tau = \Omega t$$

$$\Omega = \sqrt{\frac{EI}{\rho A L^4}}, \quad r_m = \frac{\rho A L}{M}$$

$$N_0 = \frac{N_0^*}{M\Omega^2 L}, \quad v_d = \frac{V_d}{\Omega L}, \quad v_r = v_d - \left.\frac{\partial y}{\partial \tau}\right|_{x=1}$$

in which

N_0^* is the externally applied normal load

L is the length of the beam

M is the mass of the end mass

E is the modulus of elasticity

ρ is the mass density of the beam material

$I = BH^3/12$ is the area moment of inertia of the beam cross section

$A = BH$ is the cross section area

V_d is the disc velocity, and

v_r is the normalized relative velocity between the disc and tip mass

The coefficient of friction for the stick-slip motion follows the one formulated in [123] to prevent problems of slow convergence and numerical instability caused by the discontinuity attributable to zero relative velocity.

$$\mu(v_r) = \begin{cases} \dfrac{\mu_s v_r}{v_s}, \quad for \quad |v_r| < v_s \\ sgn(v_r)\left[\mu_s - \dfrac{3}{2}(\mu_s - \mu_m)(\dfrac{|v_r| - v_s}{v_m - v_s} - \dfrac{1}{3}(\dfrac{|v_r| - v_s}{v_m - v_s})^3)\right], \quad for \quad |v_r| \geq v_s \end{cases} \tag{7.4}$$

where

v_r is the non-dimensional relative velocity between the mass and the disc

μ_s is the maximum coefficient of static friction

μ_m is the minimum coefficient of kinetic friction

v_s is the velocity corresponding to the maximum coefficient of static friction μ_s

v_m is the velocity corresponding to the minimum coefficient of kinetic friction μ_m

v_s is set to a very small number such as 10^{-4}. When the relative velocity $|v_r|$ is smaller than v_s, the model describes the state of sticking where the mass is at rest with respect to the moving belt. In contrast, when $|v_r| \geq v_s$, the state of slipping is described where the coefficient of friction is a polynomial function. The sign function, $sgn(v_r)$, can be replaced by $\arctan(kv_r)$, $k \gg 1$. The friction function plotted using $\mu_s = 0.4, v_s = 10^{-4}, \mu_m = 0.25, v_m = 0.5$, is as follows:

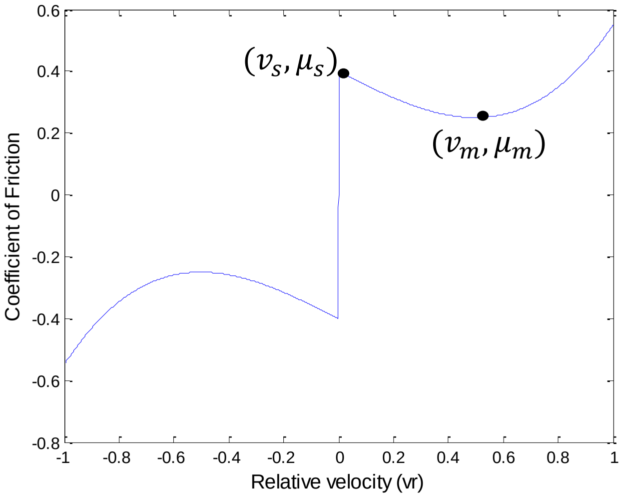

Fig. 7.2 Friction coefficient as a function of relative velocity

To solve Eq. (7.1) numerically, Galerkin's method is applied to the normalized beam equation to develop the finite element formulation and the corresponding matrix equations [136]. The average weighted residual of Eq. (7.1) is

$$\mathrm{I} = \int_0^1 \left(\frac{\partial^2 y}{\partial \tau^2} + \frac{\partial^4 y}{\partial x^4}\right) w \, dx = 0 \tag{7.5}$$

where the length of the normalized beam is 1 and w is a weight function. The beam is discretized into a number of finite elements in Fig. 7.3.

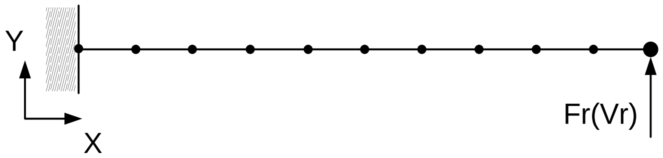

Fig. 7.3 Discretization of the disc brake model

With Ω^e defining the element domain and n the number of elements for the beam, Eq. (7.5) becomes

$$\mathrm{I} = \sum_{i=1}^{n} \left[\int_{\Omega^e} \left(w \frac{\partial^2 y}{\partial \tau^2} + \frac{\partial^2 w}{\partial x^2} \frac{\partial^2 y}{\partial x^2} \right) dx \right] + \left[w \frac{\partial^3 y}{\partial x^3} - \frac{\partial w}{\partial x} \frac{\partial^2 y}{\partial x^2} \right]_0^1 = 0 \tag{7.6}$$

Eqn. (7.6) can be rewritten as

$$\sum_{i=1}^{n} \left[\int_{\Omega^e} \left(w \frac{\partial^2 y}{\partial \tau^2} + \frac{\partial^2 w}{\partial x^2} \frac{\partial^2 y}{\partial x^2} \right) dx \right] = -\left[w \frac{\partial^3 y}{\partial x^3} - \frac{\partial w}{\partial x} \frac{\partial^2 y}{\partial x^2} \right]_0^1$$

$$= -w \frac{\partial^3 y}{\partial x^3}_{x=1} + \frac{\partial w}{\partial x} \frac{\partial^2 y}{\partial x^2}_{x=1} + w \frac{\partial^3 y}{\partial x^3}_{x=0} - \frac{\partial w}{\partial x} \frac{\partial^2 y}{\partial x^2}_{x=0} \tag{7.7}$$

Subject to the boundary conditions

$$\frac{\partial^2 y}{\partial x^2}_{x=1} = 0 \tag{7.8}$$

$$\frac{\partial^3 y}{\partial x^3}_{x=1} = \frac{1}{r_m}[\frac{\partial^2 y}{\partial \tau^2}_{x=1} - N_0\mu(v_r)] \tag{7.9}$$

$\left.\frac{\partial^3 y}{\partial x^3}\right|_{x=0}$ and $\left.\frac{\partial^2 y}{\partial x^2}\right|_{x=0}$ are the shear force and the bending moment of the normalized beam at the fixed end, respectively. The Hermitian shape functions are used to interpolate the transverse deflection *v* in terms of nodal variables v1, θ1, v2, and θ2, shown using a two-node element in Fig. 7.4.

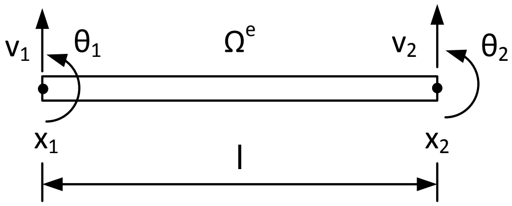

Fig. 7.4 A two-node element

The transverse deflection *v* is therefore

$$v(x) = H_1(x)v_1 + H_2(x)\theta_1 + H_3(x)v_2 + H_4(x)\theta_2 \tag{7.10}$$

where

$$d = [v_1 \quad \theta_1 \quad v_2 \quad \theta_2]^T$$

$$\omega = [H_1 \quad H_2 \quad H_3 \quad H_4]$$

$$H_1(x) = 1 - \frac{3x^2}{l^2} + \frac{2x^3}{l^3}$$

$$H_2(x) = x - \frac{2x^2}{l} + \frac{x^3}{l^2}$$

$$H_3(x) = \frac{3x^2}{l^2} - \frac{2x^3}{l^3}$$

$$H_4(x) = -\frac{x^2}{l} + \frac{x^3}{l^2}$$

The dynamic equation of the two-node element is retrieved by applying the Hermitian shape function and Galerkin's method to the left side of Eq. (7.7).

$$[M_e]\left\{\ddot{d}_e\right\} + [K_e]\left\{d_e\right\} = \left\{F_e(t)\right\} \tag{7.11}$$

Suppose $[H] = \{H_1 \quad H_2 \quad H_3 \quad H_4\}$

$$[M_e] = \int_0^l [H]^T [H] dx$$

$$= \frac{r_m l}{420}\begin{bmatrix} 156 & 22l & 54 & -13l \\ 22l & 4l^2 & 13l & -3l^2 \\ 54 & 13l & 156 & -22l \\ -13l & -3l^2 & -22l & 4l^2 \end{bmatrix} \tag{7.12}$$

And $[B] = \{H_1'' \quad H_2'' \quad H_3'' \quad H_4''\}$

$$[K_e] = \int_0^l [B]^T [B] dx$$

$$= \frac{1}{l^3}\begin{bmatrix} 12 & 6l & -12 & 6l \\ 6l & 4l^2 & -6l & 2l^2 \\ -12 & -6l & 12 & -6l \\ 6l & 2l^2 & -6l & 4l^2 \end{bmatrix} \tag{7.13}$$

The internal force between the adjacent elements is cancelled out and only the external force is left to construct $\{F_e(t)\}$. Only the boundary conditions need to be considered as the external force in this model. The global matrix equation (M, K, and F) for a dynamic beam analysis is assembled by summing up element matrices and vectors (M_e, K_e, F_e). The overall equation of motion at time t becomes

$$[M]\{\ddot{d}\}^t + [K]\{d\}^t = \{F\}^t \tag{7.14}$$

Finite difference scheme similar to [137] is used to conduct transient analysis. Assume that the initial position and velocity are available. The initial acceleration can be calculated as

$$\{\ddot{d}\}^0 = [M]^{-1}\left\{\{F\}^0 - [K]\{d\}^0\right\} \tag{7.15}$$

The velocity, displacement, and acceleration of Eq. (7.1) at each time instance are approximated by calculating Eq. (7.16)-(7.18) iteratively.

$$\{\dot{d}\}^{t+1} = \{\dot{d}\}^t + \{\ddot{d}\}^t \cdot \Delta t \tag{7.16}$$

$$\{d\}^{t+1} = \{d\}^t + \{\dot{d}\}^{t+1} \cdot \Delta t \tag{7.17}$$

$$\{\ddot{d}\}^{t+1} = [M]^{-1}\left\{\{F\}^t - [K]\{d\}^{t+1}\right\} \tag{7.18}$$

7.3 Dynamics of Friction-Induced Vibration

To investigate the dynamics of friction-induced vibration, the following non-dimensional parameters are considered: $r_m = 0.8,\ N_0 = 2,\ \mu_s = 0.4,\ \mu_m = 0.25,$ $and\ v_m = 0.5$. The disc velocity, v_d, is the control parameter. Fig. 7.2 is followed that correlates the friction coefficient with relative velocity. The dynamics of the tip mass corresponding to $v_d = 0.2$ is shown in Fig. 7.5. After the response stabilizes, the velocity profile in Fig. 7.5(a) conveys a clear stick-slip motion. The static friction dominates at certain periodic time periods when the tip mass moves at the same pace with the disc. Referring to Fig. 7.2, it is seen that the friction coefficient is negatively proportional to the relative velocity in Fig. 7.5(b). The self-excited oscillation forms a stable limit cycle as shown in Fig. 7.5(c). A static friction value at 0.8 is indicated in Fig. 7.5(d) where the dynamic friction, whose value is smaller than the static friction, occurs intermittently throughout the time window. A dominant frequency of 0.1Hz is observed in Fig. 7.5(e). However, the instantaneous frequency in Fig. 7.5(f) shows the frequency oscillates severely, an indication of nonlinear response [75].

Chaotic response is observed when v_d is increased to 0.35. High frequency modulation is found in both tip displacement and tip velocity in Fig. 7.6(a). The relative velocity in Fig. 7.6(b) demonstrates a stick-slip motion that is nonstationary and full of transient oscillations. The phase plot in Fig. 7.6(c) indicates multiple tori interweaving with each other, implying a chaotic response with broadband frequencies. The amplitude of the relative velocity in Fig. 7.6(b) falls between -0.2 and 1.0, thus corresponding the region of positive slop in Fig. 7.2 where the friction coefficient is positively proportional to the relative velocity. The highly nonlinear, intermittent friction force is generated by high relative velocity as shown in Fig. 7.6(d). The Fourier spectrum in Fig. 7.6(e) shows a dominant frequency at 0.1Hz and a cluster of frequencies around 0.5 Hz. The instantaneous frequency in Fig. 7.6(f) reflects the genuine characteristics of the frequency response, where the 0.5Hz component is a prominent temporal-spectral oscillation mode of chaotic type.

The phase portraits in Fig. 7.7 are to illustrate the evolution of friction-induced dynamics by increasing disc velocities v_d from 0.1 to 0.35. The structure of tori Fig. 7.7(a) represents a chaotic response that emerges at low speed. With the increase of disc velocity in Fig. 7.7(c), the tip dynamic is recovered to a relatively stable limit cycle at $v_d = 0.2$. Nevertheless, it starts to deteriorate when the disc velocity is increased in Figs. 7.7(d)–(f). Multiple tori occur again and the response becomes unstable and diverges when the disc velocity is greater than 0.35. The result coincides with both physical intuition and Fig. 7.2, where the friction force decreases at slow relative velocity and increases at high relative speed. Stick-slip motions are observed throughout. The instantaneous frequency in Fig. 7.8 indicates the time-frequency response with the increasing disc velocity. Comparing Figs. 7.8(a), (e), and (f) to the corresponding phase plots in Fig. 7.7, it is observed that all interweaving tori structures have an oscillating frequency at 0.5 Hz. The more irregular the phase plot is, the more severely the instantaneous frequency oscillates. As shown in Fig. 7.8(b)-(d), all stable limit cycles are of narrow bandwidth.

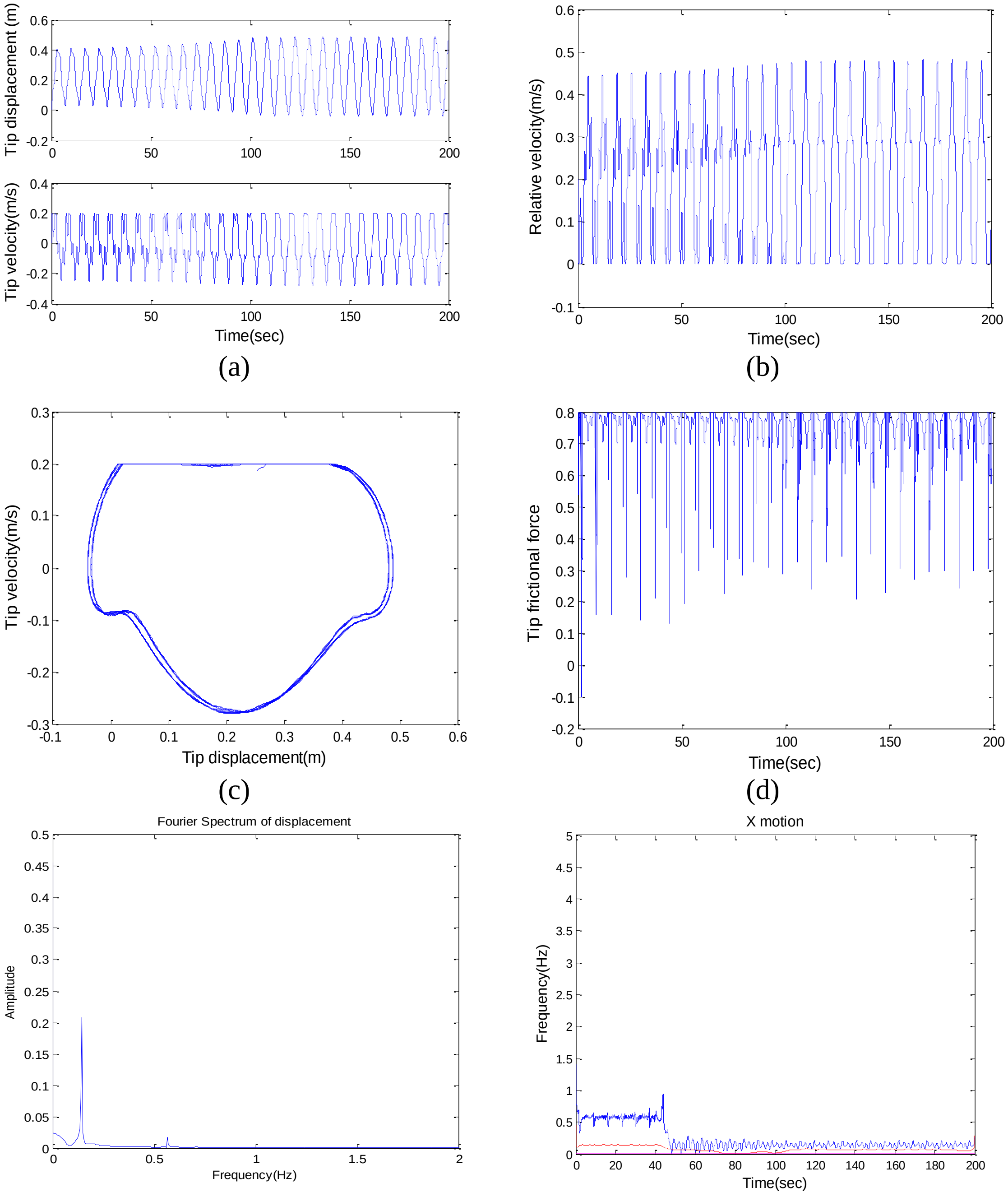

(a) (b) (c) (d) (e) (f)

Fig. 7.5 (a) Tip displacement and velocity (b) relative velocity between tip mass and disc (c) phase plot (d) friction force in *y*-direction (e) Fourier spectrum (f) Instantaneous frequency of tip displacement when $v_d = 0.2$

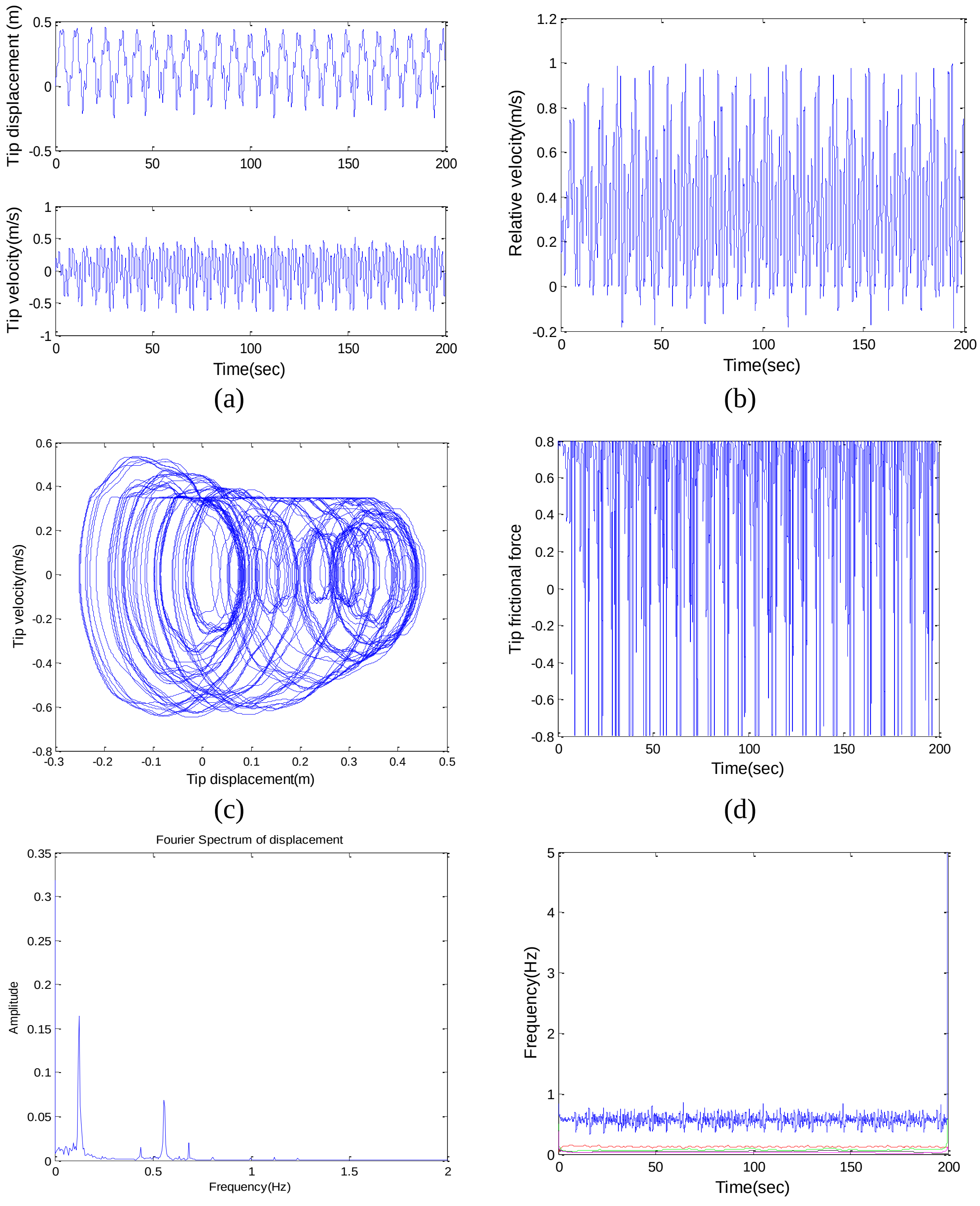

(a) (b) (c) (d) (e) (f)

Fig. 7.6 (a) Tip displacement and velocity (b) relative velocity between tip mass and disc (c) phase plot (d) friction force in *y*-direction (e) Fourier spectrum (f) Instantaneous frequency of tip displacement when $v_d = 0.35$

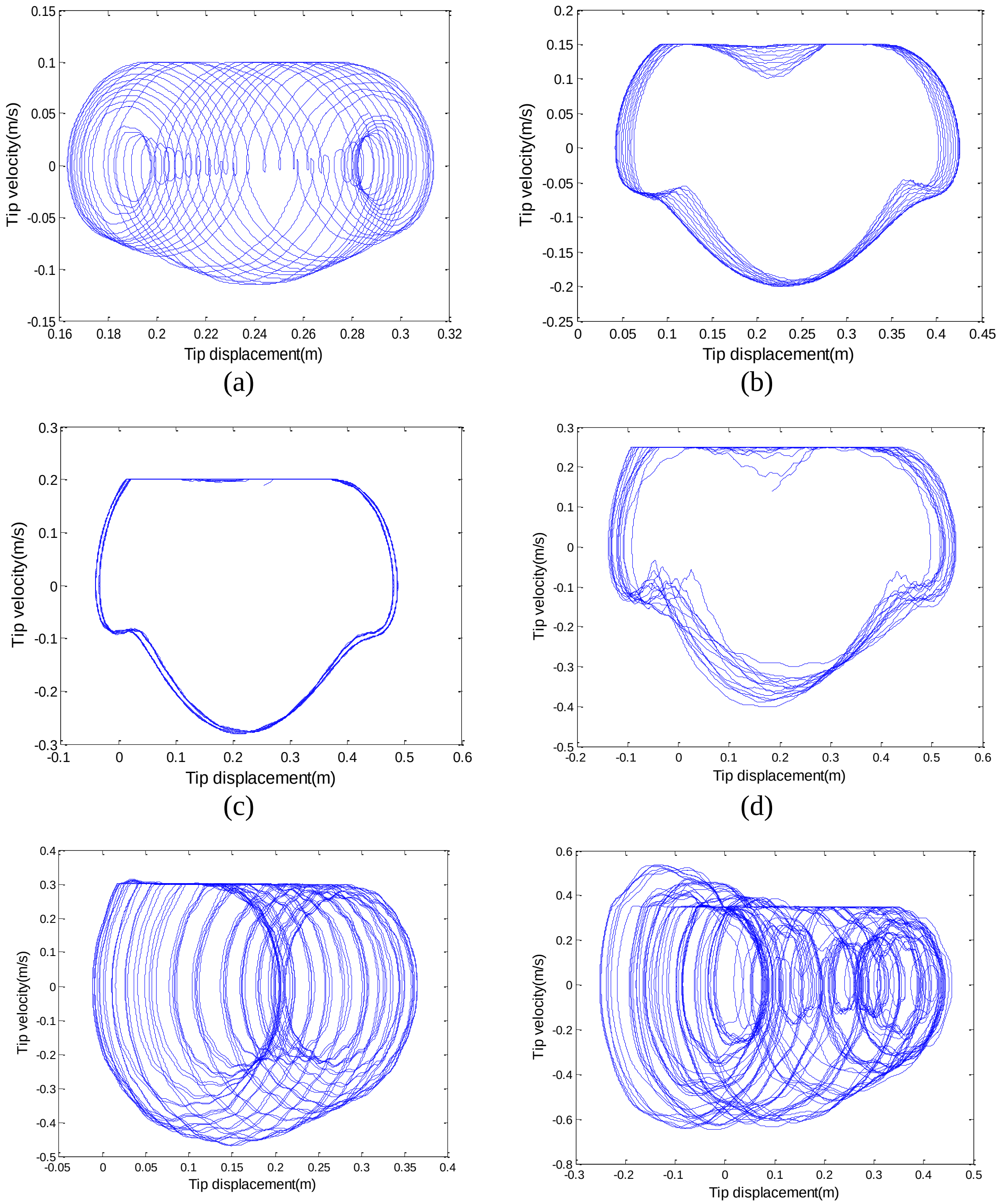

(a) (b)

(c) (d)

(e) (f)

Fig. 7.7 Phase plot of friction-induced dynamics with increasing disc velocity: (a) $v_d = 0.1$ (b) $v_d = 0.15$ (c) $v_d = 0.2$ (d) $v_d = 0.25$ (e) $v_d = 0.3$ (f) $v_d = 0.35$

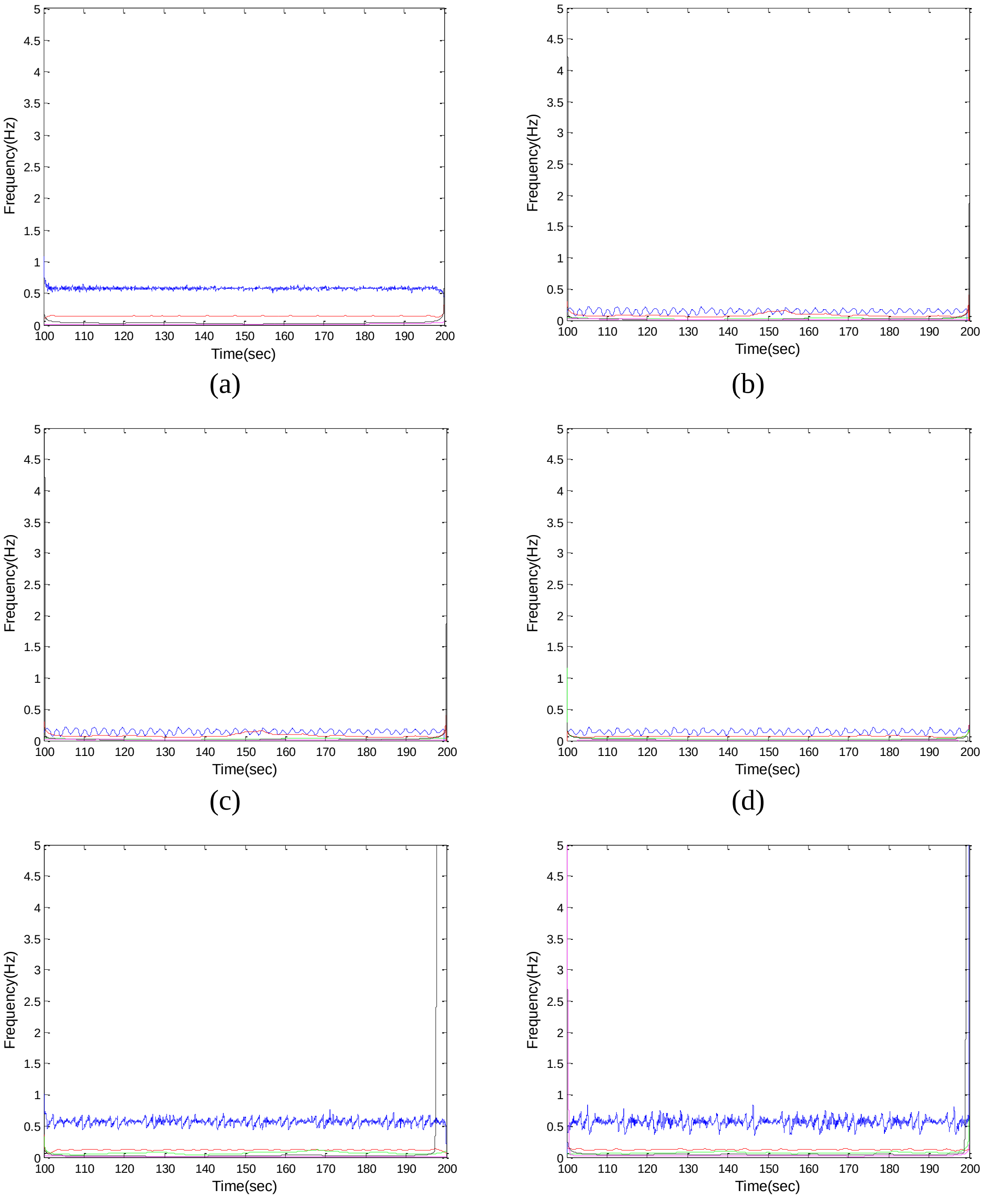

(a) (b) (c) (d) (e) (f)

Fig. 7.8 Instantaneous frequency of friction-induced dynamics with increasing disc velocity: (a) $v_d = 0.1$ (b) $v_d = 0.15$ (c) $v_d = 0.2$ (d) $v_d = 0.25$ (e) $v_d = 0.3$ (f) $v_d = 0.35$

7.4 Nonlinear Time-Frequency Control

The novel nonlinear control scheme reported in [96] was formulated to address the fundamental characteristics inherent of bifurcation and chaos. The controller doesn't adopt any linearization or method of approximation and it is applied to the nonlinear system directly, thus allowing the genuine dynamic response to be preserved and properly controlled. The normal force F applied to the tip mass in Fig. 7.1. is adjusted by Least Mean Square (LMS) adaptive filters to suppress the tip vibration amplitude. The control scheme manipulates the corresponding Discrete Wavelet Transform (DWT) coefficients of the system response to realize control in the joint time-frequency domain. The control scheme has been demonstrated to successfully negate the rich set of bifurcated and chaotic responses of a time-delayed milling model [97]. The time-frequency control scheme is applied to the disc brake model as shown in Fig. 7.9.

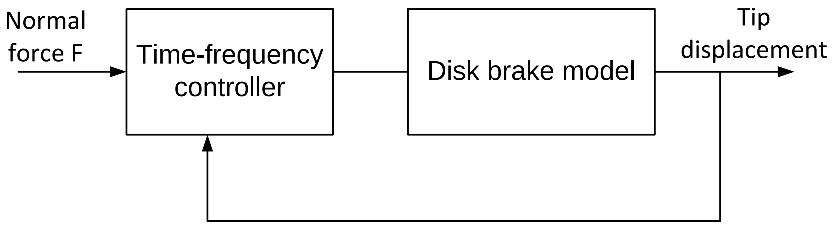

Fig. 7.9 Time-frequency control scheme of the disk brake model

The control of two chaotic conditions when v_d is 0.3 and 0.35 are considered. Chaotic vibration was observed in Fig. 7.7(e) when the disc velocity was 0.3. When the controller is turned on at 50 seconds, the severe oscillations in tip displacement and velocity are restored to a more stable vibration, as shown in Fig. 7.10(a). The applied controller affects the system dynamics and inhibits the inception of stick-slip motion. The relative velocity in Fig. 7.10(b) no longer stops at zero, the state of static friction, and remains mostly in the state of dynamic friction. The dominant frequency at 0.5Hz in Fig. 7.10(c) is eliminated after the controller is brought online. However, it still shows discontinuity in the frequency, where high frequency erupts at certain time. The friction force in Fig. 7.10(d) becomes smaller after controlled, indicating that the stick-slip phenomenon becomes opaque. The phase plots of the tip movement before and after controlled are compared in Fig. 7.11. The trajectory after controlled (Fig. 7.11(b)) shows a more stable limit cycle than Fig. 7.11(a). It has a narrower bandwidth when the controller is applied, hence restraining the system dynamics from further breakdown. Fig. 7.12 and Fig. 7.13 show the same control strategy when v_d is increased to 0.35. They all show the similar result that the controller is able to affect the system dynamics and restore chaotic responses back to a more stable state of motion.

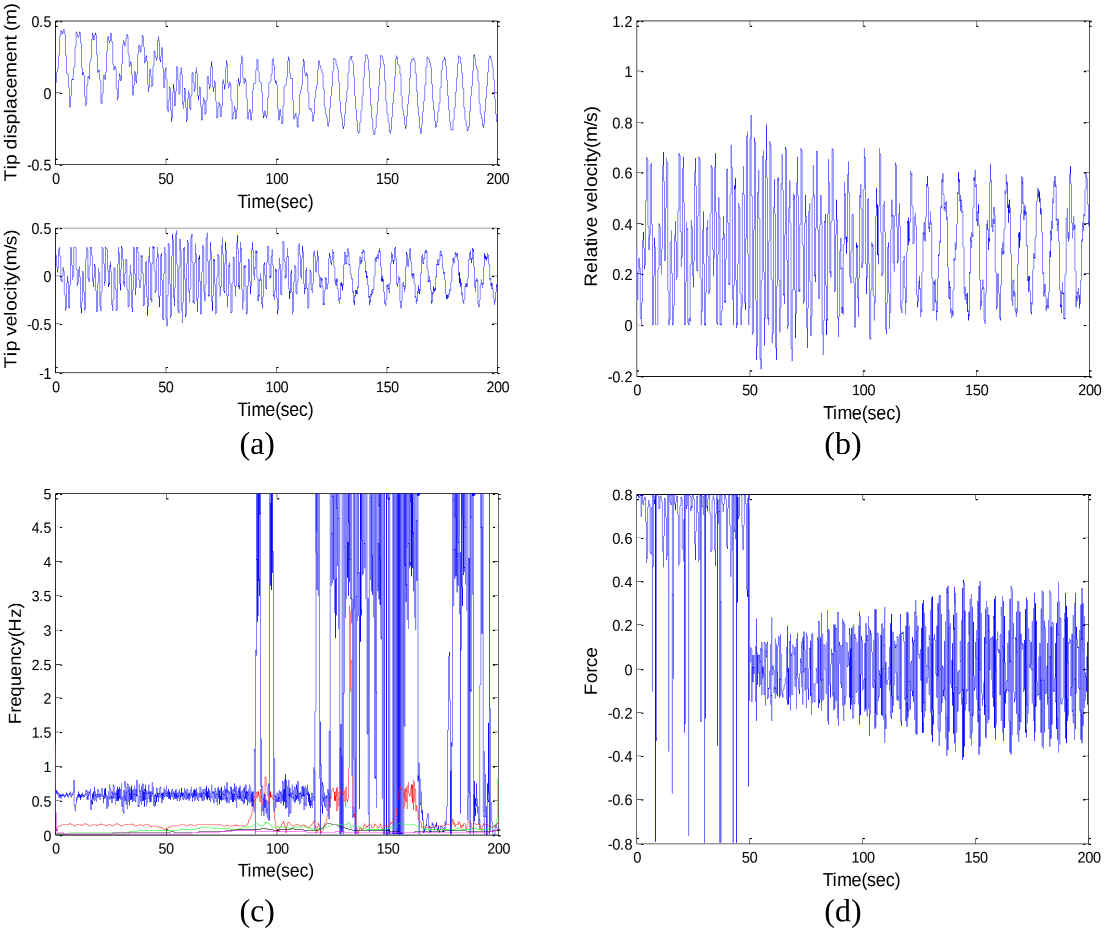

(a) (b)

(c) (d)

Fig. 7.10 (a) Tip displacement and velocity (b) relative velocity between tip mass and disc (c) instantaneous frequency (d) friction force in *y*-direction when $v_d = 0.3$ and controller is turned on at 50 seconds

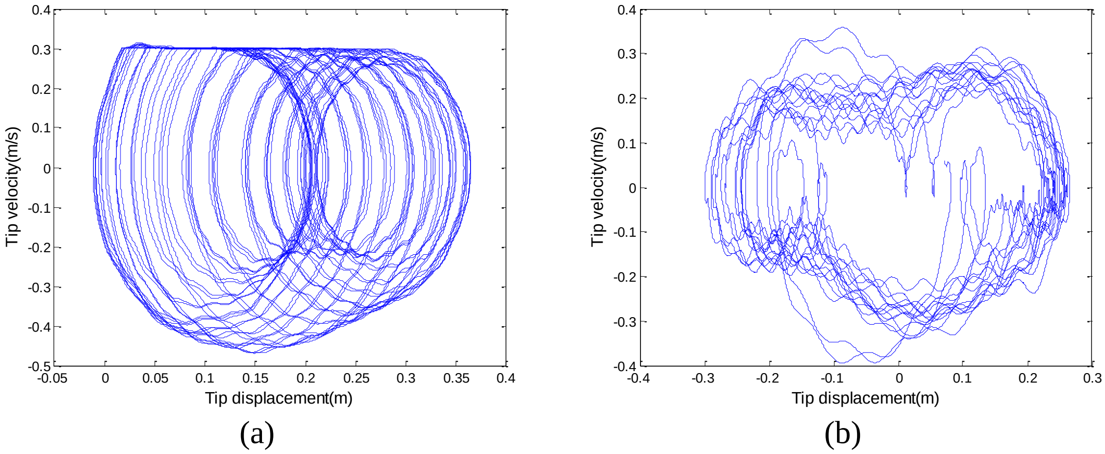

(a) (b)

Fig. 7.11 (a) Phase plot of tip movement before controlled (b) after controlled when $v_d = 0.3$

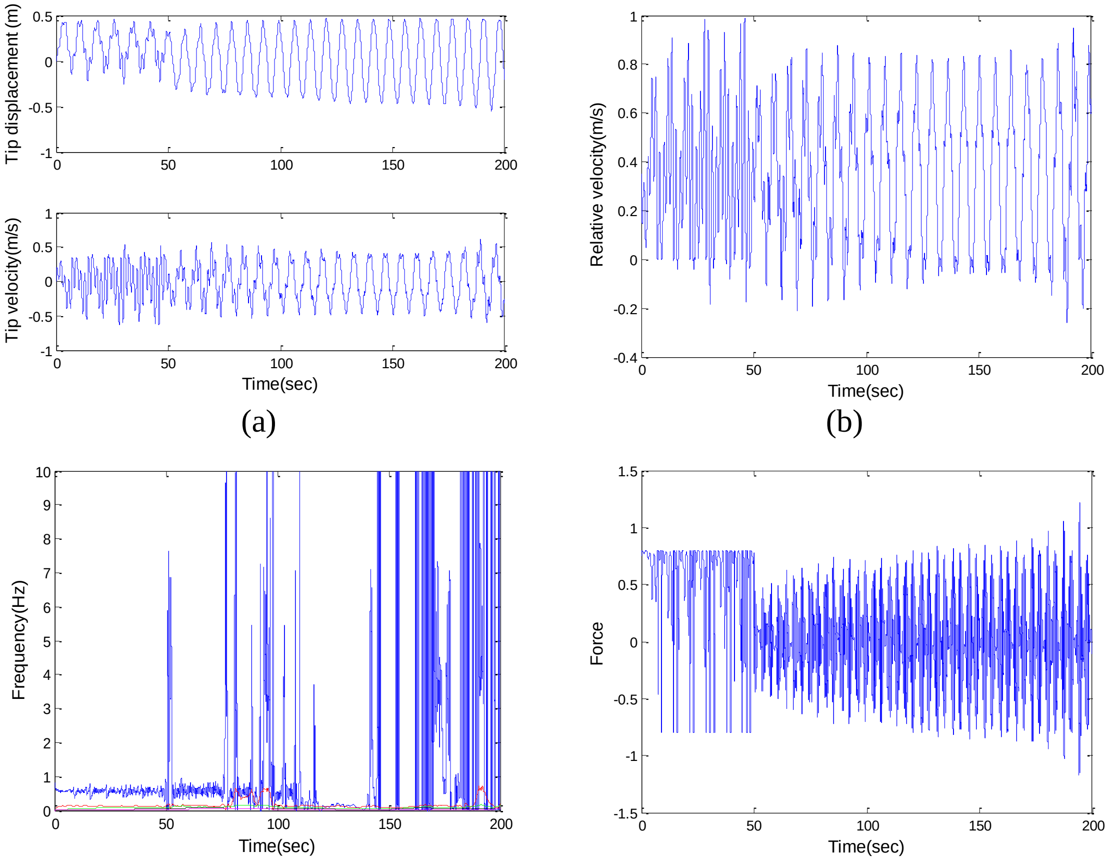

(a) (b)

(c) (d)

Fig. 7.12 (a) Tip displacement and velocity (b) relative velocity between tip mass and disc (c) instantaneous frequency (d) friction force in *y*-direction when $v_d = 0.35$ and the controller is turned on at 50 seconds

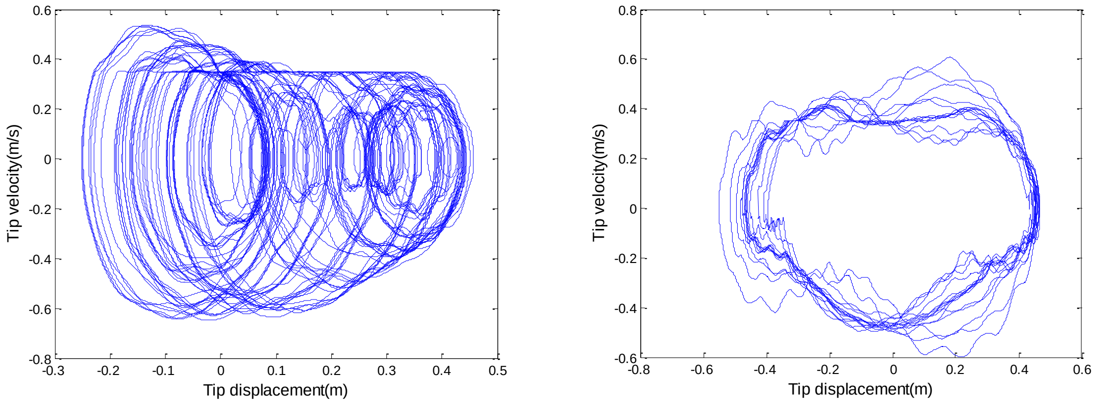

(a) (b)

Fig. 7.13 (a) Phase plot of the tip movement before controlled (b) after controlled when $v_d = 0.35$

7.5 Summary

Unlike previous studies on friction-induced dynamics which adopt either linearization method or simplified model in order to conduct analytical calculation, the numerical study using the finite element method along with the finite difference time integration scheme provided genuine insight of the friction-induced vibration. The result clearly showed stick-slip phenomenon and an unstable limit cycle in the state space. Because no approximation approach was used, responses modulated with high frequency components indicated rich nonlinearity. With the increase of the disc angular velocity, the modulated frequency became irregular and broadband in the simultaneous time-frequency domain. The system lost its stability and the oscillation diverged when the disc angular velocity exceeded certain critical value. The result coincides with the physical interpretation of friction-induced vibrations, which is highly nonlinear due to the discontinuity of the moving surfaces of contact. When the friction coefficient was negatively proportional to the relative velocity, the self-excited vibration generated a limit cycle. The system became unstable at high relative velocity when the friction coefficient was positively proportional to the relative velocity. A simultaneous time-frequency controller was deployed to control the disc break model. It was applied to the finite element model directly without resorting to linearization or closed-form solution. Therefore it was able to capture and control the genuine features of the friction-induced dynamics. The controller effectively inhibited the inauguration of chaotic response at high relative velocity and restored the system back to a relatively stable limit cycle. Because the controller was designed in the time-frequency domain, it restrained the diverging vibration amplitude and increasing bandwidth concurrently. The result indicates that the time-frequency control is a viable solution to mitigating friction-induced dynamic instabilities including route-to-chaos and discontinuity.

8. CONCLUSIONS AND RECOMMENDATIONS

8.1 Conclusions

The objective of this research was to formulate a novel nonlinear control theory that addresses and retains the fundamental characteristics inherent of all nonlinear systems undergoing route-to-chaos - one that restrains time-varying frequency spectrum from becoming broadband and also identifies the dynamic state of the system in real-time. The control scheme was demonstrated using a broad set of nonlinear systems including a nonstationary Duffin oscillator, a time-delayed milling model, a high speed micro-milling example, a synchronized chaotic circuitry, and a mass-on-a-spinning disk problem.

The research started with the investigation of a nonstationary softening Duffing oscillator, a typical example for illustrating bifurcation-to-chaos deterioration. Because nonlinear responses are oftentimes transient and consist of complex amplitude and frequency modulations, linearization would inevitably obscure the temporal transition attributable to the nonlinear terms, thus also making all inherent nonlinear effects inconspicuous. The linearization of softening Duffing oscillator underestimates the variation of the frequency response, thereby concealing the underlying evolution from bifurcation to chaos. In addition, Fourier analysis falls short of capturing the time evolution of the route-to-chaos and also misinterprets the corresponding response with fictitious frequencies. Instantaneous Frequency (IF) along with the Empirical Mode Decomposition (EMD) was adopted to unravel the multi-components that underlie the bifurcation-to-chaos transition, while retaining physical features of each component. Through considering time and frequency responses simultaneously, it was shown that the frequency of the nonlinear Duffing oscillator was a temporal-modal oscillation and that the inception of period-doubling bifurcation and the deterioration of route-to-chaos were precisely identified, implying that time-varying, transient processes fundamental of bifurcation and chaotic response need to be established in the simultaneous time-frequency domain.

Control scheme facilitated either in the time- or frequency- domain alone is insufficient in controlling route-to-chaos, where the corresponding response deteriorates in the time and frequency domain simultaneously. The nonlinear time-frequency control theory was conceived through recognizing the basic attributes inherent of all chaotic systems, including the simultaneous deterioration of dynamics in both the time and frequency domains when bifurcates, nonstationarity, and sensitivity to initial conditions. The theory has its philosophical basis established in simultaneous time-frequency control, on-line system identification and adaptive control. Physical features that embody the theory included multiresolution analysis, adaptive Finite Impulse Response (FIR) filter, and Filtered-x Least Mean Square (FXLMS) algorithm. Unlike other control theories, which focus mainly on the reduction of time domain error, the objective of the nonlinear time-frequency control theory was to mitigate the aberrant frequencies when the system underwent nonstationary route-to-chaos. The parallel adaptive filters configuration allowed on-line identification of unknown parameters without resorting to closed-form linearization, hence preserving the inherent characteristics of a chaotic system and minimizing the impact of external disturbance as well as internal perturbation. The feedforward configuration prohibited the error from re-entering the control loop, thus reducing the risk of unintentionally exciting the sensitive chaotic system with adverse outcome. Through manipulating wavelet coefficients, control was simultaneously exerted and achieved in the joint time-frequency domain. It was able to mitigate and properly restrain time and frequency responses of the chaotic system at the same time, regardless of the increasing spectral bandwidth. The control of the nonstationary softening Duffing oscillator demonstrated the effectiveness of the control methodology. Results indicated that for the control of dynamic instability including chaos to be deemed viable, mitigation had to be adaptive and engaged in the time and frequency domains at the same time.

A highly interrupted machining process, milling at high speed can be dynamically unstable and chattering with aberrational tool vibration. While its associated response is still bounded in the time domain, however, milling could become unstably broadband and chaotic in the frequency domain, inadvertently causing poor tolerance, substandard surface finish and tool damage. IF along with marginal spectrum was employed to investigate the route-to-chaos of a single-dimensional, time-delayed milling model. It was shown that marginal spectra were the tool of choice over Fourier spectra in identifying milling stability boundary. The nonlinear time-frequency control theory was explored to stabilize the nonlinear response of the milling tool in the time and frequency domains simultaneously. By exerting proper mitigation schemes to both the time and frequency responses, the controller was demonstrated to effectively deny milling chatter and restore milling stability as a limit cycle of extremely low vibrations.

The nonlinear time-frequency control theory was also demonstrated to negate the various nonlinear dynamic instabilities including tool chatter and tool resonance displayed by a multi-dimensional, time-delayed micro-milling model. Multi-variable control scheme was realized by implementing two independent controllers in parallel to follow a target signal representing the desired micro-milling state of stability. The control of unstable cutting at high spindle speeds ranging from 63,000 to 180,000 rpm and different axial depth-of-cuts were investigated using phase portrait, Poincaré section, and instantaneous frequency. The time-frequency control scheme effectively restored dynamic instabilities including repelling manifold and chaotic response back to an attracting limit cycle or periodic motion of reduced vibration amplitude and frequency response. The force magnitude of the dynamically unstable cutting process was also reduced to the range of stable cutting. The application of nonlinear time-frequency control theory to the highly nonlinear micro-milling process at high speed excitation demonstrated the capability of mitigating the process in both the time and frequency domains with significantly improved tool performance and workpiece quality.

The nonlinear time-frequency control theory was applied to synchronize two non-autonomous chaotic circuits driven by sinusoidal excitations. The driving and response circuits were subject to different initial conditions and driving forces of dissimilar amplitudes and phases, hence generating unsynchronized chaotic responses. The nonlinear controller was used to eliminate time domain as well as frequency domain difference between the driving and the response signal. The selection of controller's parameters, including mother wavelet and decomposition level, was optimized by statistics indicators, aiming to decompose the signal with the best resolution in the time-frequency domain. After the controller was activated, the instantaneous frequency of the response signal was restored to follow the driving signal with great fidelity even if the driving signal was scrambled with a high frequency noise during transmission. The result strongly indicated that the proposed nonlinear time-frequency control theory was highly effective in synchronizing the drive-response system with conspicuous correspondence and accuracy in both the time and frequency domains.

A flexible cantilever beam pressed against a rigid rotating disk was explored for studying self-excited friction-induced vibrations that are inherently unstable due to alternating friction conditions and decreasing dynamic friction characteristics. Because no linearization or approximation scheme was followed, the genuine characteristics of the discontinuous system including the route-to-chaos process were fully disclosed without any distortion. It was shown that the system dynamics was stable only within certain ranges of the relative velocity. With increasing relative velocity, the response lost its stability with diverging amplitude and broadening spectrum. The time-frequency controller was subsequently applied to negate the chaotic vibrations at high relative velocity by adjusting the applied normal force. The controller design required no closed-form solution or transfer function, hence allowing the underlying features of the discontinuous system to be fully established and controlled. The inauguration of chaotic response at high relative velocity was effectively denied to result in a restoration of the system back to a relatively stable limit cycle.

8.2 Contributions

This research has generated a nonlinear control theory that controlled nonlinear responses including chaos in both the time and frequency domains. A broad impact on the control of a wide set of nonlinear and chaotic systems is expected along with significant implications in cutting, micro machining, communication security, and the mitigation of friction-induced vibration, just to name a few. Specifically the research has achieved the followings to realize substantial contributions to the theoretical development and technical application of nonlinear control:

1. Presented a novel nonlinear time-frequency control theory

With feedforward control, on-line identification, and time-frequency control as its salient features, a chaotic system of transient, nonstationary in nature can be identified using the new nonlinear control theory without having to resort to closed-form configurations. By controlling both time and frequency domains simultaneously, nonlinear systems undergoing route-to-chaos with increasing bandwidth can be properly regulated.

2. Redefined the objective and implementation of nonlinear control

Unlike control theories of nowadays that focus on eliminating the time-domain error, the developed theory mainly focuses on restraining the frequency response from deteriorating, a phenomenon typical of all route-to-chaos.

3. Demonstrated time-frequency control of nonstationary oscillators undergoing transient route-to-chaos instability

The nonlinear control theory was demonstrated to control nonstationary oscillators whose responses are aperiodic and chaotic and achieve periodic solutions.

4. Established robust control of intermittent, interruptive milling operation

The nonlinear control theory was applied to deny the milling chatter and restore the milling stability as a limit cycle of extremely low vibrations. The feasibility of developing a chatter-free milling controller using the control theory is implied.

5. Enabled multi-variable control of high-speed micro-milling process

The various nonlinear instabilities including tool chatter and tool resonance displayed by a multi-dimensional, time-delayed micro-milling model were controlled by a multi-variable control scheme of the theory. The capability of the theory in mitigating the process in both the time and frequency domains to realize significantly improved tool performance and workpiece quality is demonstrated.

6. Provided as a viable alternative to synchronization of non-autonomous chaotic system

The nonlinear controller effectively synchronized two chaotic circuits in the time domain and at the same time restores the characteristics of the driving response in the frequency domain without complete knowledge of the system being available.

7. Controlled friction-induced, discontinuous nonlinear response

The nonlinear controller effectively inhibited the chaotic response of a rotating disk model system at high relative velocity and restored the response back to a relatively stable limit cycle.

8.3 Impact of the Research

The novel theory is not subject to all the mathematical constraint conditions and assumptions upon which common nonlinear control theories are based and derived. In addition, the multi-rate control realized by manipulating discrete wavelet coefficients enables control over nonstationary nonlinear response with increasing bandwidth - a physical condition oftentimes fails the contemporary control theories. Impact also goes to the following areas.

1. Development of a novel nonlinear control theory

The wavelet-based control theory creates a new paradigm which draws its roots from a paradigm shift in nonlinear control. It can control nonlinear responses including bifurcation and chaos without having to submit to the constraints that come with mathematical manipulation.

2. Realization of multi-rate and multi-variable nonlinear control

The multi-rate control realized by manipulating discrete wavelet coefficients enables control over nonstationary response with increasing bandwidth. The implementation of multi-variable control greatly extends the scope of application.

3. High speed and micro milling process

Current high speed and micro-milling process suffer from chatter and premature tool damage. The setting of cutting parameter depends on the stability lobe derived from linearized approximation. Hence it cannot estimate the stability boundary precisely and is subject to sudden eruption of chatter. The time-frequency control theory has been shown to effectively restrain the inauguration of chatter. The multi-variable control scheme of micro-milling instability discussed in Section 5 provides the foundation for high speed micro-milling and macro-milling controller designs. The cutting tool can be mounted on a 3-axis positioning stage driven by actuators, and tool vibrations can be measured by optical sensors. Control algorithm can be incorporated into a digital signal processor and controls the actuators. Thus the control of cutting force can be achieved by controlling the relative position between the tool and the workpiece.

4. Communication

The control theory is proved to be a promising decipher for nonautonomous chaos circuits, which is more similar to the type of synchronizing systems that are already used in communications and control. The theory has the advantage of being less sensitive to noise and requiring no prior knowledge of the circuit.

5. Active magnetic bearing system

Active magnetic bearings (AMBs) have been used as an alternative to traditional rolling or fluid film bearings for reduced friction and vibration, hence less power lost. One obstacle to the application of magnetic bearings is the high sensitivity of the control system to parametric uncertainties and bearing nonlinearities. Methods for feedback control design typically require the use of a linearized model of the system. But the highly nonlinear properties of the bearings can limit the performance of the overall system [138]. The nonlinear theory is deal for controlling magnetic bearings in that the function of on-line identification can overcome the parametric uncertainties, while the feedforward configuration can prevent the disturbance from re-entering the system. The adaptive filter along with discrete wavelet transform can be used to directly control the coil current of the electromagnet. A preliminary multi-variable control of a nonlinear AMB system is realized by using a sub-control scheme, in which two variables are wrapped up as a pseudo-input for the controller.

6. Robotics

Most bipedal robots are controlled by analytical approaches based on multi-body dynamics, pre-calculated joint trajectories, and zero-moment point considerations to ensure stability. However, these methods have several drawbacks such as strong model dependency, high power consumption, and vulnerability to external excitation. The simplest form of bipedal robotics is an inverted double-pendulum [139]. The proposed control theory can be integrated with sliding mode control concept to control the stability of an inverted double-pendulum. Preliminary results show that the controller can tolerate sudden impulse excitation due to feedforward configuration and short response time.

8.4 Recommendations for Future Work

1. Development of the stability boundary

The research is the first attempt to controlling nonlinear systems in both time and frequency domains. The control theory has been successfully applied to several models of physical systems. It is found in the course of this research that there are several factors that affect the performance and the stability of the controller including the selection of mother wavelet, decomposition level of discrete wavelet transform, length of the adaptive filter, step size of least mean square algorithm, and sampling rate. In Section 3, two time domain probability indicators, kurtosis and crest factors, were used to optimize the selection of mother wavelet and decomposition level that best represent the characteristics of the nonlinear response to be controlled. However, the stability bounds of the control theory are yet to be established mathematically. The nonlinear time-frequency controller consists of multiple sub-band filters and least mean square algorithm. Since the controller has a complete mathematical description, it could further develop to define the stability bounds similar to the performance analysis of LMS algorithm based on probability theory.

2. Formulation of the target signal

In this research, the target signal was composed from the truncated Fourier series of the dynamic response when the system was in an un-bifurcated, stable state. A mathematical, quantifiable guideline for the construction of the target signal that would guarantee unconditional and optimal control should be developed.

3. Implementation of the controller

The components of the discrete wavelet transform and adaptive filters can be implemented in a digital signal processor. It has the advantages of low power consumption, fast computational speed and short time delay. Hence it is suitable for applications requiring robust control of nonlinear, nonstationary responses in real-time.

REFERENCES

1. Boccaletti, S., Grebogi, C., Lai, Y. C., Mancini, H. and Maza, D., 2000, “The Control of Chaos: Theory and Applications,” Physics Reports, **329**, pp. 103-196.
2. Ott, E., Grebogi, C., and Yorke, J. A., 1990, “Controlling Chaos,” Physical Review Letters, **64**, pp. 1196-1199.
3. Yu, X., Chen, G., Song, Y., Cao, Z. and Xia, Y., 2000, “A Generalized OGY Method for Controlling Higher Order Chaotic System,” Proceedings of the 39th IEEE Conference on Decision and Control, Sydney, Australia, pp. 2054-2059.
4. Sanayei, A., 2009, “Controlling Chaos in Forced Duffing Oscillator Based on OGY Method and Generalized Routh-Hurwitz Criterion,” Second International Conference on Computer and Electrical Engineering, pp. 591-595.
5. Epureanu, B. and Dowell, E. H., 2000, “Optimal Multi-Dimensional OGY Controller,” Physica D: Nonlinear Phenomena, **139**(1-2), pp. 87-96.
6. Boukabou, A., Mansouri, N., 2004,”Controlling Chaos in Higher-Order Dynamical Systems,” International Journal of Bifurcation and Chaos, **14**(11), pp. 4019-4025.
7. Wang, R. and Yi, X, 2009,”The OGY Control of Chaos Signal Improved by the Reconstruction of Phase Space,” International Conference on Information Engineering and Computer Science, pp. 1-4.
8. Tian, Y., Zhu, J., Chen, G., 2005, “A Survey on Delayed Feedback Control of Chaos,” Journal of Control Theory and Applications, **4**, pp. 311-319.

9. Pyragas, K., 1992, “Continuous Control of Chaos by Self-Controlling Feedback,” Physics Letters A, **170**, pp. 421-428.
10. Nazari, M., Rafiee, G., Jafari, A. H., Golpayegani, S., 2008, “Supervisory Chaos Control of a Two-Link Rigid Robot Arm Using OGY Method,” IEEE Conference on Cybernetics and Intelligent Systems, pp. 41-46.
11. Savi, M. A., Pereira-Pinto, F. H. I. and Ferreira, A. M., 2006, “Chaos Control in Mechanical Systems,” Shock and Vibration, **13**, pp. 301-304.
12. Ogawa, A., Yasuda, M., Ozawa, Y., Kawai, T., Suzuki, R. and Tsukamoto, K., 1996, “Controlling Chaos of the Forced Pendulum with the OGY Method,” Proceedings of the 35th Conference on Decision and Control, pp. 2377-2378.
13. Okuno, H., Kanari, Y. and Takeshita, M., 2005,”Control of Three-Synchronous-Generator Infinite-Bus System by OGY Method,” Electrical Engineering in Japan, **151**(2), pp. 1047-1053.
14. Morgül, Ö., 2003, “On the Stability of Delayed Feedback Controllers,” Physics Letter A, **314**, pp. 278-285.
15. Postlethwaite, C. M., 2009, “Stabilization of Long-Period Periodic Orbits Using Time-Delayed Feedback Control,” Society for Industrial and Applied Mathematics, **8**(1), pp. 21-39.
16. Pyragas, K., 2006, “Delayed Feedback Control of Chaos,” Philosophical Transactions of the Royal Society A, **364**, pp. 2309-2334.
17. Fradkov, A. L. and Evans, R. J., 2005, “Control of Chaos: Methods and Applications in Engineering,” Annual Reviews in Control, **29**, pp. 33-56.

18. Behal, A., Dixon, W., Dawson, D. M. and Xian, Bin, 2010, *Lyapunov-Based Control of Robotic Systems*, CRC Press.

19. Park, H. J., 2005, “Chaos Synchronization of a Chaos System via Nonlinear Control,” Chaos, Solitons and Fractals, **25**, pp. 579-584.

20. Song, L. and Yang, J., 2009, “Chaos Control and Synchronization of Dynamical Model of Happiness with Fractional Order,” Industrial Electronics and Applications, pp. 919-924.

21. Daafouz, J. and Millerioux, G., 2000, “Parameter Dependent Lyapunov Function for Global Chaos Synchronization of Discrete Time Hybrid Systems,” Control of Oscillations and Chaos 2nd International Conference, **2**, pp. 339-342.

22. Yang, Z., Jiang, T. and Jing, Z, 2010, “Chaos Control in Duffing-Van Der Pol System,” International Workshop on Chaos-Fractal Theory and its Applications, pp. 106-110.

23. Nijmeijer, H. and Berghuis, H., 1995, “On Lyapunov Control of the Duffing Equation,” IEEE Transactions on Circuits and Systems I: Fundamental Theory and Applications, **42**(8), pp. 473-477.

24. Wang, R. and Jing, Z., 2004, “Chaos Control of Chaotic Pendulum System,” Chaos, Solitions and Fractals, **21**, pp. 201-207.

25. Yazdanpanah, Am., Khaki-Sedigh, A. and Yazdanpanah, Ar., 2005, “Adaptive Control of Chaos in Nonlinear Chaotic Discrete-time systems,” International Conference on Physics and Control, pp. 913-915.

26. Bessa, W. M., Paula, A. S. and Savi, M. A., 2009, “Chaos Control Using an Adaptive Fuzzy Sliding Mode Controller with Application to a Nonlinear Pendulum,” Chaos, Solitons and Fractals, **42**, pp. 784-791.

27. Huang, L., Yin, Q., Sun, G., Wang, L. and Fu, Y., 2008, “An Adaptive Observer-based Nonlinear Control for Chaos Synchronization,” 2nd International Symposium on System and Control in Aerospace and Astronautics, pp. 1-4.

28. Chen, D. Y. and Ma, X. Y., 2010, “A Hyper-Chaos with only One Nonlinear Term and Its Adaptive Synchronization and Control,” Control and Decision Conference, pp. 1689-1694.

29. Yang, B. and Suh, C.S., 2004, "On The Nonlinear Features of Time-Delayed Feedback Oscillators," Communications in Nonlinear Science and Numerical Simulations, **9**(5), pp.515-529.

30. Lynch, S., 2003, *Dynamical Systems with Applications Using MATLAB*, Ch. 6, Birkhäuser.

31. Yang, B. and Suh, C.S., 2003, "Interpretation of Crack Induced Nonlinear Response Using Instantaneous Frequency," Mechanical Systems and Signal Processing, **18**(3), pp. 491-513.

32. Mahmoud, G. M. and Bountis, T., 2004. “The Dynamics of Systems of Complex Nonlinear Oscillators: A Review,” International Journal of Bifurcation and Chaos in Applied Sciences and Engineering, **14**(11), November, pp. 3821-3846.

33. Huang, N. E. et al., 1998. “The Empirical Mode Decomposition and the Hilbert Spectrum for Nonlinear and Non-stationary Time Series Analysis,” Proceedings of

the Royal Society A: Mathematical, Physical and Engineering Sciences, **454**, pp. 903-995.

34. Yang, B. and Suh, C. S., 2006. "On Fault Induced Nonlinear Rotary Response and Instability," International Journal of Mechanical Science, **48**(10), October, pp. 1103-1125.
35. Yang, B. and Suh, C. S., 2004. "On the Characteristics of Bifurcation and Nonlinear Dynamic Response," Journal of Vibration and Acoustics, **126**(4), October, pp. 574-579.
36. Pai, P. F. and Hu, J., 2006. "Nonlinear Structural Dynamics Characterization by Decomposing Time Signals using Hilbert-Huang Transform," Structures, Structural Dynamics and Material Conference, May.
37. Kijewski-Correa, T. and Kareem, A., 2007. "Nonlinear Signal Analysis: Time-Frequency Perspectives," Journal of Engineering Mechanics, **133**(2), February, pp. 238-245.
38. Kerschen, G., Vakakis, A. F., and Lee, Y. S., 2008. "Toward A Fundamental Understanding of the Hilbert-Huang Transform in Nonlinear Structural Dynamics," Journal of Vibration and Control, **14**(1-2), pp. 77-105.
39. Douka, E. and Hadjileoniadis, L.J., 2005. "Time-Frequency Analysis of the Free Vibration Response of a Beam with a Breathing Crack," NDT&E International, **38**(1), January, pp. 3-10.

40. Pai, P. F. and Palazotto, A. N., 2008. “Detection and Identification of Nonlinearities by Amplitude and Frequency,” Mechanical Systems and Signal Processing, **22**(5), July, pp. 1107-1132.

41. Nayfeh, A. H. and Sanchez, N. E., 1989. “Bifurcations in a Forced Softening Duffing Oscillator,” International Journal of Nonlinear Mechanics, **24**(6), pp. 483-497.

42. Moslehy, F. A. and Evan-Iwanowski, R. M., 1991. “The Effects of Non-Stationary Processes on Chaotic and Regular Responses of the Duffing Equation,” International Journal of Nonlinear Mechanics, **26**(1), pp. 61-71.

43. Lu, C. H. and R. M. Evan-Iwanowski, 1994. “Period Doubling Bifurcation Problems in the Softening Duffing Oscillator with Nonstationary Excitation,” Nonlinear Dynamics, **5**(4), June, pp. 401-420.

44. Ville, J., 1958. *Theory and Applications of the Notion of Complex Signals.* Translated by I. Seline in RAND tech. rept. T-92, RAND Corp., Santa Monica, CA.

45. Gabor, D., 1946. “Theory of Communications,” Journal of the Institute of Electrical Engineers, **93**(26), November, pp. 429-457.

46. Jeevan, L. G. and Malik, V., 2010, “A Wavelet Based Multi-Resolution Controller,” Journal of Emerging Trends in Computing and Information Sciences, **2**, pp. 17-21.

47. Cloe, M. O. T., Keogh, P. S., Burrows, C. R. and Sahinkaya, M. N., 2006, “Wavelet Domain Control of Rotor Vibration,” Proceedings of the Institution of Mechanical Engineers, Part:C Journal of Mechanical Engineering Science, **220**, pp. 167-184.

48. Tsotoulidis, S., Mitronikas, E. and Safacas, A., 2010, "Design of a Wavelet Multiresolution Controller for a Fuel Cell Powered Motor Drive System," XIX International Conference on Electrical Machine, pp. 1-6.

49. Cade, I. S., Keogh, P. S. and Sahinkaya, M. N., 2007, "Rotor/active Magnetic Bearing Transient Control using Wavelet Predictive Moderation," Journal of Sound and Vibration, **302**, pp. 88-103.

50. Yousef, H. A., Elkhatib, M. E., Sebakhy, O. A., 2010, ", Wavelet Network-based Motion Control of DC Motors," Expert System with Applications, **37**, pp. 1522-1527.

51. Cruz-Tolentino, J. A., Ramos-Velasco, L. E. and Espejel-Rivera, M. A., 2010, "A Self-tuning of a wavelet PID controller," 20th International Conference on Electronics, Communications and Computer, pp. 73-78.

52. Sanner, R. M. and Slotine, J. E., 1995, "Structurally Dynamic Wavelet Networks for the Adaptive Control of Uncertain Robotic Systems," Proceedings of the 34th Conference on Decision & Control, pp. 2460-2467.

53. Hsu, C. F., Lin, C. M. and Lee, T. T., 2006, "Wavelet Adaptive Backstepping Control for a Class of Nonlinear Systems," IEEE Transactions on Neural Networks, **17**(5), pp. 1175-1183.

54. Lin, C. M., Hung, K. N. and Hsu, C. F., 2007, "Adaptive Neuro-Wavelet Control for Switching Power Supplies," IEEE Transactions on Power Electronics, **22**(1), pp. 87-95.

55. Polycarpou, M. M., Mears, M. J., Weaver, S. E., 1997, "Adaptive Wavelet Control of Nonlinear Systems," Proceedings of the 36th Conference on Decision & Control, pp. 3890-3895.

56. Mohammadi, S. J., Sabzeparvar, M., Karrari, M., 2010, "Aircraft Stability and Control Model using Wavelet Transforms," Proceedings of the Institution of Mechanical Engineers, Part G: Journal of Aerospace Engineering, **224**(10), pp. 1107-1118.

57. Kuo, S. M. and Morgan, D. R., 1996, *Active Noise Control Systems: Algorithms and DSP Implementations*, Wiley-Interscience, New York, U. S. A.

58. Yang, S. M., Sheu, G. J. and Liu, K. C., 2005, "Vibration Control of Composite Smart Structures by Feedforward Adaptive Filter in Digital Signal Processor," Journal of Intelligent Material Systems and Structures, **16**, pp. 773-779.

59. Guan, Y. H., Lim, T. C. and Shepard, W. S., 2005, "Experimental Study on Active Vibration Control of a Gearbox System," Journal of Sound and Vibration, **282**, pp. 713-733.

60. Peng, F. J., Gu, M. and Niemann, H. J., 2003, "Sinusoidal Reference Strategy for Adaptive Feedforward Vibration Control: Numerical Simulation and Experimental Study," Journal of Sound and Vibration, **256**, pp. 1047-1061.

61. Håkansson, L., Claesson, I. and Sturesson, P. O. H., 1998, "Adaptive Feedback Control of Machine-Tool Vibration based on The Filtered-x LMS Algorithm," International Journal of Low Frequency Noise, Vibration and Active Control, **17**(4), pp. 199-213.

62. Yazdanpanah, Am., Khaki-Sedigh, A. and Yazdanpanah, Ar., 2005, "Adaptive Control of Chaos in Nonlinear Chaotic Discrete-Time Systems," 2005 International Conference on Physics and Control, Saint Petersburg, Russia, pp. 913-915.

63. Kim, H., Adeli, H. and Asce, F., 2004, "Hybrid Feedback-Least Mean Square Algorithm for Structural Control," Journal of Structural Engineering, **130**(1), pp. 120-127.

64. Jensen, A., Cour-Harbo, A. L., 2001, *Ripples in Mathematics,* Springer-Verlag, Berlin Heidelberg.

65. Schniter, P., 2005, "Finite-Length Sequences and the DWT Matrix," Connexions. http://cnx.org/content/m10459/2.6/.

66. Attallah, S., 2000, "The Wavelet Transform-Domain LMS Algorithm: A More Practical Approach," IEEE Transactions on Circuit and Systems: II Analog and Digital Signal Processing, **47**(3), pp. 209-213.

67. Kou, S. M., Wang, M., and Chen, K., 1992, "Active Noise Control System with Parallel On-line Error Path Modeling Algorithm," Noise Control Engineering Journal, **39**(3), pp. 119-127.

68. Haykin, S., 2002, *Adaptive Filter Theory*, Prentice-Hall, Chap. 5.

69. Chiementin, X., Kilundu, B., Dron, J. P., Dehombreux, P., and Debray, K., 2010, "Effect of Cascade Methods on Vibration Defects Detection," Journal of Vibration and Control, **17**(4), pp. 567-577.

70. Daubechies, I., 1988, "Orthonormal Bases of Compactly Supported Wavelets," Communications on Pure and Applied Mathematics, **41**, pp. 909-996.

71. Strang, G. and Nguyen, T, 1996, *Wavelets and Filter Banks*, Wellesley-Cambridge Press.

72. Davies, M. A., Pratt, J. R., Dutterer, B. and Burns, T. J., 2002, "Stability Prediction for Low Radial Immersion Milling," Journal of Manufacturing Science and Engineering, **124**(2), pp. 217-225.

73. Szalai, R., Stépán, G. and Hogan, S. J., 2004, "Global Dynamics of Low Immersion High-speed Milling," Chaos, **14**(4), pp. 1069-1077.

74. Balachandran, B., 2001, "Nonlinear Dynamics of Milling Process," Philosophical Transactions of the Royal Society A, **359**, pp. 793-819.

75. Liu, M. K., and Suh, C.S., 2012, "Temporal and Spectral Responses of A Softening Duffing Oscillator Undergoing Route-To-Chaos," Communications in Nonlinear Science and Numerical Simulations, **17**(12), pp. 5217-5228.

76. Franklin, G. F., Powel, J. D and Emami-Naeini, A., 1994, *Feedback Control of Dynamic Systems*, Addison-Wesley, U.S.A.

77. Tansel, I., Rodriguez, M., Trujillo, E., Li. W., 1998, "Micro-End-Milling – I. Wear and Breakage," International Journal of Machine Tools & Manufacture, **38**(12), pp. 1419-1436.

78. Gandarias, S., Dimov, S., Pham, D. T., Ivanov, A., Popov, K., Lizarralde, R., Arrazola, P.J., 2006, "New Methods for Tool Failure Detection in Micromilling," Proc. IMechE Part B: J. Engineering Manufacture, **220**(2), pp. 137-144.

79. Byrne, G., Dornfeld, D., Denkena, B., 2003, "Advancing Cutting Technology," STC "C" Keynote, CIRP Annals, **52**(2), pp. 483-507.

80. Basuray, P. K., Misra, B. K., and Lal, G. K., 1977, "Transition from Ploughing to Cutting during Machining with Blunt Tools," Wear, **43**(3), pp. 341-349.

81. Afazov, S. M., Ratchev, S. M., Segal, J., Popov, A. A., 2012, "Chatter Modeling in Micro-Milling by Considering Process Nonlinearities," International Journal of Machine Tools & Manufacture, **56**, pp. 28-38.

82. Park, S., Rahnama, R., 2010, "Robust Chatter Stability in Micro-Milling Operations," CIRP Annals – Manufacturing Technology, **59**, pp. 391-394.

83. Shi, Y., Mahr, F., Wagner, U., Uhlmann, E., 2012, "Chatter Frequencies of the Micromilling Processes: Influencing Factors and Online Detection via Piezoactuators," International Journal of Machine Tools & Manufacture, **56**, pp. 10-16.

84. Jin, Y., Altintas, Y., 2012, "Prediction of Micro-Milling Forces with Finite Element Method," Journal of Materials Processing Technology," **212**, pp. 542-552.

85. Jin, Y., Altintas, Y., 2011, "Slip-Line Field Model of Micro-Cutting Process with Round Tool Edge Effect," Journal of Materials Processing Technology, **211**, pp. 339-355.

86. Fang, N., 2003, "Slip-Line Modeling of Machining with a Rounded Edge Tool – Part I: New Model and Theory," Journal of the Mechanics and Physics of Solids, **51**(4), pp. 715-742.

87. Kim, J. D., Kim, D. S., 1995, "Theoretical Analysis of Micro-Cutting Characteristics in Ultra-Precision Machining," Journal of Materials Processing Technology, **49**(3), pp. 387-398.

88. Waldorf, D. J., DeVor, R. E., Kapoor, S. G., 1998, “A Slip-Line Field for Ploughing during Orthogonal Cutting,” Journal of Manufacturing Science and Engineering, **120**, pp. 693-699.

89. Jun, M. B., Liu, X., DeVor, R. E., Kapoor, S. G., 2006, “Investigation of the Dynamics of Microend Milling – Part I: Model Development,” Journal of Manufacturing Science and Engineering, **128**(4), pp. 893-900.

90. Halfmann, E. B., Suh, C. S., 2012, “High Speed Nonlinear Micro Milling Dynamics,” MSEC2012-7287, 2012 International Manufacturing Science and Engineering Conference (MSEC 2012).

91. Chae, J., Park, S. S., Freiheit, T., 2006, “Investigation of Micro-Cutting Operations,” International Journal of Machine Tools & Manufacture, **46**, pp. 313-332.

92. Rahnama, R., Sajjadi, M., Park, S. S., 2009, “Chatter Suppression in Micro End Milling with Process Damping,” Journal of Material Processing Technology, **209**, pp. 5766-5776.

93. Fortgang, J., Singhose, W., de Juanes Márquez, J., Pérez, J., 2005, “Command Shaping for Micro-Mills and CNC Controllers,” American Control Conference, pp. 4531-4536.

94. Liu, P., Zhao, D., Zhang, L., Zhang, W., 2008, “Study of Cross-Coupling Control Approach Applied in Miniaturized NC Micro-Milling Machine Tool,” IEEE International Symposium on Knowledge Acquisition and Modeling Workshop, pp. 888-891

95. Aggogeri, F., Al-Bender, F., Brunner, B., Elsaid, M., Mazzola, M., Merlo, A., Ricciardi, D., de la O Rodriguez, M., Salvi, E., 2011, “Design of Piezo-based AVC System for Machine Tool Applications,” Mechanical Systems and Signal Processing, doi:10.1016/j.ymssp.2011.06.012.

96. Liu, M. K., Suh, C. S., 2012, “Simultaneous Time-Frequency Control of Bifurcation and Chaos,” Communications in Nonlinear Science and Numerical Simulations, **17**(6), pp. 2539-2550.

97. Liu, M. K., Suh, C. S., 2012, “On Controlling Milling Instability and Chatter at High Speed,” Journal of Applied Nonlinear Dynamics, **1**(1), pp. 59-72.

98. Jun, M. B., DeVor, R. E., Kapoor, S. G., 2006, “Investigation of the Dynamics of Microend Milling – Part II: Model Validation and Interpretation,” Journal of Manufacturing Science and Engineering, **128**(4), pp. 901-912.

99. Malekian, M., Park, S., Jun, M., 2009, “Modeling of Dynamic Micro-Milling Cutting Forces,” International Journal of Machine Tools & Manufacture, **49**(7), pp. 586-598.

100. Huang, N. E., et al., 2009, “On Instantaneous Frequency,” Advances in Adaptive Data Analysis, **1**(2), pp. 177-229.

101. Pecora, L. M., Carroll, T. L., 1990, ”Synchronization in Chaotic Systems,” Physical Review Letters, **64**(8), pp. 821-824.

102. Femat, R. and Solís-Perales, 1999, “On the Chaos Synchronization Phenomena,” Physics Letter A, **262**, pp. 50-60.

103. Chen, H. K., 2005, “Global Chaos Synchronization of New Chaotic Systems via

Nonlinear Control," Chaos, Solitons and Fractals, **23**, pp. 1245-1251.

104. Park, J. H., 2006, "Synchronization of Genesio Chaotic System via Backstepping Approach," Chaos, Solitons and Fractals, **27**, pp. 1369-1375.
105. Yu, Y. and Zhang S., 2004, "Adaptive Backstepping Synchronization of Uncertain Chaotic System," Chaos, Solitons and Fractals, **21**, pp. 643-649.
106. Feki, M, 2003, "An Adaptive Chaos Synchronization Scheme Applied to Secure Communication," Chaos, Solitons and Fractals, **18**, pp. 141-148.
107. Chen, S., and Lü, J., 2002, "Synchronization of an Uncertain Unified Chaotic System via Adaptive Control," Chaos, Solitons and Fractals, **14**, pp. 643-647.
108. Lu, J., Wu, X., Han, X. and Lű. J, 2004, "Adaptive Feedback Synchronization of a Unified Chaotic System," Physics Letter A, **329**, pp. 327-333.
109. Yau, H. T., 2004, "Design of Adaptive Sliding Mode Controller for Chaos Synchronization with Uncertainties," Chaos, Solitons and Fractals, **22**, pp. 341-347.
110. Huang, C. F., Cheng, K. H. and Yan, J. J., 2008, "Robust Chaos Synchronization of Four-Dimensional Energy Resource System Subject to Unmatched Uncertainties," Communications in Nonlinear Science and Numerical Simulation, **14**, pp. 2784-2792.
111. Park, J. H., 2006, "Chaos Synchronization between Two Different Chaotic Dynamical Systems," Chaos, Solitons and Fractals, **27**, pp. 549-554.
112. Yassen, M. T., 2005, "Chaos Synchronization between Two Different Chaotic Systems Using Active Control," Chaos, Solitons and Fractals, **23**, pp. 131-140.
113. Yassen, M.T., 2005, "Controlling Chaos and Synchronization for New Chaotic

System using Linear Feedback," Chaos, Solitons and Fractals, **26**, pp. 913-920.

114. Lü, J., Zhou, T., Zhang, S., 2002," Chaos Synchronization between Linearly Coupled Chaotic Systems," Chaos, Solitons and Fractals, **14**, pp. 529-541.

115. Voss, H., U., 2000, "Anticipating Chaotic Synchronization," Physical Review E, **61**(5), pp. 5115-5119.

116. Pyragas, K., 1998, "Synchronization of Coupled Time-delay Systems: Analytical Estimations," Physical Review E, **53**(3), pp. 3067-3071.

117. Liao, X. and Chen, Guanrong, 2003, "Chaos Synchronization of General Lur's Systems via Time-Delay Feedback Control," International Journal of Bifurcation and Chaos, **13**(1), pp. 207-231.

118. Cao, J., Li, H. X. and Ho, W. C., 2005, "Synchronization Criteria of Lur'e Systems with Time-Delay Feedback Control," Chaos, Solitions and Fractals, **23**, pp. 1285-1298.

119. Yalçin, M. E., Suykens, J. A. K. and Vandewalle, J., 2001, "Master-Slave Synchronization of Lur'e Systems with Time-delay," International Journal of Bifurcation and Chaos, **11**(6), pp. 1707-1722.

120. Carroll, T. L., Heagy, J. F., and Pecora, L. M., 1996, "Transforming Signals with Chaotic Synchronization," Physical Review E, **54**(5), pp. 4676-4680.

121. Carroll, T. L. and Pecora, L. M., 1993, "Synchronizing Nonautonomous Chaotic Circuits," IEEE Transactions on Circuits and Systems II: Analog and Digital Signal Processing, **40**(10), pp. 646-650.

122. Pecora, L. M., Carroll, T. L., Johnson, G. A., Mar, D. J. and Heagy, J. F., 1997,

"Fundamentals of Synchronization in Chaotic Systems, Concepts and Applications," Chaos, **7**(4), pp. 520-543.

123. Thomsen, J. J., 1999, "Using fast vibration to quench friction-induced oscillations," Journal of Sound and Vibration, **228**(5), pp. 1079-1102.
124. Popp, K., Rudolph, M., 2004, "Vibration control to avoid stick-slip motion," Journal of Vibration and Control, **10**, pp. 1585-1600.
125. Kröger, M., Neubauer, M., and Popp, K., 2008, "Experimental investigation on the avoidance of self-excited vibrations," Philosophical Transaction of the Royal Society A, **366**, pp. 785-810.
126. Saha, A., Wahi, P., 2011, "Delayed feedback for controlling the nature of bifurcations in friction-induced vibrations," Journal of Sound and Vibration, **330**, pp. 6070-6087.
127. Nakano, K. and Maegawa, S., 2009, "Safety-design criteria of sliding systems for preventing friction-induced vibration," Journal of Sound and Vibration, **324**, pp. 539-555.
128. Leine, R. I., Van Campen, D. H., De Kraker, A., and Van Den Steen, L., 1998, "Stick-slip vibrations induced by alternate friction models, " Nonlinear Dynamics, **16**, pp. 41-54.
129. Saha, A., Pandy, S. S., Bhattacharya, B., and Wahi, P., 2011, "Analysis and control of friction-induced oscillations in a continuous system," Journal of Vibration and Control, **18**(3), pp. 467-480.

130. Chatterjee, S. and Mahata, P., 2009, “Controlling friction-induced instability by recursive time-delayed,” Journal of Sound and Vibration, **328**, pp. 9-28.

131. Cheng, G., Zu, J. W., 2003, “Dynamics of a dry friction oscillator under two-frequency excitation”, Journal of Sound and vibration, **275**, pp. 591-603.

132. Neubauer, M., Neuber, C. and Popp, K., 2005, “Control of stick-slip vibrations,” IUTAM Symposium on Vibration Control of Nonlinear Mechanisms and Structures, Munich, pp. 223-232.

133. Chatterjee, S., 2007, ”Nonlinear control of friction-induced self-excited vibration,” International Journal of Non-Linear Mechanics, **42**, pp. 459-469.

134. Gaul, L. and Nitsche, R., 2000, “Friction control for vibration suppression,” Mechanical System and Signal Processing, **14**(2), pp. 139-150.

135. Wang, Y. F., Wang, D. H. and Chai, T. Y., 2011, “Active control of friction-induced self-excited vibration using adapting fuzzy systems,” Journal of Sound and Vibration, **330**, pp. 4201-4210.

136. Kwon, Y. W., Bang, H., 1997, *The Finite Element Method using Matlab*, CRC Press.

137. Kwon, Y. W., Salinas, D., and Neibert, M. J., 1994, “Thermally induced stresses in a trilayered system,” Journal of Thermal Stresses, **17**, pp. 489-506.

138. Hung, J. Y., Albritton, N. G. and Xia, F., 2003, “Nonlinear Control of a Magnetic Bearing System,” Mechatronics, **13**, pp. 621-637.

139. Lo, J. C. and Kuo Y. H., 1998, “Decoupled Fuzzy Sliding-Mode Control,” IEEE Transactions on Fuzzy Systems, **6**(3), pp. 426-435.